I.

BMC Biology

METHODOLOGY ARTICLE

Open Access

A versatile transposon-based technology to generate loss- and gain-of-function phenotypes in the mouse liver

Anna Georgina Kopasz[1†], Dávid Zsolt Pusztai[1,2†], Réka Karkas[1,3], Liza Hudoba[1], Khaldoon Sadiq Ahmed Abdullah[1,3], Gergely Imre[1,2], Gabriella Pankotai-Bodó[4], Ede Migh[5], Andrea Nagy[1], András Kriston[5], Péter Germán[1], Andrea Bakné Drubi[1,2], Anna Molnár[1], Ildikó Fekete[1], Virág Éva Dani[1], Imre Ocsovszki[6], László Géza Puskás[1], Péter Horváth[5,7], Farkas Sükösd[4] and Lajos Mátés[1*]

Abstract

Background Understanding the contribution of gene function in distinct organ systems to the pathogenesis of human diseases in biomedical research requires modifying gene expression through the generation of gain- and loss-of-function phenotypes in model organisms, for instance, the mouse. However, methods to modify both germline and somatic genomes have important limitations that prevent easy, strong, and stable expression of transgenes. For instance, while the liver is remarkably easy to target, nucleic acids introduced to modify the genome of hepatocytes are rapidly lost, or the transgene expression they mediate becomes inhibited due to the action of effector pathways for the elimination of exogenous DNA. Novel methods are required to overcome these challenges, and here we develop a somatic gene delivery technology enabling long-lasting high-level transgene expression in the entire hepatocyte population of mice.

Results We exploit the fumarylacetoacetate hydrolase (Fah) gene correction-induced regeneration in Fah-deficient livers, to demonstrate that such approach stabilizes luciferase expression more than 5000-fold above the level detected in WT animals, following plasmid DNA introduction complemented by transposon-mediated chromosomal gene transfer. Building on this advancement, we created a versatile technology platform for performing gene function analysis in vivo in the mouse liver. Our technology allows the tag-free expression of proteins of interest and silencing of any arbitrary gene in the mouse genome. This was achieved by applying the HADHA/B endogenous bidirectional promoter capable of driving well-balanced bidirectional expression and by optimizing in vivo intronic artificial microRNA-based gene silencing. We demonstrated the particular usefulness of the technology in cancer research by creating a p53-silenced and hRas G12V-overexpressing tumor model.

Conclusions We developed a versatile technology platform for in vivo somatic genome editing in the mouse liver, which meets multiple requirements for long-lasting high-level transgene expression. We believe that this technology will contribute to the development of a more accurate new generation of tools for gene function analysis in mice.

Keywords *Fah* KO mouse, *Sleeping Beauty*, Somatic transgenesis, In vivo gene silencing, Tumor model

†Anna Georgina Kopasz and Dávid Zsolt Pusztai are joint first authors.

*Correspondence:
Lajos Mátés
mates.lajos@brc.hu
Full list of author information is available at the end of the article

Background

Genetic manipulations to modify gene expression in a cell or an organism have been applied in numerous fields including research, medicine, industrial

biotechnology, and agriculture. In research, they are used to study gene function through the generation of loss-of-function and gain-of-function phenotypes, to characterize gene expression patterns through the introduction of reporter genes, and to visualize intracellular trafficking of macromolecules through mRNA and protein tagging. The laboratory mouse is currently the predominant mammalian species in biomedical research, most commonly used as an experimental model system for investigating the pathogenesis of human diseases and for developing new therapies. However, genetic manipulations in the mouse germline are generally laborious and time consuming and frequently result in unstable transgene expression or unreliable spatiotemporal expression pattern [1, 2]. Alternatively, if genetic modifications target the soma of mice, the workflows are faster. However, these workflows are becoming dominated by viral gene delivery, and in turn, they are hampered by viral cargo limitations, and despite natural viral infectivity, they often result in unstable gene expression due to host immune response against viral proteins [3, 4]. To replace viruses, lipid nanoparticles are used extensively as synthetic non-viral delivery vehicles. They are less prone to trigger host immune response than viral vectors due to the absence of immunogenic viral proteins and do not exhibit strict cargo limitations. However, lipid nanoparticle-based somatic gene delivery is generally not as effective as the viral one. Different organs can be targeted with varying degrees of efficiency, but in the case of the liver, the procedure is particularly effective [5]. The liver can also be efficiently targeted with naked plasmid DNA using a simple in vivo transfection procedure called hydrodynamic injection [6].

However, transgene expression rapidly declines in the liver following plasmid DNA delivery [7]. To date, a number of receptors have been reported to recognize cytosolic exogenous DNA, such as Toll-like receptor 9 (TLR9), cyclic GMP-AMP synthase (cGAS), and absent in melanoma 2 (AIM2) inflammasomes [8, 9]. These receptors trigger effector pathways that contribute to the elimination and transcriptional repression of plasmid DNA. To improve the outcome of plasmid DNA delivery, the system can be supplemented with non-viral transposon-based chromosomal gene transfer. Indeed, together with *Sleeping Beauty* (SB) transposon-mediated chromosomal transfer of the transgene, the long-term parameters of gene expression slightly improve, but a few weeks after injection, the decrease in transgene expression remains enormous [10]. This suggests that the effect of cytosolic DNA sensors can only be partially avoided, even if the technology is complemented by chromosomal gene transfer. Problems persist and transgene expression is not stably maintained, at least not to a sufficient extent.

Our aim was to change this situation by improving the current biotechnology toolkit and harnessing the SB transposon together with an efficient somatic transgenesis system, taking the efficiency, versatility, and stability of liver-specific gene delivery in mice to the next level. We planned to create a technology that would simultaneously allow the expression of native or mutant isoforms of proteins and efficient silencing of any arbitrary target gene in the mouse genome, in a stable manner and a high number of cells. We took the advantage of hydrodynamic injection for efficient in vivo transfection of hepatocytes and hyperactive SB [11] transposon-mediated chromosomal gene transfer for stable transgene delivery. For achieving high affected cell number and high stability of transgene expression, we harnessed the known selection pressure exerted in fumarylacetoacetate hydrolase (*Fah*) KO livers for Fah-expressing hepatocytes [12]. Finally, for more versatile gene expression modifications, we applied a new bidirectional promoter that had not previously been part of the biotechnology toolkit and optimized intron-derived microRNA (miR)-based gene silencing in vivo in the mouse liver.

The technology platform reported here is well suited to study gene function in hepatocytes via the generation of gain-of-function and loss-of-function phenotypes as it allows the exchange of virtually the entire hepatocyte population for transgenic cells. Here we demonstrate its particular usefulness in cancer research. A current high priority in cancer research is to functionally validate candidate genetic alterations that are relevant for cancer progression as it is no longer possible to clearly identify them using bioinformatics methods based on mutation frequency analysis alone, due to potential candidates being mutated at lower frequencies in cancer samples. Thus, there is a growing demand for in vivo experimental systems where the cancer driver role of mutations could be confirmed.

Results

Simple and highly efficient gene delivery system for directed gene expression modifications in the mouse liver

Keeping in mind the general simplicity of the procedure, we based our system on the hydrodynamic injection of plasmid DNA constructs. Hydrodynamic plasmid delivery primarily targets hepatocytes by the enhancement of their membrane permeability [6, 13]. However, following in vivo transfection, chromosomal integration is also required for long-term stable transgene expression. For very efficient SB transposon-based chromosomal transgene delivery, we used a hyperactive transposase

helper SB100 [11] and a more active transposon, the so-called T2 Inverted Terminal Repeat (ITR) structure variant [14]. In those hepatocytes where hydrodynamic transfection is successful, the hyperactive transposase helper enzyme is likely to catalyze the "cut and paste" transposition reaction presumably leading to an integration into the host chromosomes [15]. However, literature data suggest that the negative effect of exogenous DNA sensors on transgene expression cannot be efficiently avoided, even if the technology is complemented by chromosomal gene transfer [10]. We hypothesized that a high level of sustained transgene expression could be achieved by exploiting the well-known high regenerative potential of adult mouse hepatocytes. Following an extended hepatectomy, which involves removing nearly 90% of liver tissue, the mouse liver can regenerate within a short time regaining its normal size [16]. Such a high regenerative potential can be harnessed to replace virtually all $Fah^{-/-}$ hepatocytes for $Fah^{+/+}$ ones in a *Fah*-deficient liver by multi-nodular repopulation due to the selective growth advantage of wild-type (WT) cells [12]. Therefore, we supplemented our transposon construct with a *Fah* coding sequence (CDS) and used a *Fah* mutant mouse strain (C57BL/6N-$Fah^{tm1(NCOM)Mfgc/Biat}$) for the hydrodynamic injections (Fig. 1a).

For directed gene expression modifications, we constructed an SB transposon-based cloning platform (Fig. 1a) built on the co-expression of two linked transcripts allowing transgene expression to be bound to the expression of the *Fah* selection marker. Transcript A codes for the selection and visualization marker proteins connected by a "self-cleaving" T2A peptide for bicistronic expression [17], whereas transcript B encodes the protein to be tested without the need for tagging. To this end, we complemented the current biotechnology toolbox with the human *HADHA/B* promoter capable of driving well-balanced bidirectional expression. The compact (390 bp) *HADHA/B* bidirectional promoter drives the expression of the human hydroxyacyl-CoA dehydrogenase trifunctional multienzyme complex alpha (HADHA) and beta (HADHB) subunits [18].

To test the functionality of the design, an EGFP-encoding transcript B driven by the *HADHB* side of the bidirectional promoter was created (Fig. 1a). First, this EGFP-expressing transposon and the SB100 transposase helper plasmid were co-delivered hydrodynamically into the liver of $Fah^{-/-}$ mice, then the curative drug nitisinone (NTBC) [12] that had been given continuously up to that point was withdrawn. Immunohistochemical (IHC) investigations (Fig. 1b) demonstrated that due to intensive multi-nodular repopulation after 3 months, virtually all hepatocytes were Fah- and EGFP-positive in the treated livers. Next, using a quantitative reverse transcription PCR (RT-qPCR) method, we identified the amount of transcripts A and B produced by the *HADHA* and *HADHB* sides of the promoter, respectively. The amounts of mCherry-T2A-Fah and EGFP mRNAs were normalized to that of the ribosomal protein L27 (*Rpl27*). Our RT-qPCR data demonstrate that the transgene had an order of magnitude stronger expression than the ribosomal protein Rpl27 in the liver (Fig. 1c), which is fully consistent with a strong but physiological gene expression level. It should be noted that the expression levels of transcripts A and B were virtually identical (1/1.18).

To better explore the impact of multi-nodular repopulation on long-term transgene expression in *Fah*-deficient livers, the same construct, in which transcript B was coding for the firefly luciferase (Luc) marker protein (Fig. 1a), was injected into both wild-type (WT) and *Fah* KO mice in the presence of the SB100 transposase helper. Transgene expression was monitored over time by detecting the bioluminescence in living animals using the IVIS Lumina III imaging system (PerkinElmer). After a slightly higher Luc expression detected in WT animals during the first week after hydrodynamic injection, this transgene expression trend was reversed from day 28 onwards. In 3 months, by day 84, the average bioluminescence intensity in WT animals decreased to 387-fold of the initial level, while in *Fah* KO animals it reached 61-fold of the initial level (Fig. 1d, e).

Design and in vivo application of amiR elements

Our SB transposon-based cloning platform also provides an opportunity for simultaneous silencing of endogenous genes by the expression of artificial microRNA (amiR) elements. In order to avoid interference with the translation of marker proteins, amiR structures were expressed from an intron inserted into transcript A. To accommodate intronic amiR structures, the modified 943-bp-long first intron of the human eukaryotic translation elongation factor 1 alpha 1 (*EEF1A1*) gene was incorporated in the mCherry CDS (Fig. 1a). To verify the in vivo applicability of intronic amiR elements in our platform, we first incorporated an amiR element silencing EGFP (amiR-EGFP) into the intron of the mCherry CDS. In this arrangement, amiR-EGFP, which is processed from transcript A, silences EGFP encoded by transcript B. The guide sequence of amiR-EGFP targeting the EGFP CDS was designed by Beisel et al. [19]. For the creation of the amiR-EGFP, "miR-E," an optimized human miR-30a-based miR backbone, was applied [20], and the EGFP guide sequence was inserted into the miR-E backbone structure (Additional file 1: Fig. S1). This amiR-EGFP- and EGFP-expressing transposon and the SB100 transposase helper plasmid were co-delivered into the liver of $Fah^{-/-}$ mice, then NTBC was withdrawn. After

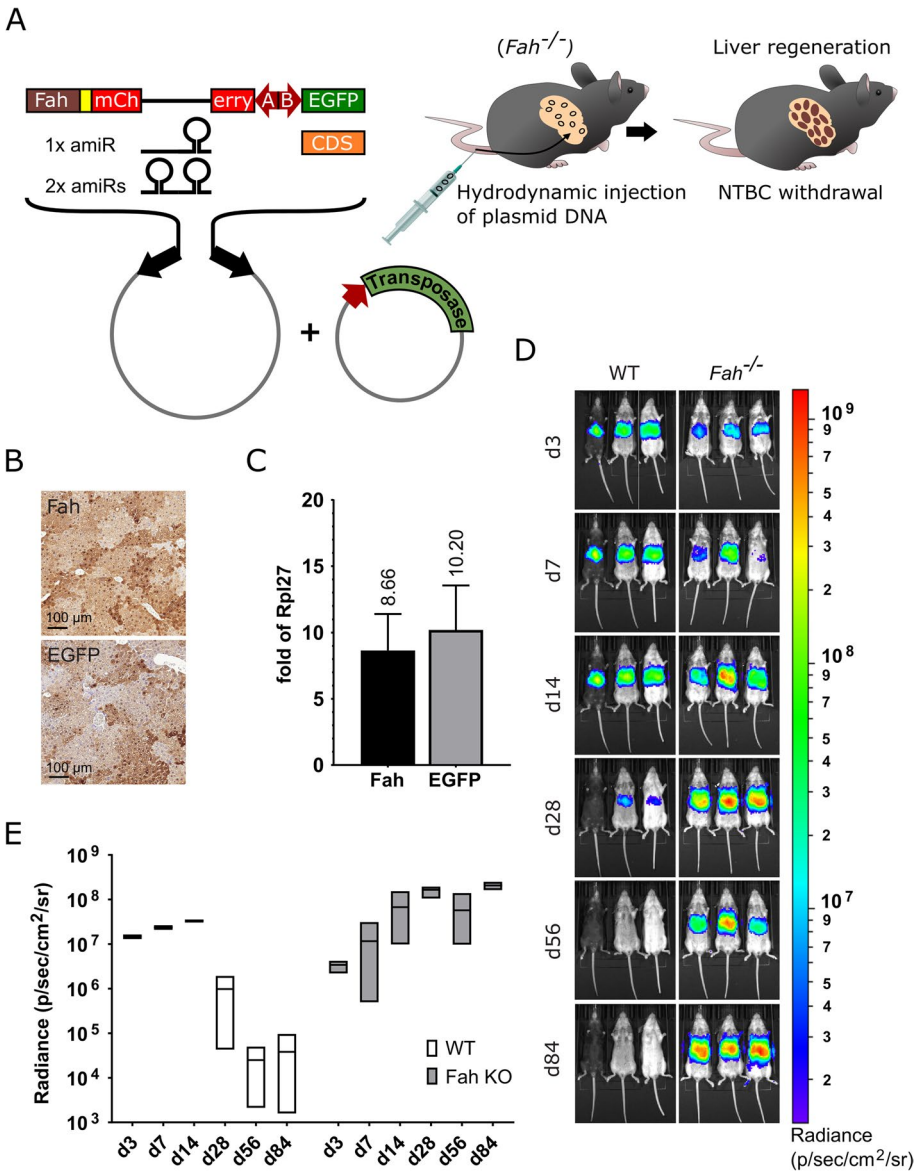

Fig. 1 In vivo transposon-based gene delivery into the liver of *Fah*$^{-/-}$ and WT mice. **a** Schematic representation of the *Sleeping Beauty* (SB) transposon-based cloning platform and animal treatments. Black arrows, SB transposon inverted terminal repeats; red arrows, promoters. **b** Fah and EGFP immunostainings of liver sections from *Fah*$^{-/-}$ mice 3 months after NTBC withdrawal. **c** Monitoring the amount of transcripts A and B following in vivo gene delivery. Liver RNA samples were collected from *Fah*$^{-/-}$ mice at 3 months post-treatment. Samples were tested using Fah- and EGFP-specific RT-qPCR assays. Results were normalized to measurements of the ribosomal protein L27 (*Rpl27*) transcript as input control and data were presented as the mean ± standard deviation (SD) ($n = 3$) (see Additional file 2 for individual data values and statistics). **d** Live bioluminescence imaging of *Fah*$^{-/-}$ and WT mice following in vivo gene delivery. Bioluminescence signals were obtained using an IVIS Lumina III imaging system at 3, 7, 14, 28, 56, and 84 days post-treatment. **e** Kinetics of bioluminescence changes during the first 3 months after gene delivery. For each experimental animal, the average radiance (photons/second/cm^2/steradian (sr) [p/s/cm^2/sr]) of circular regions of the same size covering the liver area was used for plotting. The numerical values were presented as box diagram from lowest to highest values with line at mean ($n = 3$) (see Additional file 2 for individual data values and statistics)

5 months, following complete multi-nodular repopulation, the animals were sacrificed. Macrovisualization of mCherry and EGFP autofluorescence in the liver showed that silencing of EGFP expression was very effective compared to control animals without amiR structures (Fig. 2a). The results of our EGFP Western blot assays also confirmed effective knockdown at the protein level (Additional file 1: Fig. S2). Next, RT-qPCR measurements

were used to determine the amount of A and B transcripts. According to these measurements, transcript B encoding EGFP was silenced to 4% residual gene expression in livers expressing amiR-EGFP elements (Fig. 2b).

After successful in vivo silencing of EGFP, we selected an endogenous target gene, *Tp53*, for amiR-mediated silencing. For amiR-mP53 structures — similarly to amiR-EGFP — guide sequences targeting endogenous p53 mRNA were inserted into the "miR-E" backbone (Additional file 1: Fig. S1). The amiR-mP53 guide sequences were designed following the guide design rules of Dow et al. [21] summarized in Additional file 1: Fig. S1.

To test the efficacy of amiR-mP53 elements designed to silence mouse *Tp53*, we performed studies in a mammalian tissue culture system. To this end, we inserted the first intron of the EEF1A1 gene, modified to accommodate amiR elements, into the sequence encoding the Neomycin selection marker protein and then incorporated the three amiR-mP53 elements one by one into this intron. The resulting Neomycin expression units were then inserted between the SB transposon ITRs (Additional file 1: Fig. S3). Next, the transposon series carrying the different amiR-mP53 elements and an amiR-free control transposon were co-transfected with the SB100 transposase helper plasmid into NIH3T3 cells. After G418 selection, RT-qPCR measurements were performed to determine the level of endogenous p53 mRNA in the transfected cells. Our measurements showed that all three amiR-mP53 elements were sufficiently effective. However, amiR-mP53/1 and amiR-mP53/2 elements performed better, producing 20.34 and 7.17% remaining gene expression, respectively, and were used for further in vivo studies (Fig. 2c). Subsequently, amiR-mP53/1 alone or amiR-mP53/1 and amiR-mP53/2 elements together were incorporated into the intron of the mCherry CDS in our cloning platform designed for in vivo studies (Fig. 1a). These amiR-mP53-expressing transposons and the SB100 transposase helper plasmid were co-delivered hydrodynamically into the liver of $Fah^{-/-}$ mice, then NTBC was withdrawn. After 5 months, following complete multi-nodular repopulation, the animals were sacrificed. Macrovisualization of the mCherry and EGFP autofluorescence showed that in these organs the expression of the mCherry and EGFP marker proteins was balanced and comparable to the control (Fig. 2a). Our RT-qPCR measurements confirmed that transcript A and B levels were not significantly altered compared to the control (Fig. 2b). However, we found 53% remaining *Tp53* expression in organs expressing amiR-mP53/1, while organs co-expressing amiR-mP53/1 and amiR-mP53/2 showed 32% remaining *Tp53* expression (Fig. 2b). This is in line with expectations, as hepatocytes make up about half of liver tissue [22], the other cell types are not affected by *Tp53* silencing. In contrast, EGFP is expressed exclusively in hepatocytes and therefore all EGFP-expressing cells are affected by gene silencing.

With successful gene silencing, the liver regeneration of animals expressing amiR was similar to that of controls without amiR, and no signs of non-specific toxicity associated with amiR expression were observed. The slight decrease in transgene copy number observed in livers expressing one or two amiR-mP53 elements (Fig. 2d) may explain the slight, non-significant decrease in transcript A and B levels in these organs as compared to controls (Fig. 2b).

Hepatocellular carcinoma modeling using predefined combinations of drivers

To demonstrate the utility of our technology in cancer research and the ability to co-express mutant or native proteins with amiR elements, in our cloning platform, we created an SB transposon armed to silence the endogenous *Tp53* and overexpress an oncogenic hRas variant. To achieve this, amiR-mP53/1 was introduced into the intron of the mCherry CDS in transcript A and $hRas^{G12V}$ — a constitutively active form of hRas [23] — was built into transcript B (Fig. 1a). Next, the amiR-mP53/1- and $hRas^{G12V}$-expressing driver and the

(See figure on next page.)

Fig. 2 In vivo amiR-based gene silencing in the mouse liver. **a** Brightfield and fluorescence stereomicroscopic images of the liver of $Fah^{-/-}$ mice 5 months after the intrahepatic delivery of an amiR-free control and different amiR-expressing transposon vectors. **b** Monitoring the amount of the endogenous p53 mRNA and artificial transcripts A and B in the liver of $Fah^{-/-}$ mice 5 months after intrahepatic delivery of an amiR-free control and different amiR-expressing transposon vectors. Liver RNA samples were collected from $Fah^{-/-}$ mice at 5 months post-treatment. Samples were tested using Fah-, EGFP-, and p53 mRNA-specific RT-qPCR assays. Results were normalized to measurements of the ribosomal protein L27 (*Rpl27*) transcript as input control and data were presented as the mean ± SD ($n = 3$) (see Additional file 2 for individual data values and statistics). **c** Monitoring of endogenous p53 mRNA levels in NIH3T3 cells after stable transposon-based delivery of different amiR elements designed to silence *Tp53* expression. RNA samples were collected from cultured cells after G418 selection and tested using a p53 mRNA-specific RT-qPCR assay. Results were normalized to measurements of the ribosomal protein L27 (*Rpl27*) transcript as input control. Data were presented as the mean ± SD as relative values compared to the value generated using an amiR-free control vector ($n = 3$) (see Additional file 2 for individual data values and statistics). **d** Copy numbers of the transgenes in the liver of $Fah^{-/-}$ mice following intrahepatic delivery of different transposon vectors. Liver DNA samples were collected from $Fah^{-/-}$ mice at 5 months post-treatment. Samples were tested using a *Fah* transgene-specific qPCR assay. Results were normalized to measurements of the olfactory receptor 16 (*Olfr16*) gene as an input control, and values were presented relative to one diploid genome ($n = 3$) (see Additional file 2 for individual data values and statistics)

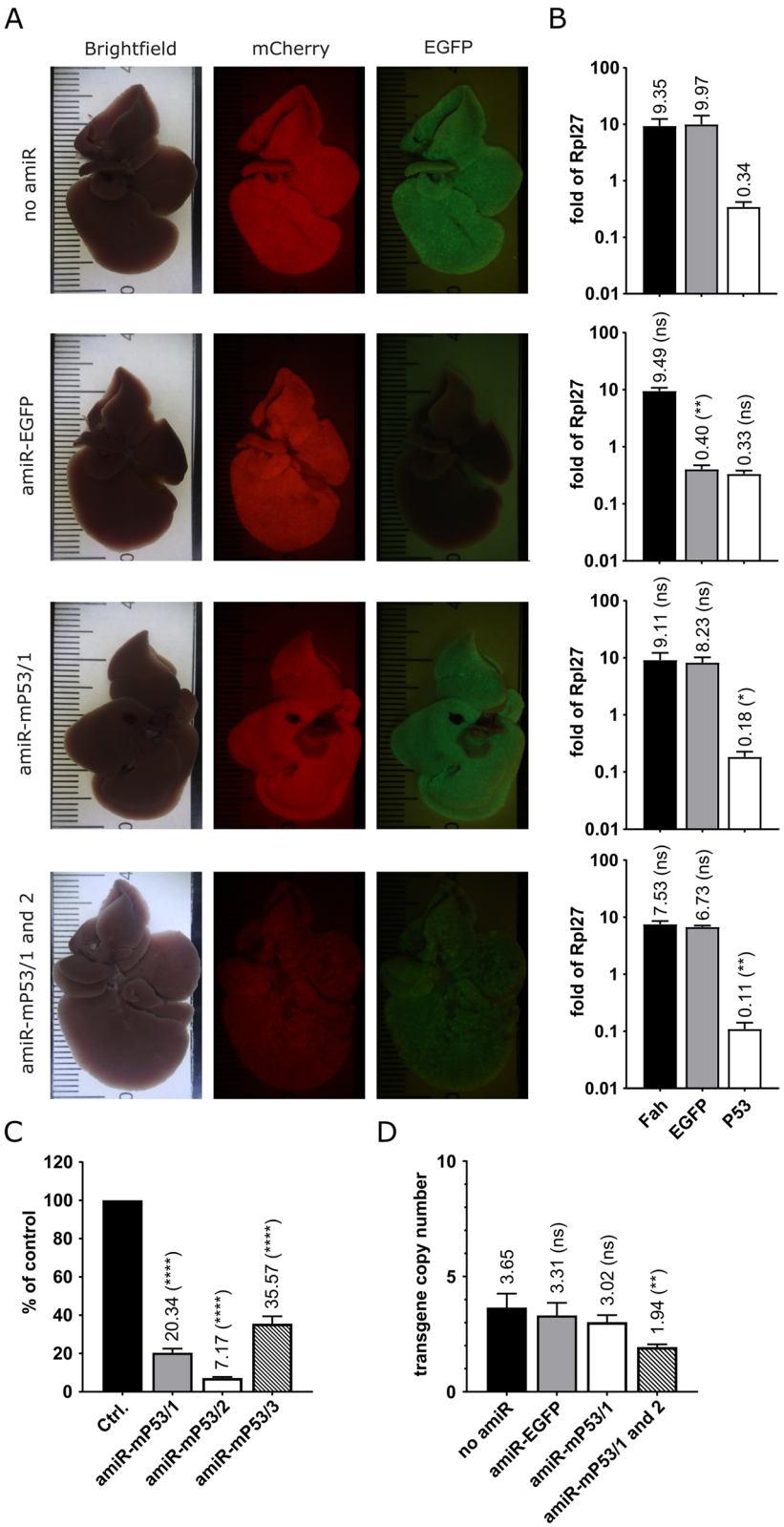

Fig. 2 (See legend on previous page.)

amiR-free EGFP-expressing control transposon constructs together with the SB100 transposase helper plasmid were co-delivered hydrodynamically into the liver of *Fah*$^{-/-}$ mice, then NTBC was withdrawn. After 5 weeks, during multi-nodular repopulation, the animals were sacrificed. Immunohistochemical investigations showed that the size of Fah-positive hepatocyte colonies repopulating the liver was larger in livers treated with the driver construct as compared to controls (Fig. 3a). This is consistent with the significantly higher proportion of Fah-positive hepatocytes (94.8% vs. 68.76%) in the driver construct-treated animals as determined by machine learning technology (Fig. 3b). This clearly shows that the division rate of the transformed hepatocytes is markedly higher than that of the regenerating cells in control mice during normal multi-nodular repopulation.

The examination time point at 5 weeks after hydrodynamic injection and NTBC withdrawal represents incomplete multi-nodular repopulation. At this time point, we again monitored the extent of *Tp53* silencing and the levels of transcripts A and B in both driver and control construct-treated animals. Our RT-qPCR measurements revealed 42% remaining *Tp53* expression in organs treated with the driver construct (Fig. 3c). The levels of transcripts A and B in the livers of animals treated with the control construct were very similar to each other (Fig. 3d), comparable to the findings in the later stages following complete multi-nodular repopulation (Figs. 1 c and 2b), whereas a significant decrease in the expression of transcript B (hRas^{G12V}) was observed in organs bearing the driver construct (Fig. 3d).

Experimental animals treated with the driver construct cannot be housed for substantially longer than 5 weeks due to the presence of a large number of transformed hepatocyte clones in their livers. Yet, to demonstrate the appearance of pathological signatures characteristic of tumors of malignant pathological grade using this high-penetrance driver combination, we mixed the transforming construct (1%) with a high amount of a transposon construct expressing the Fah selection marker protein alone (99%). Then, this construct mixture together with the SB100 transposase helper plasmid was co-delivered hydrodynamically into the liver of *Fah*$^{-/-}$ mice. Treated mice sacrificed at 5 months after NTBC withdrawal exhibited a high tumor burden (Additional file 1: Fig. S4). On histological images of their livers, tumor tissue showed high intrinsic fat accumulation typical for hepatocellular carcinoma (HCC) [24, 25] and frequent neoplastic tissue invasion and atypical mitoses were observed (Additional file 1: Fig. S4).

To better characterize the induced tumorigenic processes, immunohistochemical investigations were performed on liver samples from control and driver construct-treated animals. An early time point, 5 weeks post-treatment, and a late time point, 5 months post-treatment, were chosen (Fig. 3a). Samples from animals treated with the 1% transforming construct mixture were used to investigate the long-term effect of the driver construct at 5 months post-treatment. All liver samples from control and driver construct-treated animals were analyzed by immunohistochemical staining for alpha-fetoprotein (Afp), the most commonly used marker of HCC [26], and glypican-3 (Gpc3), one of its early markers [27, 28] (Fig. 3a). Liver samples from mice treated with the control construct did not show positivity for the Gpc3 marker at any of the stages tested (Fig. 3a). In contrast, weak positivity for the Afp marker was observed mainly in early-stage control samples at 5 weeks post-treatment (Fig. 3a). This weak Afp signal is presumably produced in remaining tyrosinemic cells [29, 30]. Interestingly, in the driver construct-treated samples, the majority of transformed hepatocyte colonies already showed Gpc3 positivity at the earlier time point of 5 weeks post-treatment, while Afp positivity was not observed at this stage. Mature tumors, 5 months after treatment, typically showed the presence of both markers tested (Fig. 3a).

(See figure on next page.)

Fig. 3 Induction of HCC using a predefined combination of drivers. **a** Immunohistochemical analysis of the Fah selection marker, Gpc3, and Afp HCC markers in liver sections from *Fah*$^{-/-}$ mice treated with either control (no amiR, EGFP) or driver (amiR-mP53/1, hRas^{G12V}) transposon constructs at 5 weeks and 5 months post-treatment. For the analysis of tumors emerging 5 months after treatment with the driver construct, a vector mixture containing 1% driver transposon vector and 99% transposon vector expressing only the Fah selection marker protein was used. Scale bars, 100 µm. **b** Determination of the percentage of Fah-positive hepatocytes 5 weeks after treatment by machine learning-based measurement. Data were presented as the mean ± SD ($n = 3$) (see Additional file 2 for individual data values and statistics). **c** Monitoring of endogenous p53 mRNA levels in the liver of *Fah*$^{-/-}$ mice treated with driver and control transposon constructs. Liver RNA samples were collected from *Fah*$^{-/-}$ mice at 5 weeks post-treatment and tested using a p53 mRNA-specific RT-qPCR assay. Results were normalized to measurements of the ribosomal protein L27 (*Rpl27*) transcript as input control and data were presented as the mean ± SD ($n = 3$) (see Additional file 2 for individual data values and statistics). **d** Monitoring the amount of transcripts A and B in the liver of *Fah*$^{-/-}$ mice treated with driver and control transposon constructs. Liver RNA samples were collected from *Fah*$^{-/-}$ mice at 5 weeks post-treatment and tested using Fah-, EGFP-, and hRas^{G12V}-specific RT-qPCR assays. Results were normalized to measurements of the ribosomal protein L27 (*Rpl27*) transcript as input control and data were presented as the mean ± SD ($n = 3$) (see Additional file 2 for individual data values and statistics)

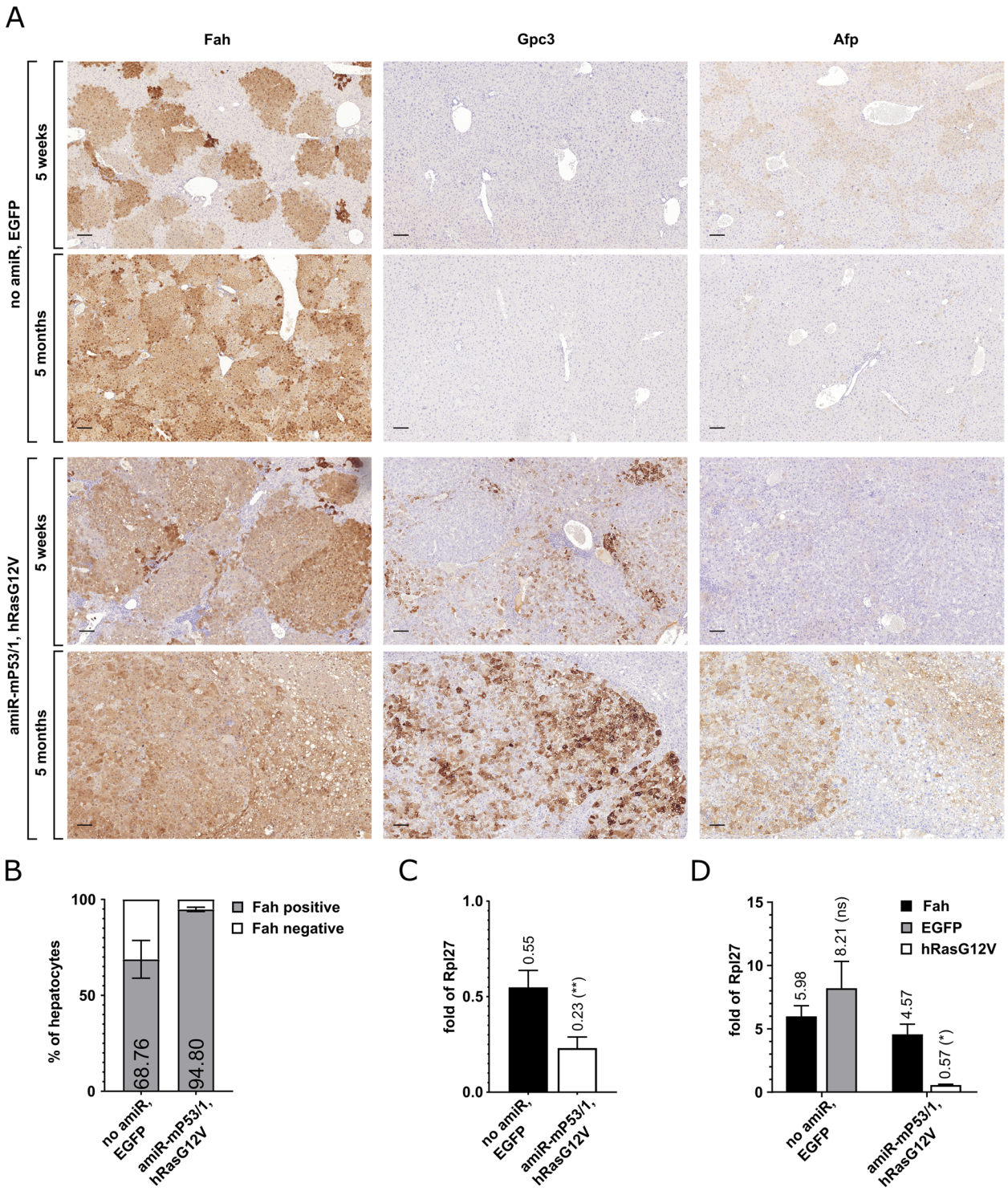

Fig. 3 (See legend on previous page.)

Discussion

The manipulation of the somatic genome in mice is hampered by a number of factors that are essentially the same as those that make it difficult to manipulate the human somatic genome for gene therapy. Transcriptional repression observed with plasmid DNA vectors in the liver is

caused by the formation of repressive heterochromatin on the plasmid DNA, a process initiated with the activation of cytoplasmic exogenous DNA sensors [8, 9]. Some studies suggest that heterochromatin formation occurs via CpG methylation [31, 32], whereas others propose a CpG-independent pathway [33]. As a consequence, transgene expression upon plasmid introduction, even if complemented by SB transposon-based chromosomal gene transfer rapidly declines in the liver [7, 10, 34]. Bell and co-workers demonstrated that even when using SB transposition, several weeks after injection, the transgene expression stabilizes at ~1% of the level at 24 h [10]. According to the results of our own comparative experiment presented here, Luc expression stabilizes at 0.26% of the level measured at day 3 in WT animals (Fig. 1e).

In comparison to the standard hydrodynamic injection method into WT animals, we can state that by exploiting the multi-nodular repopulation in *Fah*-deficient livers, a truly long-lasting and physiological level of gene expression can be achieved, virtually in the entire hepatocyte population of the experimental mice (Fig. 1b, d, e). In *Fah*-deficient animals, Luc expression showed increasing intensity over the 3-month monitoring period, up to 61-fold above the initial level (Fig. 1d, e). This net increase arises from several contributing factors, some acting in opposite directions. The initial activation of DNA sensors presumably cannot be avoided even with the technology described here. Therefore, the main negatively contributing factor is probably transgene heterochromatinization, which almost completely abolishes transgene expression in WT animals. We speculate that using our technology, the transposed transgenes are unlikely to undergo the degree of heterochromatinization required for silencing, probably due to positive selection pressure on Fah marker expression and to cell divisions during liver regeneration. The transient decrease in transgene expression in *Fah* KO animals at day 56 is presumably due to the fact that these downregulation processes are also at work in them, peaking at around day 56 but eventually ceasing (Fig. 1d, e). Another negative contributor is the disappearance of plasmid-derived transgene expression, which is due, among other things, to the loss of plasmids during cell divisions. Presumably, this phenomenon accounts for the lower initial (d3, d7) bioluminescence values measured in *Fah* KO animals (Fig. 1d, e). The main factor positively affecting cumulative transgene expression is the division of transgene-bearing cells. The 61-fold increase in transgene expression could be directly attributed to a similar increase in the number of hepatocytes, which corresponds to roughly 5 cell divisions, if negatively acting factors are excluded. However, as these are also present, more than 5 cell divisions are likely to occur during complete multi-nodular repopulation [12].

The SB transposon system has been used before for *Fah* correction [35]. Some laboratories have also taken significant steps forward to create a versatile gene expression modification system such as the one we present here [36–40]. The first study, and the one most similar to ours, was published by Wangensteen et al. [36]. The other similar studies typically use this vector system or its variants. The technological approach developed by Wangensteen et al. differs in some fundamental points from the one we describe here. The authors of the study used an early variant of amiR design [41] for endogenous gene silencing, which was later improved by others towards the mirE type structure [20]. Notably, this transcriptional unit expressing the early amiR variant was present on a separate transposon vector from the transposon vector expressing the Fah selection marker and the $NRas^{G12V}$ oncogene. Given that the toxicity of amiR elements may be significant [42, 43], target gene silencing was likely to affect only a subset of Fah-corrected $NRas^{G12V}$ expressing cells in regenerating liver tissue. Although this potentially low double feature positive cell count works with penetrant tumor models, it limits experimental applications and precludes settings in which all cells in a tissue need to be manipulated uniformly to draw valid conclusions. An artificial bidirectional promoter was also applied by Wangensteen et al. to connect the expression of the Fah selection marker and the $NRas^{G12V}$ oncogene, but the authors did not provide a detailed characterization of the amount of bidirectional transcripts relative to each other and to an endogenous control. A less effective liver repopulation as compared to our method can also be assumed potentially due to the application of less efficient SB transposase helper variants.

Here we used the hyperactive SB100 transposase helper for more effective chromosomal transgene delivery [11]. When designing our technology platform, we considered it important to allow tag-free expression of proteins of interest in such a way that their expression remains bound to the selection marker. The use of 2A-type peptides is not appropriate for this purpose, as they leave tags on both sides on the two transcriptionally linked proteins [17]. To overcome this challenge, we applied the HADHA/B endogenous bidirectional promoter capable of driving well-balanced bidirectional expression in the physiological range (Figs. 1 c and 2b). The use of HADHA/B gives the possibility for the marker-linked expression of an untagged native protein or a mutant protein isoform at the position of EGFP in transcript B (Fig. 1 a). Bidirectional promoters are more common than thought; a survey of the human genome indicated their widespread occurrence [44, 45]. The HADHA/B promoter is designed by nature to produce two subunits of a protein complex in stoichiometric proportions

[18]. According to our own measurements, the ratio of the two driven transcripts is indeed closer to 1/1 than for any other bidirectional promoter reported so far (Figs. 1c and 2b). In studies of either natural or synthetic bidirectional promoters, if such measurements have been performed at all, bidirectional transcript ratios worse than what we found for HADHA/B have been reported [46–50]. In a single case, we observed a significant shift from the typical 1/1 transcript A to B ratio to a ratio around 8/1 (Fig. 3d). Here the $hRas^{G12V}$ CDS was likely to exert negative selection pressure on the B side of the promoter, while positive pressure was still present on its A side (Fah), and in turn, the connection between the two sides of the promoter was weakened. The 1/1 transcript ratio produced by the HADHA/B bidirectional promoter can be particularly important for protein production when attempting to produce protein complexes.

In addition, we aimed to optimize amiR-based gene silencing in vivo in mouse liver. Importantly, we wanted this feature to be included in the same construct from which the other gene of interest (GOI) is expressed and on which the Fah selection marker is present. Thus, all genetic features are jointly represented in all Fah-corrected liver cells. We have also aimed to position the amiR element in such a way that its maturation does not interfere with the expression of either the selection marker or GOI. In light of this, we decided to place our amiR elements in an intron modified for this purpose. It is well known that in vivo stable gene silencing is not a straightforward technology. The in vivo toxicity of shRNA expression was long ago reported [42]. Similarly, amiR-expressing germline transgenic mice frequently show toxicity and viability issues. Miura and co-workers reported that it was not possible to generate either transgenic mice with higher amiR-expressing constructs or to generate homozygous mice with lower amiR-expressing constructs [43]. The potential reason was the saturation of endogenous miR-processing pathways or other non-specific toxic side effects of the applied amiRs. All these toxic side effects were enhanced with expression level. Here we did not observe severe, non-specific toxicity of gene silencing. In livers expressing the amiR-EGFP element, transcript A levels were virtually identical to those measured in controls not carrying amiR elements. While RT-qPCR measurements revealed only a slight non-significant decrease in levels of transcripts A and B in groups of animals carrying one or two amiR-mP53 elements as compared to controls (Fig. 2b), this slight decrease could be explained by negative selection against strong *Tp53* silencing, which is supported by the decrease in transgene copy number detected in these organs (Fig. 2d). Consequently, the physiological level of transgene expression provided by the human *HADHA/B* promoter in vivo in the mouse liver is compatible with the application of amiR elements.

No sign of tumorigenesis was detected in mice treated with EGFP-expressing transposon constructs either with or without intronic amiR structures. Even in strongly *Tp53* silenced mice carrying double amiR-mP53 elements, no tumor induction was observed. It is worth comparing these data with the published phenotype of *Tp53* KO mice [51]. Heterozygous *Tp53* KO animals rarely developed only lymphoid and testis tumors by 9 months of age, whereas approximately 75% of homozygous KO mice developed various tumors by 6 months of age. The most frequently observed tumors were malignant lymphomas, but no liver tumors were observed at all. Our results are in line with this, as we do not expect the development of hepatocellular carcinoma (HCC) in our experimental system within the given monitoring period even after aggressive *Tp53* silencing. This also implies that SB transposon-mediated random transgene delivery has no or very low oncogenic side effects, meaning that it is not sufficiently tumorigenic by itself to ruin our test system even in the presence of *Tp53* silencing.

Previously, it was shown that upon NTBC withdrawal a small subpopulation of Fah-deficient hepatocytes may be able to avoid elimination during the selection process by activating the survival Akt pathway [52]. Presumably, this phenomenon is responsible for the emergence of tumors from non-corrected Fah-deficient cells reported during retroviral gene therapy treatment of *Fah* KO mice [53]. In our system, such tumors of tyrosinemic cell origin are well distinguishable from marker-positive tumors induced by our transgenes, as they are negative for the mCherry marker. Their development requires the long-term presence of a large number of residual, uncorrected Fah-deficient cells in the liver. The emergence of this can be attributed to two potential causes: the poor efficiency of gene delivery and the use of contraselective transgenes. With the use of highly contraselective transgenes, during multi-nodular repopulation, the growth of nodules expressing these transgenes more strongly is retarded, slowing down the overall repopulation of the liver. Using the hyperactive SB100 transposase helper and non-contraselective transgenes, we do not see these tumors. However, the use of contraselective transgenes may also induce their appearance in our system in the long term. Such mCherry marker-negative tumors emerging from non-corrected Fah-deficient cells were only detected in double amiR-mP53 carrying mice at late time points, around 7–10 months post-injection. Consistent with the fact that tyrosinemic cells are prone to cancerous transformation, our measurements revealed that they might exhibit increased levels of *Tp53* expression as well. *Tp53* expression was measured in control (no amiR,

EGFP) animals at two time points, during multi-nodular repopulation, at 5 weeks after injection (Fig. 3c), and well after the completion of multi-nodular repopulation, at 5 months after injection (Fig. 2b). These RT-qPCR measurements revealed significantly higher *Tp53* expression levels in the first case (0.55-fold of Rpl27) at a considerable tyrosinemic (*Fah* KO) cell content than in the second case (0.34-fold of Rpl27), where tyrosinemic cells are already virtually absent.

Hepatocellular carcinoma (HCC) is one of the most lethal cancers worldwide; however, the genetic mechanisms underlying its pathogenesis are incompletely understood. We aimed to demonstrate the potential of our technology for cancer research by transforming mouse hepatocytes with the well-known *Tp53* tumor suppressor and *hRas* oncogene driver combination. Oncogenic hRas expression is able to trigger senescence in primary cells [54]. Therefore, their transformation by h*Ras* requires either a cooperating oncogene or the inactivation of a tumor suppressor [54, 55]. In accordance, ectopic expression of $hRas^{G12V}$ alone is insufficient to induce tumorigenesis. Thus, tumor development in our system alone demonstrates the combined manifestation of both cancer-driving genetic manipulations.

HCC characteristic of the induced tumors is well demonstrated by their Gpc3 and Afp immunoreactivity (Fig. 3a). It should also be noted that the presence of the Gpc3 marker, which can be used to distinguish early-stage HCC from dysplastic nodules [28], can already be detected in the majority of transformed hepatocyte colonies at the earlier examination time point, 5 weeks post-treatment (Fig. 3a).

The experimental potential created by our technology platform is not fully demonstrated by the *Tp53*-silenced and $hRas^{G12V}$-overexpressing tumor model. For the application of this highly penetrant driver combination, wild-type mice are also suitable, as it is sufficient to produce a small number of cells here that survive p53 silencing and overexpress $hRas^{G12V}$ to induce tumors. The high penetrance of oncogenic *Ras* mutations is a phenomenon parallel to the high incidence of *RAS* mutations in human cancer. Approximately 19% of patients with cancer harbor *RAS* mutations, equivalent to approximately 3.4 million new cases per year worldwide [56]. However, the current priority in cancer research is the functional validation of candidate driver genes with lower mutation frequencies in cancer genome databases. Such driver genes, when mutated, are likely to induce tumors at lower penetrance and may appear as germline or somatically mutated driver genes in hereditary as well as sporadic cancers [57]. The nearly 100 million testable hepatocytes available in our platform in a single experimental animal allow to functionally test even such driver genes with low-penetrance driver mutations.

Conclusions

In this study, we developed a somatic gene delivery technology enabling long-lasting and high-level transgene expression in the entire hepatocyte population of mice. We also presented comparative studies to demonstrate that our approach is superior to conventional methods. Our technology allows the tag-free expression of proteins of interest and silencing of any arbitrary gene in the mouse genome using amiR elements. Achieving these has been aided by the use of the endogenous HADHA/B promoter capable of driving well-balanced bidirectional expression and by optimizing in vivo intronic amiR-based gene silencing. The HADHA/B promoter has not been part of the biotechnology toolkit until now. Here we provide a detailed characterization of its functionality in an in vivo setting. Eventually, we developed a versatile technology platform for in vivo somatic genome editing in the mouse liver that simultaneously meets multiple requirements. We expect it will contribute to gene function analysis in mice by generating new, more accurate genetic models.

Methods

Animal care and maintain

Mice were bred and maintained in the Central Animal House at the Biological Research Centre (Szeged, Hungary). The specific pathogen-free status was confirmed quarterly according to FELASA (Federation for Laboratory Animal Science Associations) recommendations [58]. Mice were housed under 12-h light-dark cycle at 22 °C with free access to water and regular rodent chow. All animal experiments were conducted according to the protocols approved by the Institutional Animal Care and Use Committee at the Biological Research Centre. The used *Fah* mutant line, C57BL/6N-$Fah^{tm1(NCOM)Mfgc/Biat}$, is archived in the European Mouse Mutant Archive (EMMA) under EM:10787. $Fah^{-/-}$ mice were treated with 8 mg/l Orfadin®(Nitisinone, NTBC) (Swedish Orphan Biovitrum) in drinking water. After hydrodynamic injection, NTBC was withdrawn. C57BL/6NTac wild-type mice were obtained from Taconic Biosciences.

Plasmid construction

Empty pbiLiv-miR vector was synthesized and cloned in a pUC57 plasmid backbone by GeneScript. This encompasses the bidirectional promoter of the human hydroxyacyl-CoA dehydrogenase trifunctional multienzyme complex alpha (HADHA) and beta (HADHB) subunits. The HADHA side of the bidirectional promoter drives expression of the mCherry fluorescent marker gene,

which is disrupted by the first intron of the human eukaryotic translation elongation factor 1 alpha 1 (*EEF1A1*) to ensure intronic expression of the designed amiR structures. Restriction endonuclease recognition sites were introduced into the EEF1A1 intron to clone amiR elements as follows: AgeI, XbaI, SacI, and SalI. The mCherry coding sequence (CDS) is linked to the mouse fumaryl-aceto-acetate dehydrogenase (*Fah*) CDS by a T2A peptide to provide bicistronic expression. The transcription unit ends with a bGH polyadenylation signal. The HADHB side of the bidirectional promoter is flanked by an MCS followed by a bGH polyadenylation signal. The whole arrangement is flanked by the T2 type SB transposon inverted terminal repeats [14].

To generate pbiLiv-miR-EGFP, the PCR amplified EGFP coding sequence was inserted into the BamHI/PacI sites of the MCS in pbiLiv-miR. pbiLiv-miR-EGFP-EGFP and pbiLiv-miR-mP53/1-EGFP were constructed by inserting the complete amiR-EGFP or amiR-mp53/1 element into the AgeI/XbaI site of pbiLiv-miR-EGFP. pbiLiv-miR-mP53/1,2-EGFP was constructed by inserting the complete amiR-mP53/2 element into the SacI/SalI sites of pbiLiv-miR-mP53/1-EGFP. Complete amiR-EGFP, amiR-mp53/1, amiR-mp53/2, and amiR-mp53/3 elements (Additional file 1: Fig. S1) flanked by AgeI, SacI, XbaI, and SalI sites were synthesized and cloned in a pUC57 plasmid backbone by GeneScript.

To generate pbiLiv-miR-Luc, the Luciferase encoding gene was amplified by PCR from plasmid pGL3-Basic (Promega) and inserted into the NheI/PacI sites of the MCS in pbiLiv-miR.

For constructing pbiLiv-miR-mP53/1-hRas^{G12V}, hRas coding sequence was PCR amplified from mouse total liver RNA and cloned into the pBluescript SK plasmid. G12V mutation was introduced by the QuickChange Site Directed Mutagenesis Kit (Agilent Technologies). The mutated hRas coding sequence was then inserted into the BamHI/PacI sites of the MCS in pbiLiv-miR. Next, the amiR-mP53/1 element was inserted into the AgeI/XbaI sites of the hRas^{G12V}-containing pbiLiv-miR.

pNeo-miR was constructed by inserting the first intron of the *EEF1A1* with the AgeI, XbaI, SacI, and SalI restriction endonuclease recognition sites into pT2-SVNeo (Addgene #26553). The pNeo-miR-mP53 plasmid series was constructed by inserting the amiR-mP53/1, amiR-mP53/2, and amiR-mP53/3 amiR structures into the AgeI/XbaI sites of pNeo-miR. pcGlobin2-SB100 was constructed as described [11].

Hydrodynamic tail vein injection

Plasmids for hydrodynamic tail vein injection were prepared using the NucleoBond Xtra Maxi Plus EF Kit (Macherey-Nagel) according to the manufacturer's instructions. Before injection, we diluted plasmid DNA in Ringer's solution (0.9% NaCl, 0.03% KCl, 0.016% $CaCl_2$) and a volume equivalent to 10% of mouse body weight was administered via the lateral tail vein in 5–8 s into 6–8-week-old mice [10, 59]. The amount of plasmid DNA was 50 μg for each of the constructs mixed with 4 μg of the transposase helper plasmid.

RNA extraction and gene expression analysis

Total RNA from 50 mg liver tissue was isolated using TRI Reagent (MRC) following the manufacturer's protocol. RNA was Dnase I treated with PerfeCTa DNase I (Quantabio) and reverse transcribed into cDNA using RevertAid First Strand cDNA Synthesis Kit (ThermoFisher Scientific). RT-qPCR was performed on a Rotor-Gene Q instrument (Qiagen) with PerfeCTa SYBR Green SuperMix (Quantabio) as follows: 95 °C for 7 min followed by 35 cycles of 20 s at 95 °C, 20 s at 60 °C, and 20 s at 72 °C. All reactions were carried out in triplicates in a final volume of 20 μl. The following primers were used:

mP53-F: ACTTACCAGGGCAACTATGGCT; mP53-R: GCTGGCAGAATAGCTTATTGAGG; EGFP-F: GAGCAAAGACCCCAACGAGA; EGFP-R: CACCTCGAGCTACAGCTTCT; mFah-F: CTGGGTCAAGCTGCATGGAA; mFah-R: AGGAAGGTGCATTGTCGCAG; Rpl27-F: AAGCCGTCATCGTGAAGAACA; Rpl27-R: CTTGATCTTGGATCGCTTGGC [60].

PCR efficiencies were analyzed with Rotor-Gene Q software (Qiagen). Gene expression was analyzed by the normalization of expression to that of ribosomal protein L27 (*Rpl27*) using the ΔCT method [61].

Genomic DNA isolation and transgene copy number assessment

Whole livers of treated animals were lysed in 150 ml lysis buffer (100 mM TRIS-HCl pH8, 5 mM EDTA pH8, 200 mM NaCl, 0.2% SDS) and incubated overnight at 50 °C in the presence of 300 μg/ml ProteinaseK (VWR Chemicals). DNA from 1 ml lysate was isolated by conventional phenol/chloroform extraction and ethanol precipitation.

The assessment of transgene copy number was done by qPCR. Primers for Fah were the same as for the analysis of mRNA amount. PerfeCTa SYBR Green SuperMix (Quantabio) was used to carry out qPCR reactions on a Rotor-Gene Q instrument (Qiagen). All reactions were carried out in triplicates using 30 ng gDNA. Cycling conditions were as follows: 95 °C for 7 min followed by 35 cycles of 20 s at 95 °C, 20 s at 64 °C, and 20 s at 72 °C. PCR efficiencies were analyzed with Rotor-Gene Q software

(Qiagen). Relative changes in DNA levels were calculated using the ΔCT method. Results were normalized to measurements of the *Olfr16* gene. The following primers were used for this: Olfr16-F: GAGTTCGTCTTCCTGGGATTC; Olfr16-R: TAATGATGTTGCCAGCCAGA [62].

Stereomicroscope imaging

Pictures of whole mouse livers were taken with an Olympus SZX12 fluorescence stereozoom microscope equipped with a 100-W mercury lamp and filter sets for selective excitation and emission of GFP and mCherry.

In vivo bioluminescence imaging

In vivo bioluminescence imaging was performed using an IVIS Lumina III instrument (PerkinElmer). Following the intraperitoneal administration of 150 mg/kg luciferase substrate (XenoLight D-Luciferin-K+ salt, PerkinElmer), mice were anesthetized using isoflurane (Isoflurin, Vetpharma) and imaged at 10 min post-injection. Emitted photons were quantified with an exposure time of 1 to 10 s. Quantification of average radiance (photons per second per cm^2 per steradian (sr) [$p/s/cm^2/sr$]) within a circular region of interest was performed using the Living Image software (PerkinElmer).

Immunohistochemistry

Mice were sacrificed at 5 weeks, 3 months, or 5 months post-injection. Livers were removed and fixed overnight in 4% formalin, then embedded in paraffin, and cut into 5-µm sections. Immunohistochemistry was performed using the EnVision FLEX Mini Kit (DAKO). Antigen retrieval was done in a PT Link machine (DAKO). The primary antibodies used for immunohistochemistry are rabbit polyclonal anti-FAH (ThermoFisher Scientific, PA5-42049, 1:100), incubated for 120 min, and rabbit polyclonal anti-alpha 1 fetoprotein (Abcam, ab46799, 1:500) and rabbit polyclonal anti-glypican 3 (Abcam, ab186872, 1:800), incubated overnight. Secondary antibody polyclonal goat anti-rabbit-HRP (DAKO, P0448) was incubated for 30 min. Visualization was done with EnVision FLEX DAB+ Chromogen System (DAKO, GV825). After hematoxylin counterstaining for 5 min, slides were mounted and scanned with a Pannoramic Digital Slide Scanner (3D Histech).

Image analysis pipeline

3D Histech generated images were processed using BIAS software. A pipeline was created for the analysis consisting of four major steps: (1) pre-processing of the images, (2) segmentation and (3) feature extraction, and (4) cell classification using machine learning. In the pre-processing, non-uniform illumination was corrected using the CIDRE method [63]. The deep learning segmentation method was applied to detect and segment individual nuclei in images. With segmentation post-processing, two additional regions were defined for each nucleus: (1) a region representing the entire cell was defined by extending nuclei regions with a maximum 5 µm radius so that adjacent cells did not overlap and (2) cytoplasmic regions were defined by subtracting nuclei segmentation from the cell segmentation. Finally, morphological properties of these three different regions as well as intensity and texture features from all channels were extracted (in total 228 features) for cell classification. We employed supervised machine learning to predict four different cell types: FAH-positive cells, FAH-negative cells, immune cells, and other cells or segmentation artifacts that can be considered trash. These classes were manually selected based on their morphological characteristics. Cells with evenly distributed brown chromogen signal (anti-FAH staining) across the whole cells were labeled as FAH positive, while cells without chromogen staining were labeled as FAH negative. Cells with small and dark blue nuclei were considered as lymphocyte-like immune cells. Small segmented regions outside the tissue section were also classified as trash. For the training set, we annotated around 200 cells for each class from different tissue sections. Support Vector Machine (SVM) was trained with a radial basis function kernel commonly used for the multi-class cell phenotype classification. After training the SVM model, a 10-fold cross-validation was used to determine the expected accuracy of the model. We used this trained model to predict a class for all other cells in each liver section.

Protein extraction and Western blotting

Fifty milligrams of liver tissue was dounce homogenized in 2 ml radioimmunoprecipitation assay (RIPA) buffer (10 mmol/l Tris-HCl, pH 8.0, 1 mmol/l EDTA, 0.5 mmol/l EGTA, 1% Triton X-100, 0.1% sodium deoxycholate, 0.1% SDS, 140 mmol/l NaCl), supplemented with PMSF (Merck). Cleared samples were sonicated for 3×10 s. Protein concentrations were calculated using the Pierce™ BCA Protein Assay kit (ThermoFisher Scientific). A total of 80 µg of protein was separated on 10% SDS-PAGE gel, transferred to a 0.2-µm nitrocellulose membrane (Amersham), and blocked with 5% non-fat dry milk in Tris-buffered saline-Tween 20 (TBS-T) for 1 h at room temperature. Blocked membranes were incubated with anti-GFP (Abcam, ab6556, 1:4000) and peroxidase-conjugated anti-GAPDH (ThermoFisher Scientific, MA5-15738-HRP,1:10000) antibodies. Anti-rabbit IgG conjugated to horseradish peroxidase (HRP) (Sigma Aldrich, A0545, 1:20000) was used as the secondary antibody where necessary. Immune complexes detected with

enhanced chemiluminescence (ECL) Prime Western blotting Detection Reagent (Amersham).

Cell culture and transfection

NIH/3T3 cells were purchased from ATCC and cultured in Dulbecco's modified Eagle's medium (DMEM) (Biosera) supplemented with 10% fetal bovine serum (FBS; Gibco) and 1% penicillin-streptomycin (P-S; HyClone) in the presence of 5% CO_2 at 37 °C.

Cells were transfected with 500 ng of either pNeo-miR or pNeo-miR-mP53/1 or pNeo-miR-mP53/2 or pNeo-miR-mP53 in combination with 50 ng of the transposase helper plasmid, using FuGENE® HD transfection reagent (Promega) according to manufacturer's instructions. Selection of stable transfected cells was performed using neomycin (G418; Biosera).

Data visualization and statistics

GraphPad Prism software (version 8.4.3 for Windows, GraphPad Software) was used for data visualization. Statistics were calculated using Fisher's exact and Pearson's chi-squared test.

To identify levels of statistical significance (*P* value), one-way ANOVA tests were performed for the comparison of RT-qPCR measurements of different sample groups and for the comparison of two sample groups the Welch's *t*-test was applied. The threshold for significance was $P<0.05$.

Abbreviations

Afp	Alpha-fetoprotein
AIM2	Absent in melanoma 2
amiR	Artificial microRNA
CDS	Coding sequence
cGAS	Cyclic GMP-AMP synthase
EEF1A1	Eukaryotic translation elongation factor 1 alpha 1
EGFP	Enhanced green fluorescent protein
Fah	Fumarylacetoacetate hydrolase
GOI	Gene of interest
Gpc3	Glypican-3
HADHA/B	Hydroxyacyl-CoA dehydrogenase trifunctional multienzyme complex alpha and beta subunits
HCC	Hepatocellular carcinoma
IHC	Immunohistochemistry
ITR	Inverted terminal repeat
KO	Knock out
Luc	Firefly luciferase
miR	MicroRNA
NTBC	2-(2-Nitro-4-trifluoromethylbenzoyl)-1,3-cyclohexanedione (Orfadin®, Nitisinon)
Rpl27	Ribosomal protein 27
RT-qPCR	Quantitative reverse transcription PCR
SB	Sleeping Beauty transposon
shRNA	Short hairpin RNA
TLR9	Toll-like receptor 9
WT	Wild type

Supplementary Information

The online version contains supplementary material available at https://doi.org/10.1186/s12915-022-01262-x.

Additional file 1: Fig. S1. The structure of the applied amiR elements. **Fig. S2.** Detection of the EGFP protein in mouse liver. **Fig. S3.** SB transposon-based cloning platform for the expression of amiR elements in cultured cells. **Fig. S4.** Stereomicroscopic and histological examination of liver samples 5 months after treatment with a construct mixture containing 1% transforming construct.

Additional file 2. Individual data values and statistics for Figures 1-3.

Acknowledgements

The authors thank the staff of the Cellular Imaging Laboratory of the Biological Research Centre for the provided microscopy support.

Consent to participate

Not applicable.

Authors' contributions

LM contributed to the conception and design. LM and AN contributed to the writing, review, and revision of the manuscript with input from all authors. LM contributed to the analysis and interpretation of data with help from IO, LGP, PH, and FS. RK, LH, and GI performed the animal experiments. GI performed the IVIS Lumina imaging. AGK, DZP, IF, and VED participated in the construction and purification of plasmids. AGK, DZP, PG, ABD, and AM carried out qPCR and RT-qPCR experiments. GPB and KSAA performed the immunohistochemistry. EM and AK performed the image analysis. DZP, VED, and AGK carried out the cell culture experiments. AGK and RK performed the Western blot experiment. LM contributed to the study supervision. All authors read and approved the final manuscript.

Funding

This work was supported by the Momentum Programme of the Hungarian Academy of Sciences [LP2015-5/2015] and by the National Research, Development and Innovation Office (Hungary) grant [GINOP-2.3.2-15-2016-00024]. PH, EM, and AK acknowledge support from the LENDULET-BIOMAG Grant [2018-342], from the European Regional Development Fund (GINOP-2.3.2-15-2016-00026), from COMPASS-ERA PerMed H2020, from CZI Deep Visual Proteomics, from H2020-DiscovAir, and from ELKH-Excellence grant. RK was supported by the ÚNKP-20-3-SZTE-84 New National Excellence Program of the Ministry for Innovation and Technology from the source of the National Research, Development and Innovation Fund. AGK was supported by the Szeged Scientists Academy under the sponsorship of the Hungarian Ministry of Innovation and Technology (*FEIF/646-4/2021-ITM_SZERZ*) and the New National Excellence Program of the Ministry for Innovation and Technology of Hungary (*ÚNKP-20-2 –SZTE-438*). Open access funding provided by ELKH Biological Research Center.

Availability of data and materials

All data generated or analyzed during this study are included in this published article and supplementary information files. Individual data values and statistics are provided in Additional file 2. Presented qPCR experiments comply with the MIQE Guidelines. Necessary details for evaluation are supplied in the "Methods" section of the manuscript. The exact sequences of artificial microRNA structures used are provided in Additional file 1: Fig. S1.

Declarations

Ethics approval

Animal experimental procedures were approved and performed in accordance with the guidelines of the Institutional Animal Care and Use Committee at the Biological Research Centre (Szeged, Hungary) under the supervision of the Governmental Office for Csongrád County, Directorate of Food Chain Safety and Animal Health. The approval number is XVI./801/2018.

Consent for publication
Not applicable.

Competing interests
The authors declare that they have no competing interests.

Author details
[1]Institute of Genetics, Biological Research Centre, Szeged, Hungary. [2]Doctoral School of Biology, University of Szeged, Szeged, Hungary. [3]Doctoral School of Multidisciplinary Medical Sciences, University of Szeged, Szeged, Hungary. [4]Institute of Pathology, University of Szeged, Szeged, Hungary. [5]Synthetic and Systems Biology Unit, Institute of Biochemistry, Biological Research Centre, Szeged, Hungary. [6]Department of Biochemistry, University of Szeged, Szeged, Hungary. [7]Institute for Molecular Medicine Finland (FIMM), University of Helsinki, Helsinki, Finland.

Received: 25 August 2021 Accepted: 22 February 2022
Published online: 01 April 2022

References

1. Whitelaw CB, Springbett AJ, Webster J, Clark J. The majority of G0 transgenic mice are derived from mosaic embryos. Transgenic Res. 1993;2(1):29–32. https://doi.org/10.1007/BF01977678 PubMed PMID: 8513336.
2. Garrick D, Fiering S, Martin DI, Whitelaw E. Repeat-induced gene silencing in mammals. Nat Genet. 1998;18(1):56–9. https://doi.org/10.1038/ng0198-56 PubMed PMID: 9425901.
3. Limberis MP, Bell CL, Heath J, Wilson JM. Activation of transgene-specific T cells following lentivirus-mediated gene delivery to mouse lung. Mol Ther. 2010;18(1):143–50. https://doi.org/10.1038/mt.2009.190 PubMed PMID: 19724265; PubMed Central PMCID: PMCPMC2839217.
4. Zhu J, Huang X, Yang Y. Innate immune response to adenoviral vectors is mediated by both Toll-like receptor-dependent and -independent pathways. J Virol. 2007;81(7):3170–80. https://doi.org/10.1128/JVI.02192-06 PubMed PMID: 17229689; PubMed Central PMCID: PMCPMC1866082.
5. Liu L, Zern MA, Lizarzaburu ME, Nantz MH, Wu J. Poly (cationic lipid)-mediated in vivo gene delivery to mouse liver. Gene Ther. 2003;10(2):180–7. https://doi.org/10.1038/sj.gt.3301861 PubMed PMID: 12571647.
6. Lecocq M, Andrianaivo F, Warnier MT, Wattiaux-De Coninck S, Wattiaux R, Jadot M. Uptake by mouse liver and intracellular fate of plasmid DNA after a rapid tail vein injection of a small or a large volume. J Gene Med. 2003;5(2):142–56. https://doi.org/10.1002/jgm.328 PubMed PMID: 12539152.
7. Herweijer H, Zhang G, Subbotin VM, Budker V, Williams P, Wolff JA. Time course of gene expression after plasmid DNA gene transfer to the liver. J Gene Med. 2001;3(3):280–91. https://doi.org/10.1002/jgm.178 PubMed PMID: 11437333.
8. Broz P, Dixit VM. Inflammasomes: mechanism of assembly, regulation and signalling. Nat Rev Immunol. 2016;16(7):407–20. https://doi.org/10.1038/nri.2016.58 PubMed PMID: 27291964.
9. Pandey S, Kawai T, Akira S. Microbial sensing by Toll-like receptors and intracellular nucleic acid sensors. Cold Spring Harb Perspect Biol. 2014;7(1):a016246. https://doi.org/10.1101/cshperspect.a016246 PubMed PMID: 25301932; PubMed Central PMCID: PMCPMC4292165.
10. Bell JB, Podetz-Pedersen KM, Aronovich EL, Belur LR, McIvor RS, Hackett PB. Preferential delivery of the Sleeping Beauty transposon system to livers of mice by hydrodynamic injection. Nat Protoc. 2007;2(12):3153–65. https://doi.org/10.1038/nprot.2007.471 PubMed PMID: 18079715; PubMed Central PMCID: PMCPMC2548418.
11. Mates L, Chuah MK, Belay E, Jerchow B, Manoj N, Acosta-Sanchez A, et al. Molecular evolution of a novel hyperactive Sleeping Beauty transposase enables robust stable gene transfer in vertebrates. Nat Genet. 2009;41(6):753–61. https://doi.org/10.1038/ng.343ng.343 Epub 2009/05/05. [pii]. PubMed PMID: 19412179.
12. Overturf K, Al-Dhalimy M, Tanguay R, Brantly M, Ou CN, Finegold M, et al. Hepatocytes corrected by gene therapy are selected in vivo in a murine model of hereditary tyrosinaemia type I. Nat Genet. 1996;12(3):266–73. https://doi.org/10.1038/ng0396-266 PubMed PMID: 8589717.
13. Zhang G, Gao X, Song YK, Vollmer R, Stolz DB, Gasiorowski JZ, et al. Hydroporation as the mechanism of hydrodynamic delivery. Gene Ther. 2004;11(8):675–82. https://doi.org/10.1038/sj.gt.3302210 PubMed PMID: 14724673; PubMed Central PMCID: PMCPMC4412368.
14. Cui Z, Geurts AM, Liu G, Kaufman CD, Hackett PB. Structure-function analysis of the inverted terminal repeats of the sleeping beauty transposon. J Mol Biol. 2002;318(5):1221–35. https://doi.org/10.1016/s0022-2836(02)00237-1 PubMed PMID: 12083513.
15. Skipper KA, Andersen PR, Sharma N, Mikkelsen JG. DNA transposon-based gene vehicles - scenes from an evolutionary drive. J Biomed Sci. 2013;20:92. https://doi.org/10.1186/1423-0127-20-92 PubMed PMID: 24320156; PubMed Central PMCID: PMCPMC3878927.
16. Lehmann K, Tschuor C, Rickenbacher A, Jang JH, Oberkofler CE, Tschopp O, et al. Liver failure after extended hepatectomy in mice is mediated by a p21-dependent barrier to liver regeneration. Gastroenterology. 2012;143(6):1609–19 e4. https://doi.org/10.1053/j.gastro.2012.08.043 PubMed PMID: 22960658.
17. Szymczak AL, Vignali DA. Development of 2A peptide-based strategies in the design of multicistronic vectors. Expert Opin Biol Ther. 2005;5(5):627–38. https://doi.org/10.1517/14712598.5.5.627 PubMed PMID: 15934839.
18. Orii KE, Orii KO, Souri M, Orii T, Kondo N, Hashimoto T, et al. Genes for the human mitochondrial trifunctional protein alpha- and beta-subunits are divergently transcribed from a common promoter region. J Biol Chem. 1999;274(12):8077–84. https://doi.org/10.1074/jbc.274.12.8077 PubMed PMID: 10075708.
19. Beisel CL, Chen YY, Culler SJ, Hoff KG, Smolke CD. Design of small molecule-responsive microRNAs based on structural requirements for Drosha processing. Nucleic Acids Res. 2011;39(7):2981–94. https://doi.org/10.1093/nar/gkq954 PubMed PMID: 21149259; PubMed Central PMCID: PMCPMC3074164.
20. Fellmann C, Hoffmann T, Sridhar V, Hopfgartner B, Muhar M, Roth M, et al. An optimized microRNA backbone for effective single-copy RNAi. Cell Rep. 2013;5(6):1704–13. https://doi.org/10.1016/j.celrep.2013.11.020 PubMed PMID: 24332856.
21. Dow LE, Premsrirut PK, Zuber J, Fellmann C, McJunkin K, Miething C, et al. A pipeline for the generation of shRNA transgenic mice. Nat Protoc. 2012;7(2):374–93. https://doi.org/10.1038/nprot.2011.446 PubMed PMID: 22301776; PubMed Central PMCID: PMCPMC3724521.
22. Baratta JL, Ngo A, Lopez B, Kasabwalla N, Longmuir KJ, Robertson RT. Cellular organization of normal mouse liver: a histological, quantitative immunocytochemical, and fine structural analysis. Histochem Cell Biol. 2009;131(6):713–26. https://doi.org/10.1007/s00418-009-0577-1 PubMed PMID: 19255771; PubMed Central PMCID: PMCPMC2761764.
23. Bos JL. The ras gene family and human carcinogenesis. Mutat Res. 1988;195(3):255–71. https://doi.org/10.1016/0165-1110(88)90004-8 PubMed PMID: 3283542.
24. Berndt N, Eckstein J, Heucke N, Gajowski R, Stockmann M, Meierhofer D, et al. Characterization of lipid and lipid droplet metabolism in human HCC. Cells. 2019;8(5). https://doi.org/10.3390/cells8050512 PubMed PMID: 31137921; PubMed Central PMCID: PMCPMC6562484.
25. Currie E, Schulze A, Zechner R, Walther TC, Farese RV Jr. Cellular fatty acid metabolism and cancer. Cell Metab. 2013;18(2):153–61. https://doi.org/10.1016/j.cmet.2013.05.017 PubMed PMID: 23791484; PubMed Central PMCID: PMCPMC3742569.
26. Gorog D, Regoly-Merei J, Paku S, Kopper L, Nagy P. Alpha-fetoprotein expression is a potential prognostic marker in hepatocellular carcinoma. World J Gastroenterol. 2005;11(32):5015–8. https://doi.org/10.3748/wjg.v11.i32.5015 PdubMed PMID: 16124056; PubMed Central PMCID: PMCPMC4321920.
27. Anatelli F, Chuang ST, Yang XJ, Wang HL. Value of glypican 3 immunostaining in the diagnosis of hepatocellular carcinoma on needle biopsy. Am J Clin Pathol. 2008;130(2):219–23. https://doi.org/10.1309/WMB5PX57Y4P8QCTY PubMed PMID: 18628090.
28. Llovet JM, Chen Y, Wurmbach E, Roayaie S, Fiel MI, Schwartz M, et al. A molecular signature to discriminate dysplastic nodules from early hepatocellular carcinoma in HCV cirrhosis. Gastroenterology. 2006;131(6):1758–67. https://doi.org/10.1053/j.gastro.2006.09.014 PubMed PMID: 17087938.
29. Angileri F, Roy V, Morrow G, Scoazec JY, Gadot N, Orejuela D, et al. Molecular changes associated with chronic liver damage and neoplastic lesions in a murine model of hereditary tyrosinemia type 1. Biochim Biophys

Acta. 2015;1852(12):2603–17. https://doi.org/10.1016/j.bbadis.2015.09.002 PubMed PMID: 26360553.
30. Zerbini C, Weinberg DS, Hollister KA, Perez-Atayde AR. DNA ploidy abnormalities in the liver of children with hereditary tyrosinemia type I. Correlation with histopathologic features. Am J Pathol. 1992;140(5):1111–9 PubMed PMID: 1374592; PubMed Central PMCID: PMCPMC1886502.
31. Yew NS, Zhao H, Przybylska M, Wu IH, Tousignant JD, Scheule RK, et al. CpG-depleted plasmid DNA vectors with enhanced safety and long-term gene expression in vivo. Mol Ther. 2002;5(6):731–8. https://doi.org/10.1006/mthe.2002.0598 PubMed PMID: 12027557.
32. Hodges BL, Taylor KM, Joseph MF, Bourgeois SA, Scheule RK. Long-term transgene expression from plasmid DNA gene therapy vectors is negatively affected by CpG dinucleotides. Mol Ther. 2004;10(2):269–78. https://doi.org/10.1016/j.ymthe.2004.04.018 PubMed PMID: 15294174.
33. Chen ZY, Riu E, He CY, Xu H, Kay MA. Silencing of episomal transgene expression in liver by plasmid bacterial backbone DNA is independent of CpG methylation. Mol Ther. 2008;16(3):548–56. https://doi.org/10.1038/sj.mt.6300399 PubMed PMID: 18253155.
34. Bell JB, Aronovich EL, Schreifels JM, Beadnell TC, Hackett PB. Duration of expression and activity of Sleeping Beauty transposase in mouse liver following hydrodynamic DNA delivery. Mol Ther. 2010;18(10):1796–802. https://doi.org/10.1038/mt.2010.152 PubMed PMID: 20628359; PubMed Central PMCID: PMCPMC2951564.
35. Montini E, Held PK, Noll M, Morcinek N, Al-Dhalimy M, Finegold M, et al. In vivo correction of murine tyrosinemia type I by DNA-mediated transposition. Mol Ther. 2002;6(6):759–69. https://doi.org/10.1006/mthe.2002.0812 PubMed PMID: 12498772.
36. Wangensteen KJ, Wilber A, Keng VW, He Z, Matise I, Wangensteen L, et al. A facile method for somatic, lifelong manipulation of multiple genes in the mouse liver. Hepatology. 2008;47(5):1714–24. https://doi.org/10.1002/hep.22195 PubMed PMID: 18435462; PubMed Central PMCID: PMCPMC5808937.
37. Keng VW, Tschida BR, Bell JB, Largaespada DA. Modeling hepatitis B virus X-induced hepatocellular carcinoma in mice with the Sleeping Beauty transposon system. Hepatology. 2011;53(3):781–90. https://doi.org/10.1002/hep.24091 PubMed PMID: 21374658; PubMed Central PMCID: PMCPMC3079950.
38. Riordan JD, Keng VW, Tschida BR, Scheetz TE, Bell JB, Podetz-Pedersen KM, et al. Identification of rtl1, a retrotransposon-derived imprinted gene, as a novel driver of hepatocarcinogenesis. PLoS Genet. 2013;9(4):e1003441. https://doi.org/10.1371/journal.pgen.1003441 PubMed PMID: 23593033; PubMed Central PMCID: PMCPMC3616914.
39. Wuestefeld T, Pesic M, Rudalska R, Dauch D, Longerich T, Kang TW, et al. A Direct in vivo RNAi screen identifies MKK4 as a key regulator of liver regeneration. Cell. 2013;153(2):389–401. https://doi.org/10.1016/j.cell.2013.03.026 PubMed PMID: 23582328.
40. Tschida BR, Temiz NA, Kuka TP, Lee LA, Riordan JD, Tierrablanca CA, et al. Sleeping Beauty insertional mutagenesis in mice identifies drivers of steatosis-associated hepatic tumors. Cancer Res. 2017;77(23):6576–88. https://doi.org/10.1158/0008-5472.CAN-17-2281 PubMed PMID: 28993411; PubMed Central PMCID: PMCPMC5712258.
41. Dickins RA, Hemann MT, Zilfou JT, Simpson DR, Ibarra I, Hannon GJ, et al. Probing tumor phenotypes using stable and regulated synthetic microRNA precursors. Nat Genet. 2005;37(11):1289–95. https://doi.org/10.1038/ng1651 PubMed PMID: 16200064.
42. Grimm D, Streetz KL, Jopling CL, Storm TA, Pandey K, Davis CR, et al. Fatality in mice due to oversaturation of cellular microRNA/short hairpin RNA pathways. Nature. 2006;441(7092):537–41. https://doi.org/10.1038/nature04791 PubMed PMID: 16724069.
43. Miura H, Inoko H, Tanaka M, Nakaoka H, Kimura M, Gurumurthy CB, et al. Assessment of artificial MiRNA architectures for higher knockdown efficiencies without the undesired effects in mice. PLoS One. 2015;10(8):e0135919. https://doi.org/10.1371/journal.pone.0135919 PubMed PMID: 26285215; PubMed Central PMCID: PMCPMC4540464.
44. Adachi N, Lieber MR. Bidirectional gene organization: a common architectural feature of the human genome. Cell. 2002;109(7):807–9. https://doi.org/10.1016/s0092-8674(02)00758-4 PubMed PMID: 12110178.
45. Trinklein ND, Aldred SF, Hartman SJ, Schroeder DI, Otillar RP, Myers RM. An abundance of bidirectional promoters in the human genome. Genome Res. 2004;14(1):62–6. https://doi.org/10.1101/gr.1982804 PubMed PMID: 14707170; PubMed Central PMCID: PMCPMC314279.
46. Amendola M, Venneri MA, Biffi A, Vigna E, Naldini L. Coordinate dual-gene transgenesis by lentiviral vectors carrying synthetic bidirectional promoters. Nat Biotechnol. 2005;23(1):108–16. https://doi.org/10.1038/nbt1049 PubMed PMID: 15619618.
47. He K, Rad S, Poudel A, McLellan AD. Compact bidirectional promoters for dual-gene expression in a Sleeping Beauty transposon. Int J Mol Sci. 2020;21(23). https://doi.org/10.3390/ijms21239256 PubMed PMID: 33291599; PubMed Central PMCID: PMCPMC7731152.
48. Andrianaki A, Siapati EK, Hirata RK, Russell DW, Vassilopoulos G. Dual transgene expression by foamy virus vectors carrying an endogenous bidirectional promoter. Gene Ther. 2010;17(3):380–8. https://doi.org/10.1038/gt.2009.147 PubMed PMID: 19907502; PubMed Central PMCID: PMCPMC3739712.
49. Golding MC, Mann MR. A bidirectional promoter architecture enhances lentiviral transgenesis in embryonic and extraembryonic stem cells. Gene Ther. 2011;18(8):817–26. https://doi.org/10.1038/gt.2011.26 PubMed PMID: 21390068.
50. Na M, Fan X. Design of Ad5F35 vectors for coordinated dual gene expression in candidate human hematopoietic stem cells. Exp Hematol. 2010;38(6):446–52. https://doi.org/10.1016/j.exphem.2010.03.007 PubMed PMID: 20303383.
51. Donehower LA, Harvey M, Slagle BL, McArthur MJ, Montgomery CA Jr, Butel JS, et al. Mice deficient for p53 are developmentally normal but susceptible to spontaneous tumours. Nature. 1992;356(6366):215–21. https://doi.org/10.1038/356215a0 PubMed PMID: 1552940.
52. Orejuela D, Jorquera R, Bergeron A, Finegold MJ, Tanguay RM. Hepatic stress in hereditary tyrosinemia type 1 (HT1) activates the AKT survival pathway in the fah-/- knockout mice model. J Hepatol. 2008;48(2):308–17. https://doi.org/10.1016/j.jhep.2007.09.014 PubMed PMID: 18093685.
53. Grompe M, Overturf K, Al-Dhalimy M, Finegold M. Therapeutic trials in the murine model of hereditary tyrosinaemia type I: a progress report. J Inherit Metab Dis. 1998;21(5):518–31. https://doi.org/10.1023/a:1005462804271 PubMed PMID: 9728332.
54. Serrano M, Lin AW, McCurrach ME, Beach D, Lowe SW. Oncogenic ras provokes premature cell senescence associated with accumulation of p53 and p16INK4a. Cell. 1997;88(5):593–602. https://doi.org/10.1016/s0092-8674(00)81902-9 PubMed PMID: 9054499.
55. Ju HL, Ahn SH, Kim DY, Baek S, Chung SI, Seong J, et al. Investigation of oncogenic cooperation in simple liver-specific transgenic mouse models using noninvasive in vivo imaging. PLoS One. 2013;8(3):e59869. https://doi.org/10.1371/journal.pone.0059869 PubMed PMID: 23555816; PubMed Central PMCID: PMCPMC3610734.
56. Prior IA, Hood FE, Hartley JL. The frequency of Ras mutations in cancer. Cancer Res. 2020;80(14):2969–74. https://doi.org/10.1158/0008-5472.CAN-19-3682 PubMed PMID: 32209560; PubMed Central PMCID: PMCPMC7367715.
57. Gohler S, Da Silva Filho MI, Johansson R, Enquist-Olsson K, Henriksson R, Hemminki K, et al. Functional germline variants in driver genes of breast cancer. Cancer Causes Control. 2017;28(4):259–71. https://doi.org/10.1007/s10552-017-0849-3 PubMed PMID: 28238063.
58. Mahler Convenor M, Berard M, Feinstein R, Gallagher A, Illgen-Wilcke B, Pritchett-Corning K, et al. FELASA recommendations for the health monitoring of mouse, rat, hamster, guinea pig and rabbit colonies in breeding and experimental units. Lab Anim. 2014;48(3):178–92 PubMed PMID: Medline:24496575.
59. Portier I, Vanhoorelbeke K, Verhenne S, Pareyn I, Vandeputte N, Deckmyn H, et al. High and long-term von Willebrand factor expression after Sleeping Beauty transposon-mediated gene therapy in a mouse model of severe von Willebrand disease. J Thromb Haemost. 2018;16(3):592–604. https://doi.org/10.1111/jth.13938 PubMed PMID: 29288565.
60. Thomas KC, Zheng XF, Garces Suarez F, Raftery JM, Quinlan KG, Yang N, et al. Evidence based selection of commonly used RT-qPCR reference genes for the analysis of mouse skeletal muscle. PLoS One. 2014;9(2):e88653. https://doi.org/10.1371/journal.pone.0088653 PubMed PMID: 24523926; PubMed Central PMCID: PMCPMC3921188.
61. Livak KJ, Schmittgen TD. Analysis of relative gene expression data using real-time quantitative PCR and the 2(-Delta Delta C(T)) Method. Methods.

2001;25(4):402–8. https://doi.org/10.1006/meth.2001.1262 PubMed PMID: 11846609.
62. D'Hulst C, Parvanova I, Tomoiaga D, Sapar ML, Feinstein P. Fast quantitative real-time PCR-based screening for common chromosomal aneuploidies in mouse embryonic stem cells. Stem Cell Reports. 2013;1(4):350–9. https://doi.org/10.1016/j.stemcr.2013.08.003 PubMed PMID: 24319669; PubMed Central PMCID: PMCPMC3849352.
63. Smith K, Li Y, Piccinini F, Csucs G, Balazs C, Bevilacqua A, et al. CIDRE: an illumination-correction method for optical microscopy. Nat Methods. 2015;12(5):404–6. https://doi.org/10.1038/nmeth.3323 PubMed PMID: 25775044.

Publisher's Note

II.

Nucleic Acids Research, 2024, **52**, 6994–7011
https://doi.org/10.1093/nar/gkae439
Advance access publication date: 3 June 2024
Genome integrity, repair and replication

The loss of DNA polymerase epsilon accessory subunits POLE3–POLE4 leads to BRCA1-independent PARP inhibitor sensitivity

Hasan Mamar[1,2,†], Roberta Fajka-Boja[1,3,†], Mónika Mórocz[4], Eva Pinto Jurado[1,5,6], Siham Zentout[6], Alexandra Mihuţ[1,5], Anna Georgina Kopasz[1,5], Mihály Mérey[1,5], Rebecca Smith[6], Abhishek Bharadwaj Sharma[7], Nicholas D. Lakin[7], Andrew James Bowman[8], Lajos Haracska[4], Sébastien Huet[6] and Gyula Timinszky[1,*]

[1]Laboratory of DNA Damage and Nuclear Dynamics, Institute of Genetics, HUN-REN Biological Research Centre, 6276 Szeged, Hungary
[2]Doctoral School of Biology, University of Szeged, 6720 Szeged, Hungary
[3]Department of Immunology, Albert Szent-Györgyi Medical School, Faculty of Science and Informatics, University of Szeged, 6720 Szeged, Hungary
[4]HCEMM-BRC Mutagenesis and Carcinogenesis Research Group, Institute of Genetics, HUN-REN Biological Research Centre, 6276 Szeged, Hungary
[5]Doctoral School of Multidisciplinary Medical Sciences, University of Szeged, Szeged, Hungary
[6]Univ Rennes, CNRS, IGDR (Institut de génétique et développement de Rennes) - UMR 6290, BIOSITUMS 3480 Rennes, France
[7]Department of Biochemistry, University of Oxford, South Parks Road, Oxford, UK
[8]Division of Biomedical Sciences, Warwick Medical School, University of Warwick, UK

[*]To whom correspondence should be addressed. Tel: +36 62 599 600, Fax: +36 433 503; Email: timinszky.gyula@brc.hu
[†]The first two authors should be regarded as Joint First Authors.
Present address: Rebecca Smith, Sir William Dunn School of Pathology, University of Oxford, Oxford OX1 3RE, UK.

Abstract

The clinical success of PARP1/2 inhibitors (PARPi) prompts the expansion of their applicability beyond homologous recombination deficiency. Here, we demonstrate that the loss of the accessory subunits of DNA polymerase epsilon, POLE3 and POLE4, sensitizes cells to PARPi. We show that the sensitivity of POLE4 knockouts is not due to compromised response to DNA damage or homologous recombination deficiency. Instead, POLE4 loss affects replication speed leading to the accumulation of single-stranded DNA gaps behind replication forks upon PARPi treatment, due to impaired post-replicative repair. POLE4 knockouts elicit elevated replication stress signaling involving ATR and DNA-PK. We find POLE4 to act parallel to BRCA1 in inducing sensitivity to PARPi and counteracts acquired resistance associated with restoration of homologous recombination. Altogether, our findings establish POLE4 as a promising target to improve PARPi driven therapies and hamper acquired PARPi resistance.

Graphical abstract

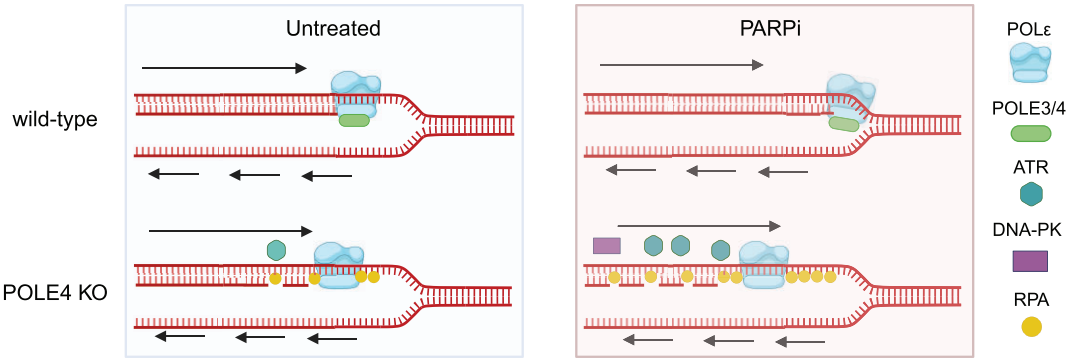

Introduction

PARP inhibitors (PARPi) emerged as a promising therapeutic approach for the treatment of cancers with mutations in the breast cancer susceptibility genes BRCA1/2 nearly two decades ago (1,2). Breast cancer susceptibility protein 1 (BRCA1) and breast cancer susceptibility protein 2 (BRCA2)

Received: September 22, 2023. **Revised:** May 2, 2024. **Editorial Decision:** May 3, 2024. **Accepted:** May 9, 2024

are pivotal for DNA double strand break (DSB) repair via the high-fidelity homologous recombination (HR) pathway. Mutations in the BRCA1/2 genes force the cells to rely on the error-prone non-homologous end joining (NHEJ) DSB repair, which leads to genomic instability (3).

PARP1 is the main writer of the posttranslational modification, ADP-ribosylation in response to DNA damage (4). PARP1 has a crucial role in the DNA damage response as it is recruited rapidly to the DNA lesions modifying itself and nearby targets by adding ADP-ribose moieties on specific protein residues. The poly (ADP-ribose) (PAR) chains generated by PARP1 trigger the recruitment of chromatin remodelers and DNA repair factors involved in early steps of the DNA damage response (5,6).

PARPi not only inhibit ADP-ribosylation signaling but also increase PARP1 retention on sites of DNA damage causing a so-called 'PARP trapping' phenomenon, which primarily underlies PARPi sensitivity (7). These PARP-bound DNA lesions are thought to be converted into DSBs during replication (8), leading to genomic instability and increased cell death in the case of HR deficiencies observed in cells displaying BRCA1/2 deficiency or a BRCAness phenotype (9). It is this Achilles' heel that is exploited in the treatment of BRCA-deficient tumors with PARPi.

Since the approval of PARPi in the clinic, extensive work has been done to expand their therapeutic spectrum beyond the BRCAness phenotype. For example, synthetic lethality with PARPi has been reported upon loss of Histone PARylation Factor 1 (HPF1) (10), defects in the ribonucleotide excision repair pathway (11), impairments of resolving trapped PARP1 (12–15) and loss of factors of the Fanconi anemia pathway (16). More recently, PARPi sensitivity has been linked to the induction of single-stranded DNA (ssDNA) gaps either from unprocessed Okazaki fragments or unrestrained fork progression ultimately causing the cells to experience replication stress (17–19).

Unbiased knockout screens to identify genes underlying PARPi resistance suggested the loss of POLE3 and POLE4 to be synthetic lethal with PARPi (12,20,21). POLE3 and POLE4 are subunits of DNA polymerase epsilon (POLε). POLε is a protein complex mainly responsible for replicating the DNA leading strand during S phase (22). It consists of four subunits, the catalytic core composed of POLE1 along with POLE2 and the aforementioned accessory factors POLE3 and POLE4. Pol2 and Dpb2, the yeast orthologues of POLE1 and POLE2, respectively, are essential for viability but not Dpb3 (POLE4 in mammals) or Dpb4 (POLE3 in mammals) (23). Deletion of Dpb3 and Dpb4 does not stall replication but instead, reduces the processivity of the Pol2-Dpb2 subcomplex due to unstable binding to DNA leading to its frequent dissociation from the template which leaves gaps on the leading strand (24). This role in stabilizing the POLε complex becomes critical upon replication stress as shown by increased sensitivity to hydroxyurea (HU) upon loss of Dpb4 (25). In addition, while Dpb3 is important for normal cell-cycle progression (26), Dpb4 was reported to promote activation of the checkpoint kinase Mec1 (ATR in humans) upon replication stress (25). Importantly, similar sensitivity can be observed in mice fibroblasts lacking POLE4 (27).

Both POLE3 and POLE4 have histone-fold domains and form a H2A–H2B-like heterodimer (28) which displays H3–H4 histone chaperone activity *in vitro* (29). More specifically, mice and yeast orthologs of POLE3 and POLE4 were shown to facilitate parental H3–H4 histone deposition on the leading strand keeping symmetrical segregation of histones between the two DNA strands (30,31). Consistent with their role in chromatin assembly, these accessory subunits were also shown to regulate heterochromatin silencing in budding and fission yeasts (32,33). Interestingly, the yeast ortholog of POLE3 (Dpb4) plays a dual role in this process depending on the complex it is part of (Figure 1A). On the one hand, as part of the POLε complex, the Dpb4-Dpb3 subcomplex ensures heterochromatin inheritance. On the other hand, within the yeast ortholog of the chromatin remodeling and chromatin-accessibility complex (CHRAC), the subcomplex Dpb4-Dls1 (CHRAC15 in humans) is important for the inheritance of an expressed state (32). As part of the CHRAC complex, Dpb4 also promotes histone removal at the vicinity of DSBs to facilitate DNA end resection (34), while through its interaction with Dpb3 in the POLε complex, it regulates the activation of the yeast checkpoint kinase Rad53 (CHK2 in humans), which is the effector kinase of Mec1/ATR in yeast (34,35).

PARP activity has been implicated in most of the POLε associated functions including DNA repair, replication, and chromatin regulation. In the present work, we provide insight into the mechanisms underlying the synthetic lethality observed upon loss of POLE4 and PARP inhibition.

Materials and methods

Cell lines and cell culture

Cell lines used in this study were cultured in DMEM (Biosera) supplemented with 10% FBS, 100 μg/ml penicillin, 100 U/ml streptomycin and 1% NEAA and maintained at 37°C in a 5% CO_2 incubator unless otherwise stated. RPE-1 p53 KO and RPE-1 p53/BRCA1 double KO cells were kindly gifted from Alan D. D'Andrea lab (36) and were grown using DMEM-F12 (Biosera) supplemented with 10% FBS, 100 μg/ml penicillin, 100 U/ml streptomycin.

POLE3 KO and POLE4 KO cell lines were generated in this study from either wild-type HeLa cells or wild-type U2OS-FlpIn cells (kindly provided by Ivan Ahel's lab) using CRISPR/Cas9 technology. The HeLa cell line was authenticated by STR profiling (Eurofins Genomics) and had 100% match with HeLa (amelogenin + 12 loci) using the Cellosaurus cell line database (37).

The sgRNA sequences targeting either POLE3 or POLE4 are:

sgPOLE3: 5′-GTACAGCACGAAGACGCTGG-3′
sgPOLE4: 5′-GTCGGGATCTGCCTTCACCA-3′

RNA interference and plasmid transfection

pSpCas9 (BB)-2A-Puro (PX459) V2.0 used to generate the knockouts of this study was a gift from Feng Zhang lab (Addgene, plasmid #62988) (38). Plasmid transfections were performed using Xfect (Takara) according to the manufacturer's protocol.

RNA interference experiments with siRNA (sequences in Supplementary Table S1) were conducted using Dharmafect (Dharmacon) or RNAiMAX (Lipofectamine) transfection reagents according to the manufacturers' instructions. Downregulation was verified by western blotting using specific antibodies (detailed in Supplementary Table S2).

For rescue experiments the HeLa POLE4 KO cells were transfected with pmEGFP-C1 and either pcDNA5-FRT-TO or

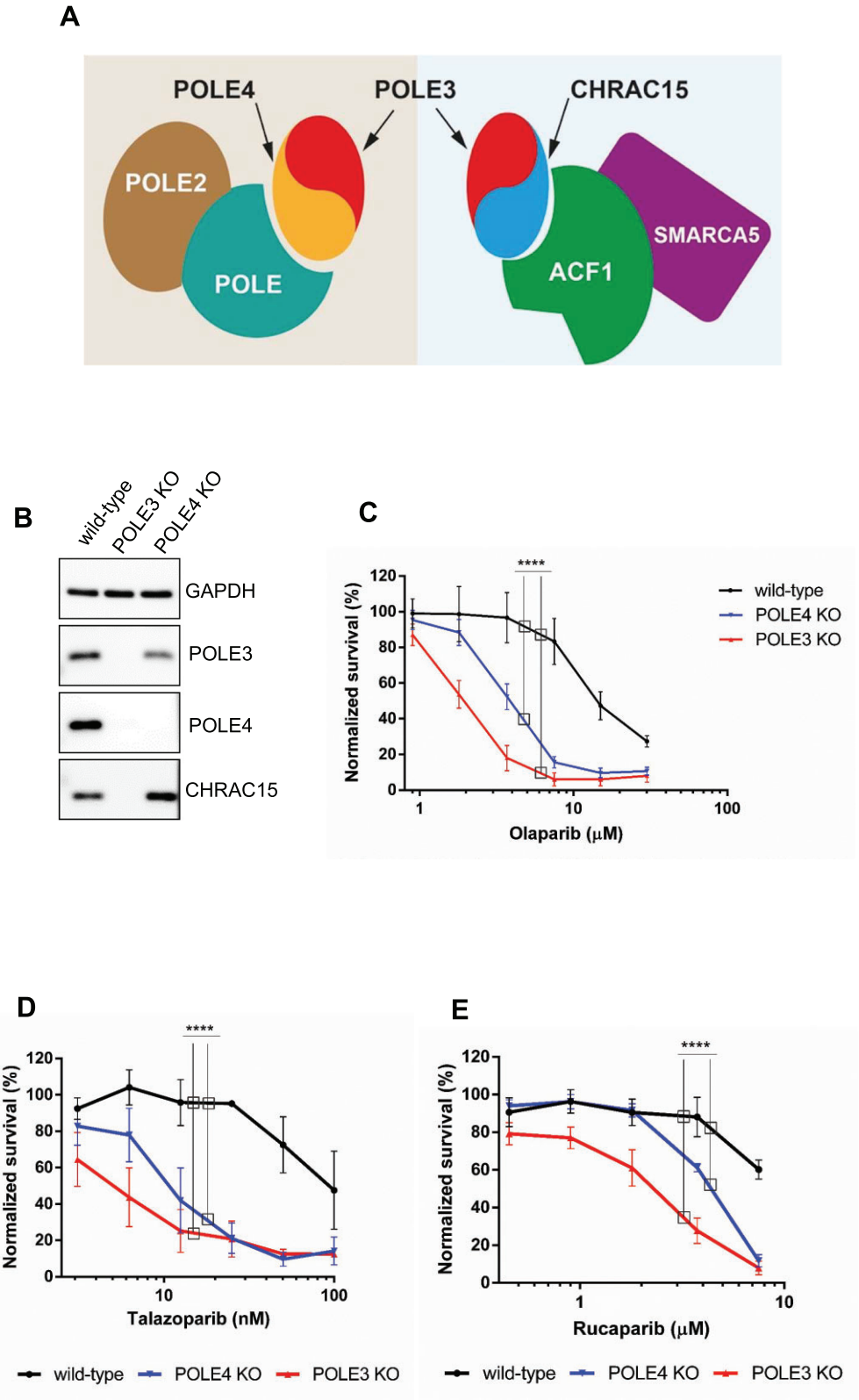

Figure 1. Loss of POLE3 or POLE4 induces PARPi sensitivity. (**A**) Schematic representation of the accessory subunits POLE3 and POLE4 within POLε and CHRAC complexes. (**B**) Western blot showing the levels of POLE3, POLE4 and CHRAC15 in HeLa wild-type, POLE4 KO and POLE3 KO cells. GAPDH is used as a loading control. (**C–E**) Cell survival assays demonstrating sensitivity of POLE3 KO and POLE4 KO to different PARPi compared to their parental HeLa wild-type. The curves are normalized to the untreated condition corresponding to each genotype. PARPi treatment was refreshed once during the 7-day long experiment. The graphs are derived from three independent experiments. Mean ± SEM ($n = 3$). Asterisks indicate *P*-values obtained by two-way ANOVA (**** $P < 0.0001$).

pcDNA5-FRT-TO-POLE4 using TransIT®-LT1 Transfection Reagent (Mirus) 24–48 h prior treatment. POLE4 expression was verified by Western blotting.

PARP1 recruitment to sites of laser irradiation

HeLa wild-type or HeLa POLE4 KO cells were grown in 8-well Lab-Tek II chambered cover glass 30 (Thermo Scientific) and transfected 48 h prior to imaging with GFP-tagged PARP1 chromobody (Chromotek). For sensitization, growth medium was replaced with fresh medium containing 0.15 μg/ml Hoechst 33342 for 1 h at 37°C. Prior to imaging, the sensitizing medium was then replaced with CO_2-independent imaging medium (Phenol Red-free Leibovitz's L-15 medium (Life Technologies) supplemented with 20% fetal bovine serum, 2 mM glutamine, 100 μg/ml penicillin and 100 U/ml streptomycin). For PARP inhibition conditions, cells were treated with Olaparib (30 nM) for 30 min prior to imaging.

Live-cell imaging experiments were performed on a Ti-E inverted microscope from Nikon equipped with a CSU-X1 spinning-disk head from Yokogawa, a Plan APO 60×/1.4 N.A. oil-immersion objective lens and a sCMOS ORCA Flash 4.0 camera. Laser microirradiation at 405 nm was done along a 16 μm-line through the nucleus using a single-point scanning head (iLas2 from Roper Scientific) coupled to the epifluorescence backboard of the microscope. The laser power at 405 nm was measured prior to each experiment to ensure consistency across the experiments and set to 125 μW at the sample level. Cells were kept at 37°C with a heating chamber. Protein recruitment was quantified using a custom-made Matlab (MathWorks) routine.

Immunofluorescence

For native BrdU staining, cells were grown with 20 μM BrdU-containing medium for 48 h, the medium was then replaced with 10 μM Olaparib-containing medium for 24 h. Cells were washed with PBS, pre-extracted with 0.5% Triton X-100 in PBS for 5 min at 4°C then fixed with 4% paraformaldehyde (PFA) for 15 min at 4°C. Permeabilization was done using 0.5% Triton X-100 in PBS for 10 min followed by blocking with 5% FBS in 0.1% Triton X-100 for 45 min at room temperature, then incubated with primary antibody diluted in blocking solution overnight at 4°C.

For Rad51 experiments, cells were treated with 10 μM Olaparib-containing medium for the 48 h before being washed with PBS and pre-extracted with pre-extraction buffer (10 mM Tris–HCl, 2.5 mM $MgCl_2$, 0.5% NP-40, 100× Protease inhibitor cocktail (Roche)) for 5 min at 4°C. Fixation was done using 4% PFA for 15 min at 4°C followed by permeabilization, blocking and antibody incubation as described earlier.

For S-phase PAR staining experiments, either wild-type or POLE4 KO cells were loaded with 2.5 μM of amine-reactive dye carboxyfluorescein diacetate, succinimidyl ester (CFSE) using the CellTrace™ CFSE Cell Proliferation Kit (Molecular Probes, Life Technologies) for 12 min at room temperature before seeding and mixing with the other unlabeled genotype. Cells were treated with DMSO (vehicle control) or PARGi (10 μM) or PARGi (10 μM) and Fen1i (10 μM) (Supplementary Table S3) for 1 h. Cells were pulse-labeled with the nucleotide analog EdU (10 μM) (5-ethynyl-2′-deoxyuridine, Baseclick, BCK-EdU555) for the last 20 min prior to fixing. Fixation and staining were done as described earlier.

Following overnight incubation with the primary antibodies (Supplementary Table S2), cells were washed three times with 0.1% Triton X-100 and incubated at room temperature with fluorescently tagged secondary antibody (Supplementary Table S2) for 1 h. Next, cells were washed with 0.1% Triton X-100 and counterstained with DAPI (1 μg/ml in PBS) for 10 min. To detect proliferating cells, EdU incorporation was visualized by a Click-IT Kit (Baseclick) according to the manufacturer's protocol.

Z-stacks of images were acquired on a Zeiss LSM800 confocal microscope with a Plan-Apochromat 20x/0.8 M27 or a water immersion Plan-Apochromat 40×/1.2 DIC M27 objective controlled by the ZEN 2.3 software. Fluorescence excitation was performed using diode lasers at 405, 488, 561 and 650 nm. Images were analyzed after generating maximum intensity projections of the z-stacks using a custom CellProfiler pipeline (39).

BrdU comet post-replication repair assay

Exponentially growing cells were plated in 24-well plate at a density of 3×10^5 cells/well. The following day the cells were pulse-labeled with 25 μM of the nucleotide analog BrdU, and incubated at 37°C for 30 min. Next, the cells were washed with PBS and treated or not with hydroxyurea (4 mM) for 3 h. Cells were then harvested (corresponding to 0 h repair) or left to perform post-replicative repair for additional 3 h. Cells were embedded in 0.75% low melting agarose and layered onto microscope slides (pre-coated with 1% agarose), covered with coverslips, and left to solidify for 5 min at 4°C.

The following steps were performed as detailed in (40) with slight modification detailed below. The alkaline lysis was performed in 0.3 M NaOH, 1 mM EDTA, pH 13 for 2 h in Coplin jars. The DNA was left to unwind for 40 min in this ice-cooled electrophoresis buffer. The electrophoresis was subsequently conducted at 1 V/cm (25 V, 300 mA) for 30 min in the same buffer at 10°C.

Following the electrophoresis, the slides were washed with neutralization buffer (0.4 M Tris–HCl, pH 7.4), blocked with PBS containing 1% BSA for 20 min at room temperature and incubated with the indicated primary antibody (Supplementary Table S2) for 2 h at room temperature. The primary antibody was washed off and slides were incubated with secondary antibody (Supplementary Table S2) for 2 h at room temperature then mounted by Fluoromount mounting solution containing DAPI, covered with coverslips and stored at 4°C until microscopy. Imaging was performed using Zeiss Axioscope Z2 fluorescent microscope. Scanning of images was done using automated scanning platform of Metasystem and the quantitation of comets was done by Metasystems Neon Metafer4 software. Three independent experiments were done with duplicate slides, 150–300 comet/slides were scored.

BrdU comet assay for detection of ssDNA gaps

To detect the Olaparib-induced ssDNA gaps the comet method described above was applied with a slight modification. Exponentially growing cells were plated in 24-well plate at a density of 3×10^5 cells/well in duplicates. The following day the growth medium was changed to fresh DMEM containing 25 μM of the nucleotide analog iododeoxyuridine (IdU), the cells were incubated at 37°C for 30 min. After the

labelling, the cells were washed two times with PBS and were cultured in Olaparib (20 μM) containing medium for 24 h.

Cells were harvested by trypsinization, collected and pelleted in DMEM washed with ice-cold PBS. Pelleted again and resuspended in 500 μl ice cold H_2O_2 (75 μM, diluted in PBS), kept on ice for 3 minutes and pelleted by centrifugation (5 min, 900 rpm at 4°C). H_2O_2 was removed by washing twice with ice-cold PBS and, after the last centrifugation, cells were resuspended in 70 μl 0.75% low melting agarose/slide. The lysis and the further steps of the assay and analysis were identical to those detailed in the section of BrdU comet post-replication repair assay.

DNA fiber assay

Exponentially growing cells were pulse labelled with 25 μM IdU for 20 min in 37C°, washed twice with prewarmed PBS and then labeled with 250 μM CldU (chlorodeoxyuridine) in the presence or absence of Olaparib (10 μM), cells were harvested, and DNA fiber spreads were prepared as described previously (41). Briefly, 2 μl of cells resuspended in PBS (10^6 cells/ml) were spotted onto clean glass slides. Cells were lysed with lysis solution (0.5% sodium dodecyl sulphate (SDS) in 200 mM Tris–HCl (pH 7.5), 50 mM EDTA). Slides were tilted at 15° to the horizontal, allowing a stream of DNA to run slowly down the slide. Next, slides were air-dried for 20 minutes and fixed in methanol-acetic acid (3:1) and let dry for 10 min. Fixed fibers were rehydrated in water for 5 min and denatured (2.5 M HCl for 1 h) and blocked in blocking buffer (1% bovine serum albumin and 0.1% Tween20) for 1 h. Incubation with the two primary antibodies (Supplementary Table S2) was done for 2 h in humidified chamber at room temperature. Slides were washed and incubated with the secondary antibodies (Supplementary Table S2) for 90 min in humidified chamber at room temperature. DNA fibers were imaged using Axioscope Z2 fluorescent microscope (Zeiss, Germany) with a 60× objective. The lengths of DNA tracks corresponding to IdU and CldU labelling were measured using the Zen (Zeiss) software. In each experiment, a minimum of 200 independent fibers were analyzed per experiment. All measurements of four independent experiments were summarized in a dot plot created in GraphPad10.2.

R-loop detection

Cells were treated with 10 μM Olaparib and 2 mM hydroxyurea for 24 h before being washed with PBS and fixed with MeOH for 15 min at −20°C. Cells were then treated or not with 2.5 units of RNase H (Thermo Fisher Scientific, cat #EN0201). Blocking was done with 3% BSA in 0.1% Triton-X100 for 45 min at room temperature, then cells were incubated with anti-DNA–RNA Hybrid primary antibody (Supplementary Table S2) diluted in blocking solution for overnight at 4°C. Next day, cells were washed three times with PBS and incubated at room temperature with anti-mouse IgG-Alexa Fluor 555 secondary antibody (Supplementary Table S2) for 1 h. Then the cells were washed with PBS and stained with DAPI (1 μg/ml in PBS) for 10 min. Z-stacks of images were acquired on a VisiScope Spinning Disk confocal microscope with 40×/0.6 objective using diode lasers at 405 and 561 nm. Detection was performed with Andor Zyla 4.2 PLUS camera. Fluorescent images were analyzed after generating maximum intensity projections of the z-stacks using CellProfiler (39).

Cell survival assays

POLE4 KO, POLE3 KO and their parental wild-type cells were seeded in defined numbers in 96-well plates and treated for one week with Olaparib (0, 0.45, 0.9, 1.8, 3.7, 7.5, 15, 30 μM), Rucaparib (0, 0.45, 0.9, 1.8, 3.7, 7.5, 15 μM), Talazoparib (0, 15, 31, 62, 125, 250 nM) or ATRi (0, 0.6, 1.2, 2.5, 5, 10 μM) (Supplementary Table S3). For experiments with the combination of ATRi and Olaparib, 1 μM Olaparib was used along with 0.6 μM of ATRi. For experiments with RNAi-induced BRCA1 depletion the concentrations of Olaparib were 0, 0.3, 0.6, 1.2, 2.5, 5 and 10 μM. Treatment with HU (Sigma-Aldrich, 0, 0.5, 1, 2, 4, 8 mM) was for 24 h, with MMS (Sigma-Aldrich, 0, 0.0015, 0.003, 0.006, 0.012, 0.025, 0.05%) or with Etoposide (Sigma-Aldrich, 0, 0.45, 0.9, 1.8, 3.7, 7.5, 15 μM) for 1 h; following the indicated durations, cells were washed and incubated for 1 week in complete medium. After 7 days of incubation, the supernatants were aspirated and resazurin (Sigma) solution was added (25 μg/ml in Leibowitz's L-15, Gibco). The fluorescent resorufin product was measured after 30–60 min using a Biotek Synergy H1 microplate reader with a 530/590 filter set.

Flow cytometry for intracellular markers and cell cycle analysis

Cells were dissociated with TrypLe Select (Gibco), washed with PBS and fixed with ice-cold ethanol. For labelling the intracellular markers, the cells were permeabilized and blocked with 0.5% Triton X-100 and 5% FBS in PBS, and then incubated with the appropriate primary antibody (Supplementary Table S2) overnight at 4°C. Next, the cells were washed two times with PBS, and incubated with fluorescently tagged secondary antibodies (Supplementary Table S2) for 2 h at room temperature. Finally, the DNA staining solution was added (10 μg/ml propidium-iodide and 10 μg/ml RNase in PBS) for 15 min at room temperature. The samples were analyzed with CytoFLEX S flow cytometer (Beckman Coulter Life Sciences) or FACSCalibur (Becton Dickinson). The measurements were evaluated with Kaluza Analysis software (Beckman Coulter Life Sciences).

PARylation assay

Cells were cultured in 6 cm dishes. The cells were treated with H_2O_2 (2 mM) in fresh culturing medium for the indicated timepoints. At the time of collection, the cells were washed twice in PBS and lysed directly using denaturing lysis buffer (4% SDS, 50 mM Tris–HCl, pH 7.4, 100 mM NaCl, 4 mM $MgCl_2$, 5 U/μl Benzonase). The cell lysates were collected using a cell scraper and the total protein concentration was equalized after measuring the initial concentration by NanoDrop (A280 setting). Samples were boiled in 4× Laemmli buffer for 5 min at 95°C prior to western blotting.

Western blotting

Protein samples were prepared for SDS–polyacrylamide gel electrophoresis in 4× sample buffer (10% SDS, 300 mM Tris–HCl, 10 mM β-mercaptoethanol, 50% glycine, and 0.02% bromophenol blue). Separated proteins were blotted onto nitrocellulose or PVDF membranes, blocked for 1 h at RT in 5% low-fat milk or 5% BSA in 0.1% Tris-buffered saline, and incubated with primary antibodies overnight at 4°C. Horseradish peroxidase-conjugated secondary anti-

bodies were used for 1 hour at room temperature. Membranes were developed with enhanced chemiluminescence using Odyssey Fc Imaging System (LI-COR Biotechnology).

Statistical analysis

All experiments were done at least in triplicates and for immunofluorescence experiments at least 200 cells were scored. A minimum of 10 cells were irradiated in live-cell imaging experiments. Graphing and statistical analysis were done using GraphPad Prism versions 6 and 7. Statistical analysis of cell survival experiments was done using two-way ANOVA. PARP1 recruitment experiments were analyzed using Mann–Whitney unpaired *t*-test. Statistics for immunofluorescence experiments were performed using one-way ANOVA. Asterisks represent *P* values, which correspond to the significance ($*P < 0.05$, $**P < 0.01$, $***P < 0.001$ and $****P < 0.0001$).

Results

Loss of POLE3 or POLE4 causes PARPi sensitivity.

We and others have previously identified the loss of POLE3 and POLE4 to sensitize cells to the PARP1/2 inhibitor Olaparib (12,20,21). To confirm this finding, we employed CRISPR-Cas9 gene editing to generate POLE3 and POLE4 knock-outs (KO) in HeLa cells (Figure 1B, Supplementary Figure S1A). As expected, all tested clones of POLE3 KO and POLE4 KO were hypersensitive to Olaparib treatment in a cell survival assay (Figure 1C, Supplementary Figure S1B, C), a phenotype that was also observed upon knockdown of these subunits although to a lower extent (Supplementary Figure S1D). Furthermore, POLE3 and POLE4 KOs were also sensitive to other PARPi, such as Talazoparib and Rucaparib, showing that the sensitivity was not limited to Olaparib (Figure 1D, E). Additionally, the PARPi sensitivity upon POLE3 and POLE4 loss was not exclusive to HeLa cells as U2OS cells knocked out for POLE3 or POLE4 showed similar sensitive phenotype to Olaparib (Supplementary Figure S1E, F).

The heterodimerization of POLE3 and POLE4 is essential for their stability (21). Accordingly, the loss of either protein eliminated, or strongly reduced the levels of, the other (Figure 1A, B, Supplementary Figure S1A). POLE3 is a shared subunit between the POLε holoenzyme and the CHRAC complex (42), where POLE3 is forming heterodimer with POLE4 and CHRAC15, respectively (Figure 1A). Similar to the POLE3–POLE4 dimer, compromising the POLE3–CHRAC15 dimer by deleting POLE3 led to loss of CHRAC15 protein (Figure 1B). Since POLE3 KO cells lack both POLE4 and CHRAC15, we decided to further characterize the consequences of PARPi treatment only in the POLE4 KO to avoid confounding phenotypes arising from the lack of both POLE3–POLE4 and POLE3–CHRAC15 heterodimers.

PARP1 is essential for Olaparib-induced POLE4 KO sensitivity with no apparent defects in the DNA damage response.

The toxicity of PARPi requires the presence of PARP1 in cells (7), with recent reports also highlighting a requirement of PARP2 (43,44). To investigate whether the sensitivity of POLE4 KO to PARPi was dependent on the presence of PARP1 or PARP2, we employed RNAi to deplete either or both factors. Cell survival assays demonstrated that the depletion of PARP1 alone was sufficient to rescue POLE4 KO sensitivity (Figure 2A, Supplementary Figure S2A). Instead, depleting PARP2 neither reduced the PARPi sensitivity nor further improved survival of the POLE4 KO co-depleted for PARP1, suggesting that the Olaparib-induced sensitivity of POLE4 KO relies on the presence of PARP1, but not PARP2, which is consistent with PARP1 trapping on their cognate lesions (Figure 2A, Supplementary Figure S2A).

Active ADP-ribosylation is crucial to release PARP1 from DNA. Cellular processes dampening or enhancing this signaling pathway lead to increased or reduced sensitivity to PARPi, respectively (45,46). Nevertheless, immunoblots showed no major difference in ADP-ribose (ADPr) levels between wild-type and POLE4 KO, as detected by a pan-ADPr reagent, both in the absence of genotoxic stress and after H_2O_2 treatment (Supplementary Figure S2B). This data indicates that POLE4 loss is not a source of DNA lesions that would lead to PARP1 activation. Moreover, it excludes POLE4 as playing a central role in the regulation of ADP-ribosylation signaling that could underlie the sensitivity of the KO cells to PARPi. Nevertheless, processes independent of ADP-ribosylation could also modulate PARP1 retention at DNA lesions (47,48). Thus, to more directly assess whether POLE4 regulates PARP1 mobilization from sites of DNA damage, we monitored the dynamics of endogenous PARP1 at sites of DNA damage upon laser micro-irradiation using a GFP-tagged PARP1-binding chromobody (49). In wild-type cells, PARP1 was recruited rapidly to sites of laser-induced damage before dissociating from the lesions within a time frame of a few hundreds of seconds (Figure 2B, Supplementary Figure S2C). As expected, this release was delayed upon Olaparib treatment (Figure 2B, Supplementary Figure S2C). PARP1 kinetics at sites of laser irradiation were similar in POLE4 KO and wild-type cells, irrespective of the presence of PARPi (Figure 2B, Supplementary Figure S2C) suggesting that POLE4 did not regulate PARP1 dynamics at sites of DNA damage.

To further investigate a potential role of POLE4 in DNA repair, we assessed the sensitivity of the POLE4 KO cells to genotoxic stress. POLE4 KO were not sensitive to methyl methanesulfonate (MMS) or etoposide treatments (Figure 2C, D). This is in line with earlier reports that observed no sensitivity to camptothecin (CPT) or MMS in a Dpb3-deficient yeast strain (50), or to ionizing radiation in POLE4-deficient mouse fibroblasts (27).

Altogether these data indicate that PARPi sensitivity of POLE4 KO is not a consequence of impaired PARP1 mobilization from sites of damage or defects in the DNA damage response.

POLE4 loss alters the replication profile and increases the level of PARPi-induced ssDNA gaps

PARPi have been reported to accelerate fork speed (51). Additionally, the accessory subunits of POLε were shown to be important for processive progression of the POLε complex on the DNA (24). To investigate the replication speed in POLE4 KO and how PARPi affects it, we employed DNA fiber assay, where cells were pulse labeled with the nucleotide analog IdU for 20 min followed by pulse labeling with another nucleotide analog, CldU for the same period of time with or without PARPi treatment (Figure 3A). As previously reported (51), PARPi treatment increased the fork speed in wild-type cells (Figure 3A) as shown by increased CldU/IdU ratios compared to untreated cells. Replication was slightly but

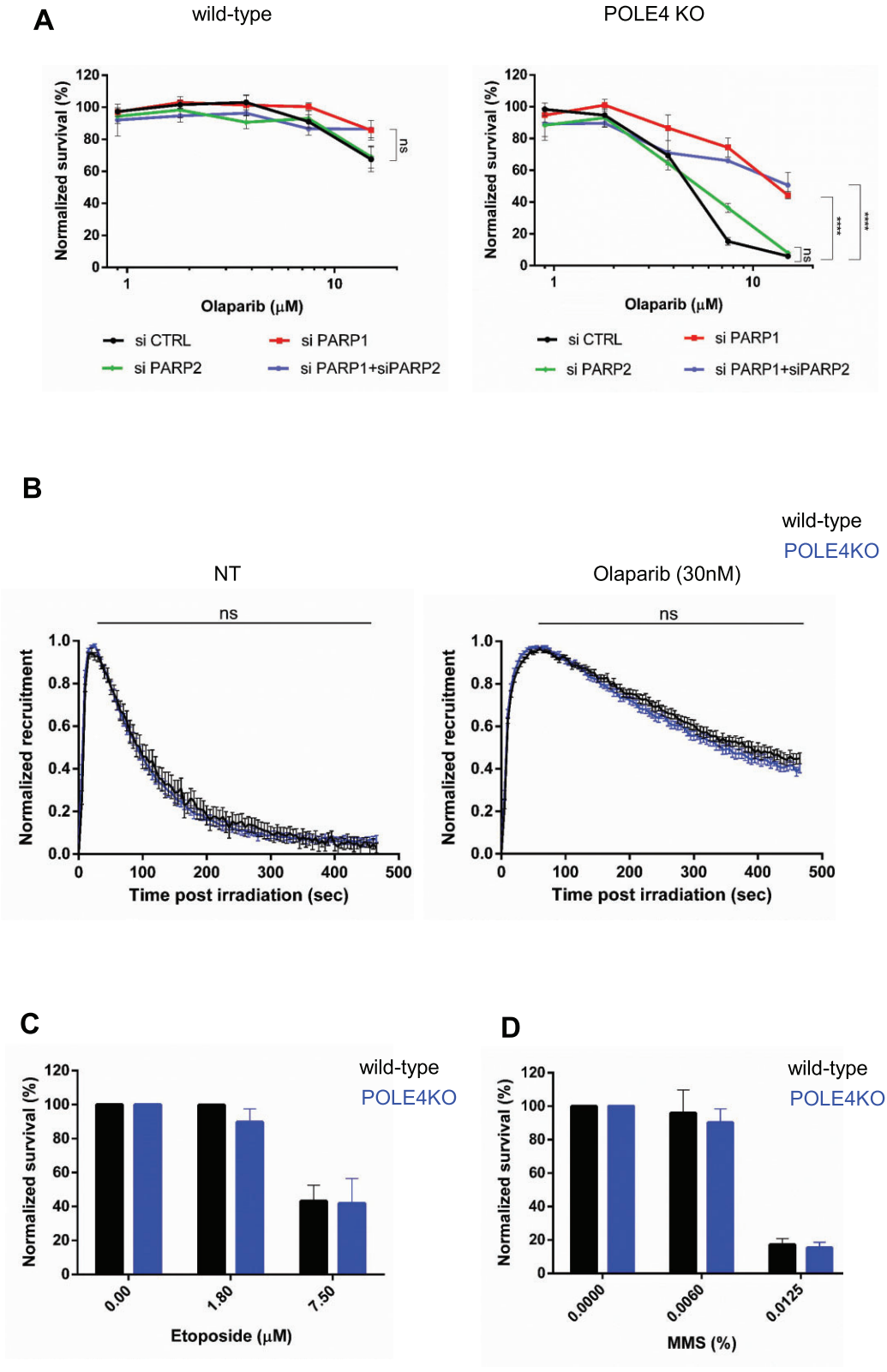

Figure 2. PARP1 is essential for Olaparib-induced POLE4 KO sensitivity with no apparent defects in the DNA damage response. (**A**) Cells survival assay showing Olaparib sensitivity of HeLa wild-type and POLE4 KO upon downregulation of PARP1, PARP2 or both of them using siRNA transfection. The curves are normalized to the untreated condition corresponding to each genotype. PARPi treatment was refreshed once during the 7-day long experiment. The graphs are derived from three independent experiments. Mean ± SEM ($n = 3$). Asterisks indicate *p*-values obtained by two-way ANOVA (ns. Not significant and **** $P < 0.0001$). (**B**) Normalized recruitment quantification of GFP-tagged PARP1 chromobody to sites of DNA damage in HeLa wild type and POLE4 KO cells in both untreated (left) or Olaparib treated (right) conditions. All data points included ± SEM. The figure is a representative experiment of three independent replicates ($n = 3$). Measurements were analyzed using Mann–Whitney unpaired *t*-test. (ns. Not significant). (C, D) Cell survival of HeLa wild-type and POLE4 KO cells upon treatment with etoposide (**C**) or MMS (**D**) for 1h. After the 1h treatment, cells were washed and incubated in culturing medium for 7 days. The bars are normalized to the untreated condition corresponding to each genotype. The graphs are derived from three independent experiments. Mean ± SEM ($n = 3$).

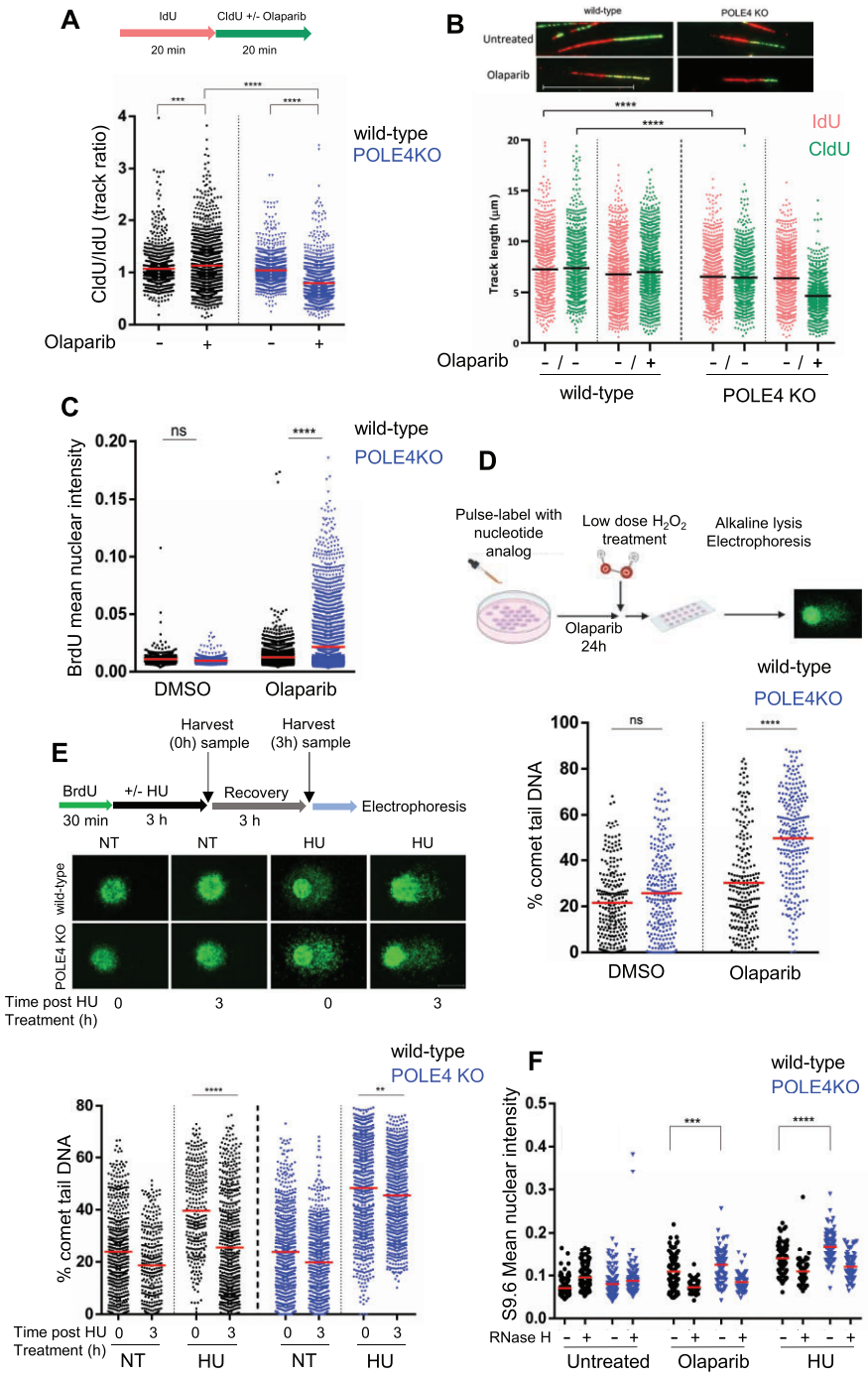

Figure 3. POLE4 loss alters the replication profile and increases PARPi-induced ssDNA gaps. (**A**, **B**) DNA fiber assay of HeLa wild-type and POLE4 KO cells upon treatment with Olaparib (20 μM). (A, top) Schematic illustration of the experimental procedure. (A, bottom) Results are illustrated as ratio of CldU and IdU labelled fiber track lengths obtained from four independent experiments ($n = 4$). (**B**, top) Representative images of fibers taken from HeLa wild-type and POLE4 KO cells with the indicated treatment. Scale bar, 20 μm. (**B**, bottom) Data represent length of the indicated tracks derived from four independent experiments ($n = 4$). Asterisks indicate *P*-values obtained by one-way ANOVA (*** $P < 0.001$, **** $P < 0.0001$). (**C**) Immunofluorescence experiment of native BrdU staining. Cells with the indicated genotypes were incubated with BrdU (20 μM, 48 h), then treated with Olaparib (10 μM, 24 h) or the control vehicle DMSO. Mean BrdU intensity of all scored cells was blotted. The graph represents one experiment out of three independent repetitions. Asterisks indicate *P*-values obtained by one-way ANOVA (ns, not significant, **** $P < 0.0001$). (**D**, top) Schematic illustration of BrdU-Comet experiment. (Bottom) Quantification of % of comet tail DNA of HeLa wild-type and POLE4 KO cells treated with Olaparib (20 μM, 24 h) or DMSO. The figure is a representative of three independent experiments. Asterisks indicate *P*-values obtained by one-way ANOVA (ns, not significant, **** $P < 0.0001$). (**E**, top) Schematic illustration of the post-replicative comet assay. Cells were BrdU pulse labelled, mock treated or treated with hydroxyurea (HU) (4 mM for 3 h) and harvested immediately (0 h) or left to recover for additional 3 h. Comet PRR assay and immunostaining was performed as detailed in Materials and methods. (Middle) Representative images of post-replication repair comet assay. Scale bar, 20 μm. (Bottom) Quantification of % of comet tail DNA. The figure is a representative of three independent experiments. Asterisks indicate *P*-values obtained by one-way ANOVA (** $P < 0.01$, **** $P < 0.0001$). (**F**) Detection of R-loops in untreated, Olaparib (10 μM) or hydroxyurea-treated (HU, 2 mM) wild-type or POLE4 KO HeLa cells after 24 h treatment. The graph shows the mean fluorescent intensity of nuclei with or without RNase H treatment. The figure is a representative of three independent experiments. Asterisks indicate *P*-values obtained by one-way ANOVA (*** $P < 0.001$, **** $P < 0.0001$).

significantly slower in POLE4 KO as compared to wild-type even without PARPi treatment (Figure 3B), indicated by the reduction in track lengths compared to wild-type cells, which can be attributed to impaired POLε progression as a consequence of POLE4 absence. Importantly, replication speed was further reduced in the presence of PARPi (Figure 3A, B), suggesting major defects in replication upon PARP inhibition.

Sensitivity to PARPi has been linked to defects in Okazaki fragments processing during DNA replication (17), and PAR signal was reported to correlate with the amount of unligated Okazaki fragments (52). To test whether POLE4 had a role in Okazaki fragments processing, we assessed PAR levels in replicating cells in the presence of Poly (ADP-ribosyl) glycohydrolase inhibitor (PARGi), which is required to detect the highly dynamic PAR signal at replication foci (52). To ensure each cell line undergoes the exact same conditions when performing the experiment and imaging, we loaded POLE4 KO cells with the amine-reactive carboxyfluorescein diacetate, succinimidyl ester (CFSE) cell tracker dye and mixed it with its wild-type unlabeled cells. The lack of difference in PAR levels between POLE4 KO and wild-type cells suggested similar amounts of Okazaki fragments in both cell lines (Supplementary Figure S3A). Co-inhibition of PARG and Fen1, an enzyme responsible for processing Okazaki fragments (52), increased further the PAR signal compared to PARG inhibition alone but again to comparable levels in both wild-type and POLE4 KO (Supplementary Figure S3A), indicating that POLE4 loss neither altered the processing of Okazaki fragments nor led to increased S-phase specific PARP activity.

PARPi were reported to induce ssDNA gaps behind replication forks through the suppression of fork reversal (18). To test whether such gaps were formed upon Olaparib treatment in cells lacking POLE4, we employed the non-denaturing BrdU immunostaining assay, where the specific antibody against BrdU is unable to bind the nucleotide analog in native conditions unless there is a single stranded DNA gap opposite it, therefore making the intensity of BrdU staining an indicator of the ssDNA gaps levels in the cell (17,18). With this assay, POLE4 KO cells displayed a striking increase in the intensity of BrdU staining upon Olaparib treatment compared to their wild-type counterparts, indicating a dramatic accumulation of unprocessed ssDNA gaps in these cells (Figure 3C, Supplementary Figure S3B). To further confirm this observation, we performed a variation of a comet assay, the so called BrdU comet assay, where pulse labeling cells with a nucleotide analog is used to highlight newly synthesized DNA, rendering the assay S-phase specific (40,53). The assay was further modified by application of a short, low dose of H_2O_2 treatment immediately prior to embedding the cells in agarose, to convert single stranded gaps into double stranded breaks, the resulting fragmented DNA fraction thus migrating into the comet tail (53). Consistent with the non-denaturing BrdU staining results (Figure 3C, Supplementary Figure S3B), we observed a significant increase in the percentage of comet tail DNA of POLE4 KO cells treated with Olaparib, revealing increased formation of ssDNA gaps (Figure 3D, Supplementary Figure S3C), indicating the role of POLE4 in averting the formation of PARPi-induced ssDNA gaps.

The accumulation of ssDNA gaps could also reflect impaired post-replicative repair (PRR). To test whether POLE4 plays a role in this process, we performed a comet assay variant described previously as a sensitive indicator of PRR efficiency (40). Briefly, cells were pulse-labeled with BrdU and subjected to Hydroxyurea (HU) treatment to induce S-phase specific ssDNA breaks, then the treatment was washed out and cells were incubated for a period of time to allow the repair of replicative gaps. In wild-type cells, HU treatment led to a higher level of post-replicative gaps as compared to their untreated counterparts, indicated by an increase of percentage of DNA in the comet tails, that was reduced after the 3h recovery time (Figure 3E). On the contrary, POLE4 KO cells showed increased levels of post-replicative gaps upon HU treatment, even after 3h recovery as compared to wild-type cells (Figure 3E), underscoring the role of POLE4 in maintaining efficient PRR. Accordingly, POLE4 KO were hypersensitive to replication stress induced by HU treatment in cell survival assays (Supplementary Figure S3D), in line with previous reports (21,54,55). It has been reported that HU treatment leads to the accumulation of R-loops (56), DNA:RNA hybrids that form due to nascent RNA binding to its complementary DNA, reflecting a possible replication-transcription conflict (57). Moreover, PARP1 was shown to be important for R-loops resolution (58–60). Given POLE4 KO sensitivity to both PARPi and HU, we probed for the levels of R-loops in these cells using the S9.6 antibody that recognizes DNA:RNA hybrids (61). Loss of POLE4 caused increased accumulation of R-loop structures compared to wild-type cells upon treatment with either HU or PARPi (Figure 3F, Supplementary Figure S3E) indicating a role of POLE4 in resolving these structures. The pan nuclear intensity observed with this antibody decreased upon treatment with RNase H, emphasizing its specificity for the R-loops (Figure 3F, Supplementary Figure S3E).

Taken together, these results demonstrate that the loss of POLE4 alters replication profile by slowing down nucleotide incorporation, a phenotype that gets exacerbated upon PARPi, leading to accumulation of ssDNA gaps due to impaired processing of post-replicative gaps and defects in resolving of R-loops.

POLE4 protects against replication stress induced by PARPi and ATRi

Accumulation of unprocessed ssDNA gaps induces replication stress and alters cell cycle progression (62). To assess whether POLE4 KO cells stall at a certain phase of the cell cycle, we probed their cell cycle profile. All POLE4 KO clones showed mild accumulation in G2/M without treatment, which was strongly elevated upon PARPi treatment (Figure 4A, Supplementary Figure S4A), suggesting already a low level of replication stress in the absence of POLE4, which gets strongly potentiated upon PARP inhibition. During DNA replication, the phosphatidylinositol 3-kinase-related kinase (PIKK) family member Ataxia-telangiectasia mutated and RAD3-related (ATR) orchestrates origin firing, protects replication forks and regulates cell cycle progression (63). Indeed, we detected that ATR activity was mildly increased in POLE4 KO cells as compared to wild-type, revealed by autophosphorylation of residue Threonine 1989 (T1989), a proxy for ATR activation (64) (Figure 4B). PARPi treatment strongly enhanced the pATR signal, which was reversed by ATR inhibitor (ATRi), indicating a specific role of ATR in mediating PARPi-induced replication stress response (Figure 4B).

Our results revealed that the replication profile of POLE4 KO is impaired, which is potentiated by PARPi treatment leading to the accumulation of ssDNA gaps and replication

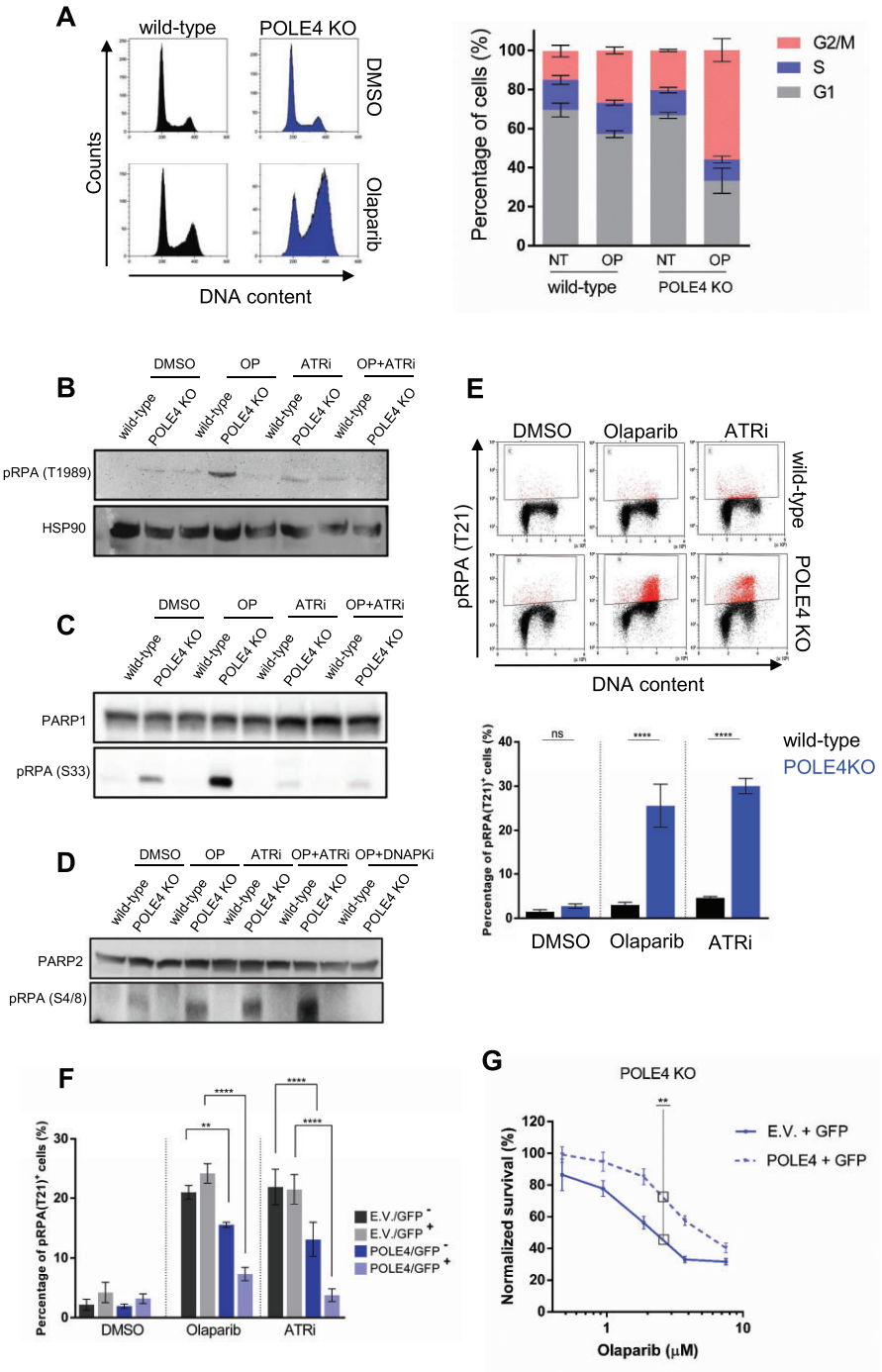

Figure 4. POLE4 protects against replication stress induced by PARPi and ATRi. (**A**, left) Representative FACS experiment showing cell-cycle profile of cells with the indicated genotypes with or without Olaparib treatment (5 μM, 24 h). (Right) Percentages of cells in G1, S or G2/M cell cycle phases are presented as mean ± SEM of three independent experiments ($n = 3$). (**B**, **C**) A representative western blot out of three independent repetitions of HeLa wild-type and POLE4 KO cells with the indicated antibodies upon treatment with Olaparib (5 μM, 24 h), ATRi (5 μM, 24 h) or both of them. HSP70 and PARP1 are used as a loading control. (**D**) A representative western blot out of three independent repetitions of HeLa wild-type and POLE4 KO cells with the anti-pRPA (S4/8) upon treatment with Olaparib (5 μM, 24 h), ATRi (5 μM, 24 h), their combination or Olaparib plus DNA-PKi (5 μM, 24 h). PARP2 is used as a loading control. (**E**) Flow cytometry of HeLa wild-type or POLE4 KO cells after culturing for 24 h with Olaparib (5 μM), ATRi (5 μM) or DMSO. The cells were fixed and stained with anti-pRPA (T21) and propidium-iodide (DNA content). (Top) FACS images of a representative experiment are shown. (Bottom) Bar chart shows the mean ± SEM of percentages of pRPA(T21) positive cells from three independent experiments ($n = 3$). Asterisks indicate *P*-values obtained by one-way ANOVA (ns, not significant, **** $P < 0.0001$). (**F**) Percentage of pRPA (T21) positive cells upon transient POLE4 expression. POLE4 KO cells were transfected with GFP and empty (E.V.) or POLE4 coding plasmids for 48 h, then treated with Olaparib (5 μM), ATRi (5 μM) or with DMSO for 16 h. The cells were fixed and stained with anti-pRPA (T21) and propidium-iodide. RPA (T21) phosphorylation is shown in cells gated to GFP positive and negative populations during flow cytometry analysis. Data are mean ± SEM from three independent experiments ($n = 3$). Asterisks indicate *P*-values obtained by one-way ANOVA (** $P < 0.01$, **** $P < 0.0001$). (**G**) Cell survival assay showing Olaparib sensitivity of POLE4 KO cells transfected with GFP and empty (E.V.) or POLE4 coding plasmids. Olaparib treatment was refreshed once during the 6-day long experiment. The graphs show the relative survival normalized to the untreated samples of each transfection. Data are mean ± SEM ($n = 3$) of triplicate samples from one representative out of three independent experiments. Asterisks indicate *P*-values obtained by two-way ANOVA (** $P < 0.01$).

stress induction. Replication protein A (RPA) acts as a sensor of ssDNA and signals different levels of replication stress by getting phosphorylated sequentially on multiple residues by PIKKs, with Serine 33 (S33) being phosphorylated early on upon mild replication stress, followed by Serine 4 and 8 (S4/8) and Threonine 21 (T21) upon severe replication stress (65). Consistent with mild replication stress upon the loss of POLE4, we detected pRPA (S33) signal in untreated POLE4 KO cells, which got exacerbated upon PARPi (Figure 4C). The pRPA (S33) signal was abolished by ATRi, in line with being phosphorylated by ATR (65). Furthermore, we detected pRPA (S4/8) signal in POLE4 KO cells without any treatment, which was enhanced upon PARPi, ATRi and their combination (Figure 4D) indicating elevated levels of replication stress. This signal was suppressed by treatment with DNA-dependent protein kinase (DNA-PK) inhibitor (DNA-PKi) (Figure 4D), consistent with the phosphorylation of this residue by DNA-PK (65). ATRi-induced severe replication stress in POLE4 KO is also reflected in their reduced survival (Supplementary Figure S4B), indicating a synthetic lethal interaction between ATR inhibition and POLE4 deficiency in line with previous reports (21,55).

The inability of POLE4 KO to resolve replication stress led to increased severity of the phenotype as PARPi treatment caused a strong increase in the pRPA (T21) signal, which was characteristic to the G2/M arrested population in POLE4 KO, but not detected in wild-type cells (Figure 4E). This phenotype was also observed in all other POLE4 KO clones (Supplementary Figure S4C), confirming that it was not clone-dependent. Interestingly, RPA phosphorylation on T21 residue was also induced by ATR inhibition (Figure 4E), suggesting a severe replication stress, which may ultimately lead to replication catastrophe due to accumulation of DSB indicated by phosphorylation of serine 139 on the histone variant H2AX (also called γH2A.X). We measured γH2A.X level upon MMS-induced DSB as a positive control. As expected, MMS treatment induced γH2A.X signal, however, there was no significant difference in the percentage of γH2A.X positive cells between wild-type and POLE4 KO cells (Supplementary Figure S4D), which is in line with our previous observation that POLE4 KO and wild-type cells were equally sensitive to MMS in a cell survival assay (Figure 2D). While PARPi treatment did not lead to DSB in wild-type or in POLE4 KO as indicated by low levels of γH2A.X (Supplementary Figure S4D), ATRi caused a dramatic increase in the percentage of γH2A.X positive cells only in POLE4 KO (Supplementary Figure S4D) revealing differences in the cellular response to PARPi and ATRi. It has been reported that ATRi can induce ssDNA accumulation, which can be converted to DSB leading to phosphorylation and activation of other PIKKs, such as DNA-PK and Ataxia-telangiectasia mutated (ATM) (63).

To address the role of POLE4 in protecting against severe replication stress, we measured the pRPA (T21) signal in POLE4 KO cells co-transfected with a plasmid expressing untagged POLE4 or an empty vector together with a GFP-expressing plasmid and subjected these cells to treatment with either PARPi or ATRi. After transfection, we sorted the cells using FACS into two populations: one that was GFP^+, likely to have POLE4 expression as well, and one that was GFP^- which corresponded to cells that were likely not expressing POLE4 (Supplementary Figure S4E, F). In samples co-transfected with the GFP expressing plasmid and empty vector, the pRPA (T21) signal was detected in POLE4 KO upon either PARPi or ATRi treatment in both GFP positive and negative populations (Figure 4F), indicating that GFP expression itself does not alter the level of replication stress in POLE4 KO. In cells co-transfected with the plasmids expressing GFP and POLE4, pRPA (T21) was detected upon treatment with either PARPi or ATRi in the GFP^- population corresponding to no POLE4 expression. Importantly, this phenotype was rescued in the GFP^+ population, where POLE4 was expressed (Figure 4F, Supplementary Figure S4E, F). The transient expression of POLE4 in POLE4 KO also reduced their sensitivity to PARPi as compared to the empty vector control (Figure 4G).

Altogether, these results demonstrate that POLE4 ensures normal cell-cycle progression and curbs replication stress associated with PARPi or ATRi treatment.

Distinct roles of PIKKs in response to PARPi-induced replication stress in POLE4 KO

Our results suggest the role of other members of the PIKK family besides ATR in replication stress signaling in the POLE4 KO. Therefore, we probed for the activity of ATM and DNA-PK as well. While DNA-PK activity, as revealed by its autophosphorylation, was not changed in wild-type cells upon Olaparib and/or ATRi treatment, it was markedly elevated in POLE4 KO after 24 h of ATRi treatment alone or when combined with Olaparib (Figure 5A). ATM phosphorylation (pATM)—an indicator of ATM activation—was modestly elevated upon incubation of the wild-type cells either with Olaparib or with ATRi alone, while strongly enhanced in the presence of their combination. Compared to wild-type cells, the ATM phosphorylation was further increased in POLE4 KO cells both in the case of single Olaparib or ATRi treatment and when combined (Figure 5A). These results reveal the complex interplay between PIKKs in POLE4 KO cells in response to replication stress.

Next, we aimed to reveal the role of PIKKs in the PARPi-induced cell cycle arrest. The cell cycle of wild-type cells was not affected by either ATRi, ATMi or DNA-PKi alone, and Olaparib treatment caused a mild G2/M accumulation with or without PIKK inhibitors (Figure 5B, Supplementary Figure S5A). In line with the ATRi sensitivity of POLE4 KO, ATRi treatment alone, but not the other PIKK inhibitors, caused a marked accumulation of G2/M cells in POLE4 KO (Figure 5B, Supplementary Figure S5A). In contrast to ATR and ATM inhibition that had little effect on Olaparib-induced cell cycle arrest in POLE4 KO, DNA-PKi reduced it (Figure 5B, Supplementary Figure S5A) indicating a role of DNA-PK activation in the cell-cycle arrest upon PARPi in POLE4 KO.

To refine whether Olaparib leads to G2 or mitotic arrest, we quantified a mitotic marker, histone H3 phosphorylated on Serine 10 (pH3S10). Despite the strong accumulation of cells with DNA content characteristic to G2/M detected in Olaparib-treated POLE4 KO, the ratio of mitotic cells within the G2/M population was reduced (Figure 5C, Supplementary Figure S5B). This shows that POLE4 KO cells are arrested in G2 upon PARP inhibition, presumably due to the accumulation of ssDNA gaps and ATR activation. ATR inhibition promoted the transition of POLE4 KO cells into mitosis, even if PARP1 was inhibited (Figure 5C, Supplementary Figure S5B) confirming that ATR is the major checkpoint kinase responsible for the G2/M cell cycle arrest in POLE4 KO. The proportion of mitotic cells did not

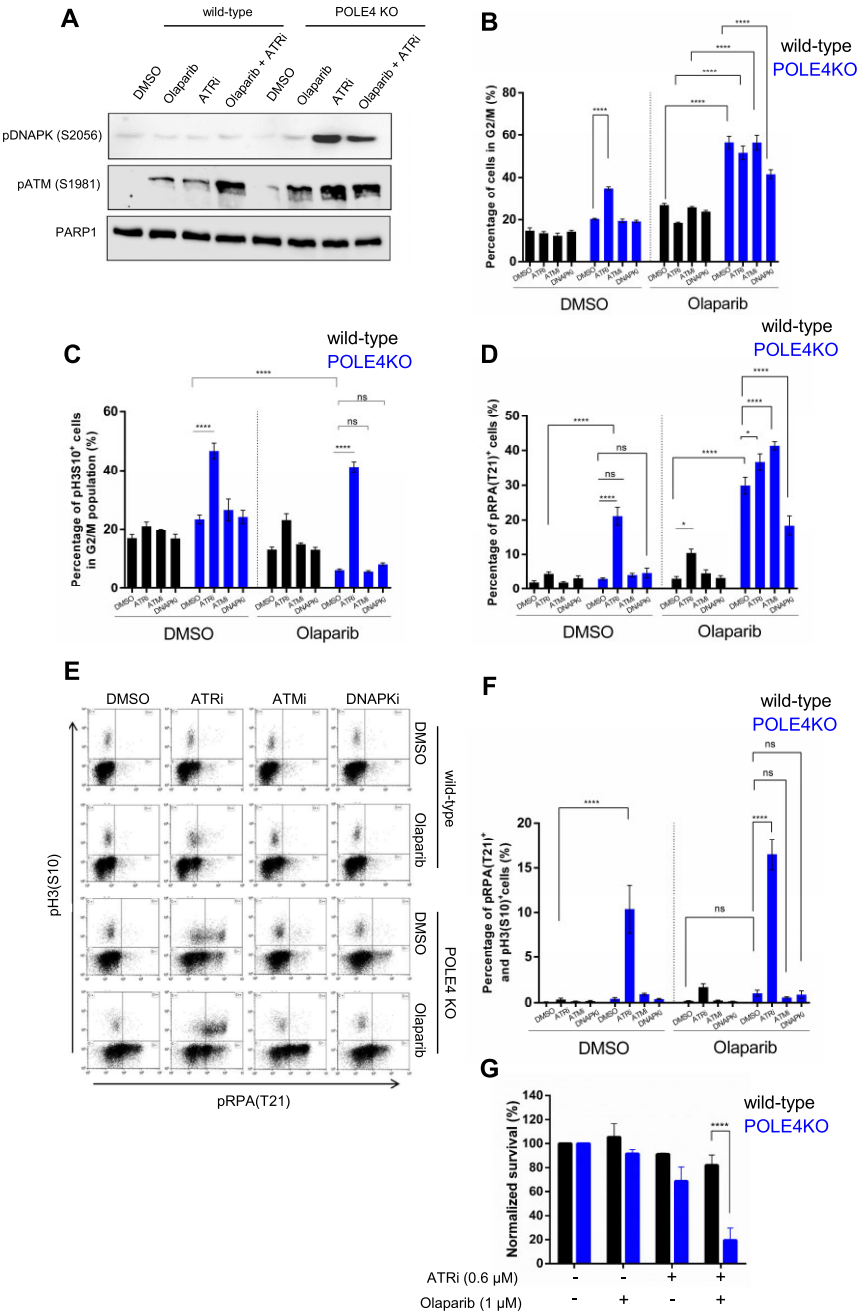

Figure 5. Distinct roles of PIKKs in response to PARPi-induced replication stress in POLE4 KO. (**A**) A representative Western blot out of three independent repetitions of HeLa wild-type and POLE4 KO cells with the indicated antibodies upon treatment with Olaparib (5 μM, 24 h), ATRi (5 μM, 24 h) or both of them. PARP1 is used as a loading control. (**B**) Percentages of HeLa wild-type and POLE4 KO in G2/M phase after 24 h of Olaparib (5 μM) and/or ATRi (5 μM), ATMi (5 μM) DNA-PKi (5 μM) treatment. DMSO was used as a solvent control. Percentages of cells in G2/M were determined from cell cycle analysis measured by flow cytometry. Bar chart shows the mean ± SEM from five independent experiments ($n = 5$). Asterisks indicate *P*-values obtained by one-way ANOVA (**** $P < 0.0001$). (**C**) Percentages of HeLa wild-type and POLE4 KO in mitosis after 24h treatment with Olaparib (5 μM) and/or ATRi (5 μM), ATMi (5 μM), DNA-PKi (5 μM). DMSO was used as a solvent control. The cells were stained with anti-pH3(S10) and propidium-iodide, and the ratio of mitotic cells was determined by pH3(S10) positivity within the G2/M gate in flow cytometry. Bar chart shows the mean ± SEM from three independent experiments ($n = 3$). Asterisks indicate *P*-values obtained by one-way ANOVA (ns, not significant, **** $P < 0.0001$). (**D**) Percentages of phospho-RPA (T21) positive HeLa wild-type or POLE4 KO cells after 24 h of Olaparib (5 μM) and/or ATRi (5 μM), ATMi (5 μM), DNA-PKi (5 μM) treatment. DMSO was used as a solvent control. The cells were stained with anti-pRPA (T21) and propidium-iodide (DNA content), and the percentages of pRPA (T21) positive cells were determined by flow cytometry. Bar chart shows the mean ± SEM of percentages of pRPA (T21) positive cells from four independent experiments ($n = 4$). Asterisks indicate *P*-values obtained by one-way ANOVA (ns, not significant, * $P < 0.05$, **** $P < 0.0001$). (**E**, **F**) Mitotic entry of pRPA (T21) positive HeLa wild-type or POLE4 KO cells after 24 h of Olaparib (5 μM) and/or ATRi (5 μM), ATMi (5 μM), DNA-PKi (5 μM) treatment. DMSO was used as a solvent control. The cells were stained with anti-pH3(S10) and anti-pRPA (T21) and analyzed by flow cytometry. (**E**) FACS image of a representative experiment is shown. (**F**) Bar chart shows the mean ± SEM of percentages of pRPA (T21)/pH3(S10) double positive cells from three independent experiments ($n = 3$). Asterisks indicate *P*-values obtained by one-way ANOVA (ns, not significant, **** $P < 0.0001$). (**G**) Cell survival assay of HeLa wild-type and POLE4 KO cells treated with Olaparib (1 μM) and/or ATRi (0.6 μM). The columns represent normalized survival of the cells upon the indicated treatments. The treatment was refreshed once during the 7-day experiment. Mean ± SEM ($n = 3$). The figure is derived from three independent experiments. Asterisks indicate *P*-values obtained by two-way ANOVA (**** $P < 0.0001$).

change in the presence of other PIKK inhibitors (Figure 5C, Supplementary Figure S5B).

As pRPA (T21) is a marker of severe replication stress and it overlapped with G2/M arrest in PARPi-treated POLE4 KO cells, we aimed to address which PIKK was responsible for this signal. Of the tested PIKK inhibitors, only ATRi increased the percentage of pRPA (T21) positive wild-type cells upon Olaparib treatment significantly (Figure 5D, Supplementary Figure S5C). As we have shown previously, single ATRi treatment induced pRPA (T21) phosphorylation (Figure 4E), but neither ATMi nor DNA-PKi treatment alone changed the fraction of pRPA (T21) positive POLE4 KO cells (Figure 5D, Supplementary Figure S5C). On the other hand, all PIKK inhibitors altered the percentage of pRPA (T21) positive POLE4 KO to Olaparib: ATRi and ATMi increased the percentage of pRPA positive cells, while DNA-PKi decreased it (Figure 5D, Supplementary Figure S5C). The double staining of pH3 (S10) and pRPA (T21) also revealed that the Olaparib-induced pRPA (T21) positive POLE4 KO cells were blocked in G2 and they were prevented from entering mitosis, unless released from the control of ATR (Figure 5E, F). ATR inhibition allowed the cells with persisting replication defects to prematurely enter mitosis leading to replication catastrophe as revealed by γH2A.X positive cells (Supplementary Figure S4D) and reduced cell survival (Supplementary Figure S4B) and (54,66). In support of this, while the treatment with low dose of either Olaparib or ATRi alone had minor effect on the survival of POLE4 KO cells, combining them synergistically killed POLE4 KO cells (Figure 5G). This establishes the loss of POLE4 as a major sensitizing event to co-treatment with ATRi and PARPi, a drug combination being tested in clinical trials (67).

Together, these results emphasize the importance of ATR signaling in restraining POLE4 KO from entering mitosis upon PARPi-induced replication stress. Furthermore, our data reveal that DNA-PK activity contributes to the replication stress observed in POLE4-deficient cells.

POLE4 acts parallel to BRCA1 in inducing PARPi sensitivity

Since PARPi sensitivity was first described in BRCA-deficient cells displaying impaired HR (1,2), we aimed to check whether PARPi-induced replication stress response could be detected when BRCA1 was missing. Similar to POLE4 KO, downregulating BRCA1 resulted in increased levels of pRPA upon Olaparib treatment (Figure 6A). Strikingly, co-depletion of POLE4 and BRCA1 had a synthetic impact on pRPA levels compared to single depletion (Figure 6A). This suggests that POLE4 might function parallel to BRCA1, and that it is not part of the canonical HR pathway.

To confirm this hypothesis, we examined PARPi-induced Rad51 foci formation by confocal microscopy. The recombinase Rad51 is a crucial protein in the process of HR: following DNA end-resection, Rad51 binds ssDNA overhangs and leads the homology search and strand invasion to facilitate homology-directed repair (1,2). Consistent with previous reports describing impairment in HR, BRCA1-deficient cells displayed reduced Rad51 foci formation compared to the BRCA1 proficient controls (Supplementary Figure S6A, B). Conversely, POLE4 KO cells were able to efficiently form Rad51 foci upon Olaparib treatment, even to a higher extent than their wild-type counterpart (Figure 6B). This observation can be attributed to the elevation of ssDNA gaps we described previously in POLE4 KO following PARPi (Figure 3C, D).

Since POLE4 is not redundant in function with BRCA1, we reasoned that PARPi sensitivity could be potentiated if both proteins were missing. To that end, we downregulated BRCA1 in wild-type and POLE4 KO and challenged the cells with a low dose of Olaparib. BRCA1 depletion in POLE4 KO cells resulted in massive killing of these cells in comparison to the loss of either POLE4 or BRCA1 alone (Figure 6C), indicating that POLE4 might serve as a potential target for enhancing sensitivity of BRCA1-deficient tumors to PARPi.

A common mechanism for BRCA1-deficient tumors acquiring resistance to PARPi is the rewiring of HR through loss of the NHEJ factor 53BP1 (68–70). Given that sensitivity of POLE4 KO to PARPi is not going through defective HR, we sought to investigate whether targeting POLE4 could overcome PARPi resistance observed upon loss of 53BP1 in BRCA1-deficient cells (68–70). To that end, we utilized RNAi-mediated downregulation of either BRCA1, 53BP1 or their combination in wild-type and POLE4 KO cells. Consistent with previous reports, downregulating BRCA1 in wild-type cells sensitized them to Olaparib, which was rescued with combined depletion of BRCA1/53BP1 (Figure 6D, Supplementary Figure S6C). As mentioned earlier, BRCA1 depletion in POLE4 KO cells resulted in severe sensitization to Olaparib in comparison to missing either POLE4 or BRCA1 alone (Figure 6D). Significantly, the co-depletion of BRCA1/53BP1 did not rescue PARPi sensitivity of POLE4 KO as in the case of wild-type cells (Figure 6D, Supplementary Figure S6C), indicating that targeting POLE4 not only enhanced PARPi synthetic lethality in BRCA1-depleted cells but also bypassed the synthetic viability induced by reactivation of HR upon 53BP1 loss in BRCA1-compromised cells (69).

Discussion

Our findings confirm that the deficiency of POLE4 results in heightened sensitivity to PARPi. While Olaparib inhibits both PARP1 and PARP2 (7), our data supports the notion that the toxicity of PARPi in POLE4 KO is primarily associated with PARP1 rather than PARP2, justifying the rationale behind the development of PARP1-specific inhibitors (71,72). The observed synthetic lethality between POLE4 deficiency and PARP inhibition is ascribed to the prolonged presence of inhibited PARP1 on chromatin rather than the blocked ADP-ribosylation activity of PARP1. This is substantiated by the fact that the depletion of PARP1 mitigates the toxicity of PARPi in POLE4 KO.

Based on our current understanding, the process of PARP1 trapping necessitates the presence of lesions that PARP1 can bind to, leading to its activation in the absence of PARPi. Considering the observed synthetic lethality, two scenarios can be hypothesized. On one hand, the absence of POLE4 might contribute to an increase in lesions that activate PARP1. Consequently, a higher prevalence of these activating lesions could result in more PARP1 trapping and increased sensitivity in the presence of PARPi. Here, one would anticipate elevated ADP-ribosylation levels. However, our findings reveal no increase either in S-phase PAR levels or in ADPr in response to DNA damage in POLE4 KO as compared to wild-type, therefore, they are more consistent with the alternative scenario suggesting that POLE4 plays a role in mitigating the toxicity induced by PARP trapping.

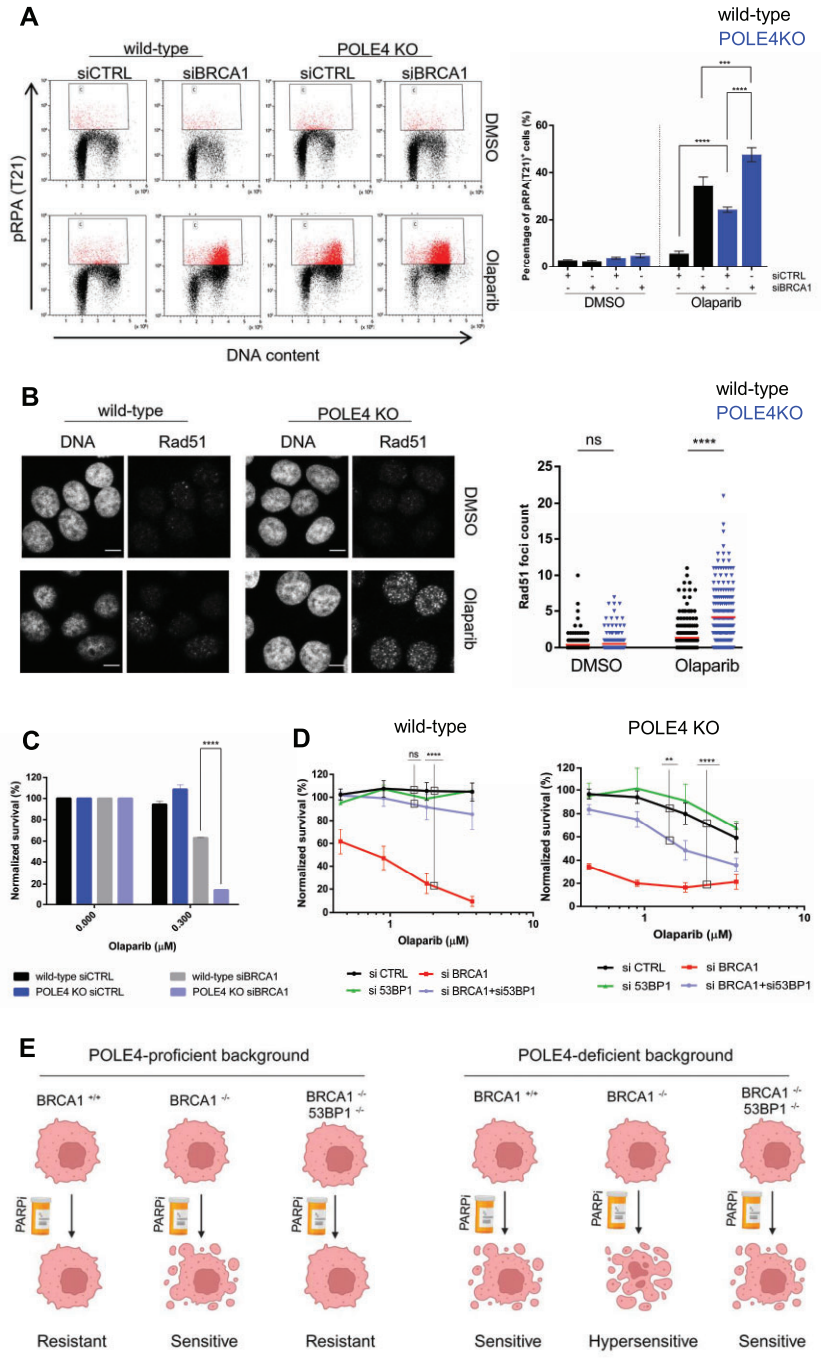

Figure 6. POLE4 acts parallel to BRCA1 in inducing PARP inhibitor sensitivity. (**A**) Flow cytometry of HeLa wild-type or POLE4 KO cells with downregulated BRCA1, treated with Olaparib (5 μM, 24 h) or DMSO. The cells were fixed and stained with anti-pRPA (T21) and propidium-iodide (DNA content). (Left) The figure is a representative of three independent experiments. (Right) Bar chart shows the mean ± SEM of percentages of pRPA(T21) positive cells from three independent experiments ($n = 3$). Asterisks indicate *P*-values obtained by one-way ANOVA (*** $P < 0.001$, **** $P < 0.0001$). (**B**, left) Representative images of immunofluorescence experiment of Rad51 foci formation in HeLa wild-type and POLE4 KO cells upon treatment of Olaparib (10 μM, 48 h), Scale bar, 10 μm. (Right) Quantification of Rad51 foci count in the indicated cell lines upon the indicated treatment. The experiment is representative of three independent repetitions. Asterisks indicate *P*-values obtained by one-way ANOVA (ns, not significant, **** $P < 0.0001$). (**C**) Cell survival assay of HeLa wild-type and POLE4 KO cells transfected with the indicated siRNA and treated with the indicated concentration of Olaparib for 7 days, with the treatment being changed once, before calculating the relative survival normalized to the untreated samples of each genotype. Mean ± SEM ($n = 3$). The figure is derived from three independent experiments. Asterisks indicate *P*-values obtained by two-way ANOVA (**** $P < 0.0001$). (**D**) Cell survival assay of HeLa wild-type and POLE4 KO cells downregulated of either BRCA1, 53BP1 or both of them using siRNA transfection and treated with the indicated concentrations of Olaparib for 7 days, with the treatment being changed once. The curves are normalized to the untreated condition corresponding to each genotype. Mean ± SEM ($n = 3$). The figures are derived from three independent experiments. Asterisks indicate *P*-values obtained by two-way ANOVA (ns, not significant, ** $P < 0.01$, **** $P < 0.0001$). (**E**) In POLE4-proficient cells, PARPi is synthetic lethal with BRCA1 deficiency, which is reversed upon loss of both BRCA1 and 53BP1 leading to PARPi acquired resistance. In POLE4-deficient background, the cells become sensitive to PARPi, and this sensitivity is further enhanced upon loss of BRCA1. Importantly, the acquired resistance to PARPi due to co-depletion of BRCA1 and 53BP1 can be bypassed in POLE4-deficeint cells, highlighting a potential therapeutic exploitation in the clinic. Created with BioRender.com

PARPi cytotoxicity is associated with the accumulation of ssDNA gaps (17,18). Such ssDNA gaps can arise from various sources, such as defective Okazaki fragments processing (17,52), or stalled replication forks (18). Unligated Okazaki fragments have been proposed to be a major source of PARP activity in S-phase. If POLE4 functions to ensure timely processing of Okazaki fragments, then its loss is expected to cause accumulation of ssDNA fragments even without PARPi treatment, such accumulation will be translated into increased PAR levels in S-phase cells just as in BRCA-deficient cells (17). However, POLE4 KO cells do not show increased S-phase PAR signal compared to their wild-type counterparts upon treatment with either PARGi or the combination of PARGi and Fen1i, the latter interfering with Okazaki fragment processing indicating that the loss of POLE4 does not increase the formation of Okazaki fragments.

Yeast studies identify a role of the POLε complex in the activation of S-phase checkpoint either through the C-terminal of the catalytic subunit or the accessory subunit Dpb4 in response to replication stress (25,73,74). Importantly, these accessory subunits also contribute to normal replication fork progression (24). Moreover, several reports have shown that the loss of POLE4 causes reduced replication origin activation in mice and worms (27,75,76). These replication defects remain, however, relatively mild unless these cells are subjected to replication stress inducers (27). These findings, together with our data that POLE4 KO cells elicit reduced replication rate under normal conditions and hypersensitivity to replication stress, as well as other previous reports (21,54,55), all point towards a key role of POLE4 in replication stress tolerance.

PARPi has been reported to increase fork speed, which induces replication stress (51). Further, PARP1 plays a role in the resolution of R-loops (58–60), whose function when inhibited may also interfere with efficient replication, a phenotype that was reported recently and correlated with PARPi sensitivity (56). Considering the reduced fork speed in POLE4 KO upon PARPi, it is tempting to speculate that the instability of fork progression due to POLE4 loss is potentiated when PARP1 is trapped on chromatin and interferes with efficient replication, which ultimately lead to the replication stress phenotype in POLE4 deficient cells. Reduced replication speed due to discontinuities of DNA synthesis requires efficient post-replicative repair and resolving of R-loops to alleviate the genomic stress accompanied by elevation of such DNA gaps (57,77). Our results suggest that impairment of these processes is likely to contribute to the low replication stress tolerance of POLE4 KO.

The arising ssDNA gaps in POLE4 KO are recognized by ATR and lead to its activation, the critical kinase in the protection against replication stress (78). ATR blocks cells from entering mitosis with unrepaired damage and reduces the replication rate to prevent potentiating replication stress (79). Along with this, several studies have shown that combining PARPi and ATRi synergistically kills BRCA 1/2 deficient cells by causing premature mitotic release (66,80). The toxicity of drug combinations could be further reduced through identifying novel genetic alterations that enhance susceptibility towards these drugs (54). Based on our results, POLE4 can serve as a target to enhance the sensitivity of cancer cells to the combination of PARPi and ATRi.

PARPi were reported to cause ATM activation (81,82). Our data further validate ATM activation as part of the canonical response to both PARPi and ATRi as it is evident in wild-type cells, and much increased in POLE4 KOs due to their increased sensitivity. Conversely, DNA-PK signaling remains inactive in wild-type cells following PARPi or ATRi treatment, while being excessively activated in POLE4 KO cells, contributing to some of the observed toxicity. Similar upregulation of DNA-PK signaling has been documented in HR-deficient cells exposed to PARPi (83).

Importantly, our results place POLE4 in a BRCA1-independent pathway underlying PARPi resistance. In contrast to BRCA1-deficient cells, sensitivity of POLE4 KO cells to PARPi is not rescued by the restoration of HR upon 53BP1 depletion (Figure 6E). Sensitivity of BRCA1-deficient tumors to PARPi can be attributed to three main mechanisms: (i) HR deficiency, (ii) loss of replication fork protection, (iii) defects in Okazaki fragments processing. POLE4 KO cells differ from BRCA1-deficiency in all these mechanisms. Genetic deletions of POLE4 have been identified in cases of malignant mesothelioma (84) and non–small cell lung cancer (85). Therefore, our data suggest that POLE4 might serve as a biomarker for identifying tumors that can respond to PARPi treatment regardless of their HR status.

Data availability

The data underlying this article are available in the article and in its online supplementary material. Further data underlying this article will be shared on reasonable request to the corresponding author.

Supplementary data

Supplementary Data are available at NAR Online.

Acknowledgements

We would like to thank the technical assistance of Adrián Kószó in the laboratory of G.T., Bernadett Bóna in the laboratory of L.H. and that of the Microscopy Rennes Imaging Center (BIOSIT, Université Rennes 1). The authors also acknowledge the contribution of the Core Facility (Cellular Imaging Laboratory and Laboratory of Functional Genomics) of the HUN-REN Biological Research Centre. The graphical abstract and the model in Figure 6 were created with BioRender.com.

Authors contributions: The authors confirm contribution to the paper as follows: study conception and design: G.T., R.F.B., H.M.; data collection: H.M., R.F.B., M.Me., E.P.J., A.G.K., A.M., M.Mo., S.Z., R.S., A.B.S.; analysis and interpretation of results: H.M., R.F.B., G.T., M.Mo., S.H., L.H., A.J.B., N.D.L.; draft manuscript preparation: H.M., R.F.B., G.T. All authors reviewed the results and approved the final version of the manuscript.

Funding

The work in the Timinszky laboratory was supported by the National Research Development and Innovation Office [K143248]; G.T. and H.M. were supported by the EMBO Advanced Collaboration Grant (10265); A.G.K. was supported by the National Academy of Scientist Education Program of the National Biomedical Foundation under the sponsorship of the Hungarian Ministry of Culture and Innovation and

the New National Excellence Program of the Hungarian Ministry of Culture and Innovation [UNKP-22-3-SZTE-264]; for this work, S.H.'s group received financial support from the Agence Nationale de la Recherche [AROSE, ANR-22-CE12-0039]; Institut National du Cancer [PLBIO-2019]; Institut Universitaire de France; the Bowman lab was supported by Wellcome Trust [208801/Z/17/Z]; research in the Haracska laboratory was supported by the National Research, Development and Innovation Office [PharmaLab, RRF-2.3.1-21-2022-00015 and TKP-31-8/PALY-2021]. Funding for open access charge: National Research Development and Innovation Office [K143248].

Conflict of interest statement

None declared.

References

1. Bryant,H.E., Schultz,N., Thomas,H.D., Parker,K.M., Flower,D., Lopez,E., Kyle,S., Meuth,M., Curtin,N.J. and Helleday,T. (2005) Specific killing of BRCA2-deficient tumours with inhibitors of poly(ADP-ribose) polymerase. *Nature*, **434**, 913–917.
2. Farmer,H., McCabe,N., Lord,C.J., Tutt,A.N.J., Johnson,D.A., Richardson,T.B., Santarosa,M., Dillon,K.J., Hickson,I., Knights,C., *et al.* (2005) Targeting the DNA repair defect in BRCA mutant cells as a therapeutic strategy. *Nature*, **434**, 917–921.
3. Bunting,S.F., Callén,E., Wong,N., Chen,H.-T., Polato,F., Gunn,A., Bothmer,A., Feldhahn,N., Fernandez-Capetillo,O., Cao,L., *et al.* (2010) 53BP1 inhibits homologous recombination in Brca1-deficient cells by blocking resection of DNA breaks. *Cell*, **141**, 243–254.
4. Langelier,M.-F., Planck,J.L., Roy,S. and Pascal,J.M. (2012) Structural basis for DNA damage-dependent poly(ADP-ribosyl)ation by human PARP-1. *Science*, **336**, 728–732.
5. Barkauskaite,E., Jankevicius,G., Ladurner,A.G., Ahel,I. and Timinszky,G. (2013) The recognition and removal of cellular poly(ADP-ribose) signals. *FEBS J.*, **280**, 3491–3507.
6. Sellou,H., Lebeaupin,T., Chapuis,C., Smith,R., Hegele,A., Singh,H.R., Kozlowski,M., Bultmann,S., Ladurner,A.G., Timinszky,G., *et al.* (2016) The poly(ADP-ribose)-dependent chromatin remodeler Alc1 induces local chromatin relaxation upon DNA damage. *Mol. Biol. Cell*, **27**, 3791–3799.
7. Murai,J., Huang,S.N., Das,B.B., Renaud,A., Zhang,Y., Doroshow,J.H., Ji,J., Takeda,S. and Pommier,Y. (2012) Trapping of PARP1 and PARP2 by clinical PARP inhibitors. *Cancer Res.*, **72**, 5588–5599.
8. Ying,S., Hamdy,F.C. and Helleday,T. (2012) Mre11-dependent degradation of stalled DNA replication forks is prevented by BRCA2 and PARP1. *Cancer Res.*, **72**, 2814–2821.
9. Lord,C.J. and Ashworth,A. (2016) BRCAness revisited. *Nat. Rev. Cancer*, **16**, 110–120.
10. Gibbs-Seymour,I., Fontana,P., Rack,J.G.M. and Ahel,I. (2016) HPF1/C4orf27 Is a PARP-1-interacting protein that regulates PARP-1 ADP-ribosylation activity. *Mol. Cell*, **62**, 432–442.
11. Zimmermann,M., Murina,O., Reijns,M.A.M., Agathanggelou,A., Challis,R., Tarnauskaitė,Ž., Muir,M., Fluteau,A., Aregger,M., McEwan,A., *et al.* (2018) CRISPR screens identify genomic ribonucleotides as a source of PARP-trapping lesions. *Nature*, **559**, 285–289.
12. Juhász,S., Smith,R., Schauer,T., Spekhardt,D., Mamar,H., Zentout,S., Chapuis,C., Huet,S. and Timinszky,G. (2020) The chromatin remodeler ALC1 underlies resistance to PARP inhibitor treatment. *Sci. Adv.*, **6**, eabb8626.
13. Hewitt,G., Borel,V., Segura-Bayona,S., Takaki,T., Ruis,P., Bellelli,R., Lehmann,L.C., Sommerova,L., Vancevska,A., Tomas-Loba,A., *et al.* (2021) Defective ALC1 nucleosome remodeling confers PARPi sensitization and synthetic lethality with HRD. *Mol. Cell*, **81**, 767–783.
14. Blessing,C., Mandemaker,I.K., Gonzalez-Leal,C., Preisser,J., Schomburg,A. and Ladurner,A.G. (2020) The oncogenic helicase ALC1 regulates PARP inhibitor potency by trapping PARP2 at DNA breaks. *Mol. Cell*, **80**, 862–875.
15. Verma,P., Zhou,Y., Cao,Z., Deraska,P.V., Deb,M., Arai,E., Li,W., Shao,Y., Puentes,L., Li,Y., *et al.* (2021) ALC1 links chromatin accessibility to PARP inhibitor response in homologous recombination-deficient cells. *Nat. Cell Biol.*, **23**, 160–171.
16. Niraj,J., Färkkilä,A. and D'Andrea,A.D. (2019) The Fanconi anemia pathway in cancer. *Annu Rev Cancer Biol*, **3**, 457–478.
17. Cong,K., Peng,M., Kousholt,A.N., Lee,W.T.C., Lee,S., Nayak,S., Krais,J., VanderVere-Carozza,P.S., Pawelczak,K.S., Calvo,J., *et al.* (2021) Replication gaps are a key determinant of PARP inhibitor synthetic lethality with BRCA deficiency. *Mol. Cell*, **81**, 3227.
18. Simoneau,A., Xiong,R. and Zou,L. (2021) The trans cell cycle effects of PARP inhibitors underlie their selectivity toward BRCA1/2-deficient cells. *Genes Dev.*, **35**, 1271–1289.
19. Vaitsiankova,A., Burdova,K., Sobol,M., Gautam,A., Benada,O., Hanzlikova,H. and Caldecott,K.W. (2022) PARP inhibition impedes the maturation of nascent DNA strands during DNA replication. *Nat. Struct. Mol. Biol.*, **29**, 329–338.
20. Clements,K.E., Schleicher,E.M., Thakar,T., Hale,A., Dhoonmoon,A., Tolman,N.J., Sharma,A., Liang,X., Imamura Kawasawa,Y., Nicolae,C.M., *et al.* (2020) Identification of regulators of poly-ADP-ribose polymerase inhibitor response through complementary CRISPR knockout and activation screens. *Nat. Commun.*, **11**, 6118.
21. Su,D., Feng,X., Colic,M., Wang,Y., Zhang,C., Wang,C., Tang,M., Hart,T. and Chen,J. (2020) CRISPR/CAS9-based DNA damage response screens reveal gene-drug interactions. *DNA Repair (Amst.)*, **87**, 102803.
22. Burgers,P.M.J. and Kunkel,T.A. (2017) Eukaryotic DNA replication fork. *Annu. Rev. Biochem.*, **86**, 417–438.
23. Pursell,Z.F. and Kunkel,T.A. (2008) DNA polymerase ε: a polymerase of unusual size (and complexity). *Prog. Nucleic Acid Res. Mol. Biol.*, **82**, 101–145.
24. Aksenova,A., Volkov,K., Maceluch,J., Pursell,Z.F., Rogozin,I.B., Kunkel,T.A., Pavlov,Y.I. and Johansson,E. (2010) Mismatch repair-independent increase in spontaneous mutagenesis in yeast lacking non-essential subunits of DNA polymerase ε. *PLoS Genet.*, **6**, e1001209.
25. Puddu,F., Piergiovanni,G., Plevani,P. and Muzi-Falconi,M. (2011) Sensing of replication stress and Mec1 activation act through two independent pathways involving the 9-1-1 complex and DNA polymerase ε. *PLoS Genet.*, **7**, e1002022.
26. Spiga,M.-G. and D'Urso,G. (2004) Identification and cloning of two putative subunits of DNA polymerase epsilon in fission yeast. *Nucleic Acids Res.*, **32**, 4945–4953.
27. Bellelli,R., Borel,V., Logan,C., Svendsen,J., Cox,D.E., Nye,E., Metcalfe,K., O'Connell,S.M., Stamp,G., Flynn,H.R., *et al.* (2018) Polε instability drives replication stress, abnormal development, and tumorigenesis. *Mol. Cell*, **70**, 707–721.
28. Tsubota,T., Tajima,R., Ode,K., Kubota,H., Fukuhara,N., Kawabata,T., Maki,S. and Maki,H. (2006) Double-stranded DNA binding, an unusual property of DNA polymerase ϵ, promotes epigenetic silencing in Saccharomyces cerevisiae. *J. Biol. Chem.*, **281**, 32898–32908.
29. Bellelli,R., Belan,O., Pye,V.E., Clement,C., Maslen,S.L., Skehel,J.M., Cherepanov,P., Almouzni,G. and Boulton,S.J. (2018) POLE3-POLE4 is a histone H3-H4 chaperone that maintains chromatin integrity during DNA replication. *Mol. Cell*, **72**, 112–126.
30. Yu,C., Gan,H., Serra-Cardona,A., Zhang,L., Gan,S., Sharma,S., Johansson,E., Chabes,A., Xu,R.-M. and Zhang,Z. (2018) A mechanism for preventing asymmetric histone segregation onto replicating DNA strands. *Science*, **361**, 1386–1389.

31. Li,Z., Hua,X., Serra-Cardona,A., Xu,X., Gan,S., Zhou,H., Yang,W.-S., Chen,C.-L., Xu,R.-M. and Zhang,Z. (2020) DNA polymerase α interacts with H3-H4 and facilitates the transfer of parental histones to lagging strands. *Sci. Adv.*, **6**, eabb5820.
32. Iida,T. and Araki,H. (2004) Noncompetitive counteractions of DNA polymerase epsilon and ISW2/yCHRAC for epigenetic inheritance of telomere position effect in Saccharomyces cerevisiae. *Mol. Cell. Biol.*, **24**, 217–227.
33. He,H., Li,Y., Dong,Q., Chang,A.-Y., Gao,F., Chi,Z., Su,M., Zhang,F., Ban,H., Martienssen,R., *et al.* (2017) Coordinated regulation of heterochromatin inheritance by Dpb3-Dpb4 complex. *Proc. Natl. Acad. Sci. U.S.A.*, **114**, 12524–12529.
34. Casari,E., Gobbini,E., Gnugnoli,M., Mangiagalli,M., Clerici,M. and Longhese,M.P. (2021) Dpb4 promotes resection of DNA double-strand breaks and checkpoint activation by acting in two different protein complexes. *Nat. Commun.*, **12**, 4750.
35. Pardo,B., Crabbé,L. and Pasero,P. (2017) Signaling pathways of replication stress in yeast. *FEMS Yeast Res.*, **17**, fow101.
36. Lim,K.S., Li,H., Roberts,E.A., Gaudiano,E.F., Clairmont,C., Sambel,L.A., Ponnienselvan,K., Liu,J.C., Yang,C., Kozono,D., *et al.* (2018) USP1 is required for replication fork protection in BRCA1-deficient tumors. *Mol. Cell*, **72**, 925–941.
37. Bairoch,A. (2018) The Cellosaurus, a cell-line knowledge resource. *J. Biomol. Tech.*, **29**, 25–38.
38. Ran,F.A., Hsu,P.D., Wright,J., Agarwala,V., Scott,D.A. and Zhang,F. (2013) Genome engineering using the CRISPR-Cas9 system. *Nat. Protoc.*, **8**, 2281–2308.
39. Carpenter,A.E., Jones,T.R., Lamprecht,M.R., Clarke,C., Kang,I.H., Friman,O., Guertin,D.A., Chang,J.H., Lindquist,R.A., Moffat,J., *et al.* (2006) CellProfiler: image analysis software for identifying and quantifying cell phenotypes. *Genome Biol.*, **7**, R100.
40. Mórocz,M., Gali,H., Raskó,I., Downes,C.S. and Haracska,L. (2013) Single cell analysis of human RAD18-dependent DNA post-replication repair by alkaline bromodeoxyuridine comet assay. *PLoS One*, **8**, e70391.
41. Jansen,J.G., Tsaalbi-Shtylik,A., Hendriks,G., Gali,H., Hendel,A., Johansson,F., Erixon,K., Livneh,Z., Mullenders,L.H.F., Haracska,L., *et al.* (2009) Separate domains of Rev1 mediate two modes of DNA damage bypass in mammalian cells. *Mol. Cell. Biol.*, **29**, 3113–3123.
42. Poot,R.A., Dellaire,G., Hülsmann,B.B., Grimaldi,M.A., Corona,D.F., Becker,P.B., Bickmore,W.A. and Varga-Weisz,P.D. (2000) HuCHRAC, a human ISWI chromatin remodelling complex contains hACF1 and two novel histone-fold proteins. *EMBO J.*, **19**, 3377–3387.
43. Lin,X., Jiang,W., Rudolph,J., Lee,B.J., Luger,K. and Zha,S. (2022) PARP inhibitors trap PARP2 and alter the mode of recruitment of PARP2 at DNA damage sites. *Nucleic Acids Res.*, **50**, 3958–3973.
44. Langelier,M.-F., Lin,X., Zha,S. and Pascal,J.M. (2023) Clinical PARP inhibitors allosterically induce PARP2 retention on DNA. *Sci. Adv.*, **9**, eadf7175.
45. Prokhorova,E., Zobel,F., Smith,R., Zentout,S., Gibbs-Seymour,I., Schützenhofer,K., Peters,A., Groslambert,J., Zorzini,V., Agnew,T., *et al.* (2021) Serine-linked PARP1 auto-modification controls PARP inhibitor response. *Nat. Commun.*, **12**, 4055.
46. Gogola,E., Duarte,A.A., de Ruiter,J.R., Wiegant,W.W., Schmid,J.A., de Bruijn,R., James,D.I., Guerrero Llobet,S., Vis,D.J., Annunziato,S., *et al.* (2018) Selective loss of PARG restores PARylation and counteracts PARP inhibitor-mediated synthetic lethality. *Cancer Cell*, **33**, 1078–1093.
47. Gatti,M., Imhof,R., Huang,Q., Baudis,M. and Altmeyer,M. (2020) The ubiquitin ligase TRIP12 Limits PARP1 trapping and constrains PARP inhibitor efficiency. *Cell Rep.*, **32**, 107985.
48. Krastev,D.B., Li,S., Sun,Y., Wicks,A.J., Hoslett,G., Weekes,D., Badder,L.M., Knight,E.G., Marlow,R., Pardo,M.C., *et al.* (2022) The ubiquitin-dependent ATPase p97 removes cytotoxic trapped PARP1 from chromatin. *Nat. Cell Biol.*, **24**, 62–73.
49. Buchfellner,A., Yurlova,L., Nüske,S., Scholz,A.M., Bogner,J., Ruf,B., Zolghadr,K., Drexler,S.E., Drexler,G.A., Girst,S., *et al.* (2016) A new nanobody-based biosensor to study endogenous PARP1 in vitro and in live human cells. *PLoS One*, **11**, e0151041.
50. Dolce,V., Dusi,S., Giannattasio,M., Joseph,C.R., Fumasoni,M. and Branzei,D. (2022) Parental histone deposition on the replicated strands promotes error-free DNA damage tolerance and regulates drug resistance. *Genes Dev.*, **36**, 167–179.
51. Maya-Mendoza,A., Moudry,P., Merchut-Maya,J.M., Lee,M., Strauss,R. and Bartek,J. (2018) High speed of fork progression induces DNA replication stress and genomic instability. *Nature*, **559**, 279–284.
52. Hanzlikova,H., Kalasova,I., Demin,A.A., Pennicott,L.E., Cihlarova,Z. and Caldecott,K.W. (2018) The importance of poly(ADP-ribose) polymerase as a sensor of unligated Okazaki fragments during DNA replication. *Mol. Cell*, **71**, 319–331.
53. Collins,A., Møller,P., Gajski,G., Vodenková,S., Abdulwahed,A., Anderson,D., Bankoglu,E.E., Bonassi,S., Boutet-Robinet,E., Brunborg,G., *et al.* (2023) Measuring DNA modifications with the comet assay: a compendium of protocols. *Nat. Protoc.*, **18**, 929–989.
54. Zimmermann,M., Bernier,C., Kaiser,B., Fournier,S., Li,L., Desjardins,J., Skeldon,A., Rimkunas,V., Veloso,A., Young,J.T.F., *et al.* (2022) Guiding ATR and PARP inhibitor combinationswith chemogenomic screens. *Cell Rep.*, **40**, 111081.
55. Hustedt,N., Álvarez-Quilón,A., McEwan,A., Yuan,J.Y., Cho,T., Koob,L., Hart,T. and Durocher,D. (2019) A consensus set of genetic vulnerabilities to ATR inhibition. *Open Biol*, **9**, 190156.
56. Sharma,A.B., Ramlee,M.K., Kosmin,J., Higgs,M.R., Wolstenholme,A., Ronson,G.E., Jones,D., Ebner,D., Shamkhi,N., Sims,D., *et al.* (2023) C16orf72/HAPSTR1/TAPR1 functions with BRCA1/Senataxin to modulate replication-associated R-loops and confer resistance to PARP disruption. *Nat. Commun.*, **14**, 5003.
57. Petermann,E., Lan,L. and Zou,L. (2022) Sources, resolution and physiological relevance of R-loops and RNA-DNA hybrids. *Nat. Rev. Mol. Cell Biol.*, **23**, 521–540.
58. Laspata,N., Kaur,P., Mersaoui,S.Y., Muoio,D., Liu,Z.S., Bannister,M.H., Nguyen,H.D., Curry,C., Pascal,J.M., Poirier,G.G., *et al.* (2023) PARP1 associates with R-loops to promote their resolution and genome stability. *Nucleic Acids Res.*, **51**, 2215–2237.
59. Cristini,A., Groh,M., Kristiansen,M.S. and Gromak,N. (2018) RNA/DNA hybrid interactome identifies DXH9 as a molecular player in transcriptional termination and R-loop-associated DNA damage. *Cell Rep.*, **23**, 1891–1905.
60. Lin,W.-L., Chen,J.-K., Wen,X., He,W., Zarceno,G.A., Chen,Y., Chen,S., Paull,T.T. and Liu,H.-W. (2022) DDX18 prevents R-loop-induced DNA damage and genome instability via PARP-1. *Cell Rep.*, **40**, 111089.
61. Bou-Nader,C., Bothra,A., Garboczi,D.N., Leppla,S.H. and Zhang,J. (2022) Structural basis of R-loop recognition by the S9.6 monoclonal antibody. *Nat. Commun.*, **13**, 1641.
62. Zeman,M.K. and Cimprich,K.A. (2014) Causes and consequences of replication stress. *Nat. Cell Biol.*, **16**, 2–9.
63. Buisson,R., Boisvert,J.L., Benes,C.H. and Zou,L. (2015) Distinct but concerted roles of ATR, DNA-PK, and Chk1 in countering replication stress during S phase. *Mol. Cell*, **59**, 1011–1024.
64. Liu,S., Shiotani,B., Lahiri,M., Maréchal,A., Tse,A., Leung,C.C.Y., Mark Glover,J.N., Yang,X.H. and Zou,L. (2011) ATR autophosphorylation as a molecular switch for checkpoint activation. *Mol. Cell*, **43**, 192–202.
65. Maréchal,A. and Zou,L. (2015) RPA-coated single-stranded DNA as a platform for post-translational modifications in the DNA damage response. *Cell Res.*, **25**, 9–23.
66. Schoonen,P.M., Kok,Y.P., Wierenga,E., Bakker,B., Foijer,F., Spierings,D.C.J. and van Vugt,M.A.T.M. (2019) Premature mitotic entry induced by ATR inhibition potentiates olaparib inhibition-mediated genomic instability, inflammatory signaling, and cytotoxicity in BRCA2-deficient cancer cells. *Mol Oncol*, **13**, 2422–2440.

67. Cybulla,E. and Vindigni,A. (2023) Leveraging the replication stress response to optimize cancer therapy. *Nat. Rev. Cancer*, **23**, 6–24.
68. Bouwman,P., Aly,A., Escandell,J.M., Pieterse,M., Bartkova,J., van der Gulden,H., Hiddingh,S., Thanasoula,M., Kulkarni,A., Yang,Q., *et al.* (2010) 53BP1 loss rescues BRCA1 deficiency and is associated with triple-negative and BRCA-mutated breast cancers. *Nat. Struct. Mol. Biol.*, **17**, 688–695.
69. Aly,A. and Ganesan,S. (2011) BRCA1, PARP, and 53BP1: conditional synthetic lethality and synthetic viability. *J. Mol. Cell Biol.*, **3**, 66–74.
70. Belotserkovskaya,R., Raga Gil,E., Lawrence,N., Butler,R., Clifford,G., Wilson,M.D. and Jackson,S.P. (2020) PALB2 chromatin recruitment restores homologous recombination in BRCA1-deficient cells depleted of 53BP1. *Nat. Commun.*, **11**, 819.
71. Johannes,J.W., Balazs,A., Barratt,D., Bista,M., Chuba,M.D., Cosulich,S., Critchlow,S.E., Degorce,S.L., Di Fruscia,P., Edmondson,S.D., *et al.* (2021) Discovery of 5-{4-[(7-Ethyl-6-oxo-5,6-dihydro-1,5-naphthyridin-3-yl)methyl]piperazin-1-yl}-N-methylpyridine-2-carboxamide (AZD5305): A PARP1-DNA Trapper with High Selectivity for PARP1 over PARP2 and Other PARPs. *J. Med. Chem.*, **64**, 14498–14512.
72. Illuzzi,G., Staniszewska,A.D., Gill,S.J., Pike,A., McWilliams,L., Critchlow,S.E., Cronin,A., Fawell,S., Hawthorne,G., Jamal,K., *et al.* (2022) Preclinical characterization of AZD5305, a next-generation, highly selective PARP1 inhibitor and trapper. *Clin. Cancer Res.*, **28**, 4724–4736.
73. Navas,T.A., Zhou,Z. and Elledge,S.J. (1995) DNA polymerase epsilon links the DNA replication machinery to the S phase checkpoint. *Cell*, **80**, 29–39.
74. Araki,H., Leem,S.H., Phongdara,A. and Sugino,A. (1995) Dpb11, which interacts with DNA polymerase II(epsilon) in Saccharomyces cerevisiae, has a dual role in S-phase progression and at a cell cycle checkpoint. *Proc. Natl. Acad. Sci. U.S.A.*, **92**, 11791–11795.
75. Borel,V., Boeing,S., Van Wietmarschen,N., Sridharan,S., Hill,B.R., Ombrato,L., Perez-Lloret,J., Jackson,D., Goldstone,R., Boulton,S.J., *et al.* (2022) Disrupted control of origin activation compromises genome integrity upon destabilization of Polε and dysfunction of the TRP53-CDKN1A/P21 axis. *Cell Rep.*, **39**, 110871.
76. Bellelli,R., Youds,J., Borel,V., Svendsen,J., Pavicic-Kaltenbrunner,V. and Boulton,S.J. (2020) Synthetic lethality between DNA polymerase epsilon and RTEL1 in metazoan DNA replication. *Cell Rep.*, **31**, 107675.
77. Smirnova,M. and Klein,H.L. (2003) Role of the error-free damage bypass postreplication repair pathway in the maintenance of genomic stability. *Mutat. Res.*, **532**, 117–135.
78. Cimprich,K.A. and Cortez,D. (2008) ATR: an essential regulator of genome integrity. *Nat. Rev. Mol. Cell Biol.*, **9**, 616–627.
79. Menolfi,D., Lee,B.J., Zhang,H., Jiang,W., Bowen,N.E., Wang,Y., Zhao,J., Holmes,A., Gershik,S., Rabadan,R., *et al.* (2023) ATR kinase supports normal proliferation in the early S phase by preventing replication resource exhaustion. *Nat. Commun.*, **14**, 3618.
80. Kim,H., George,E., Ragland,R., Rafail,S., Zhang,R., Krepler,C., Morgan,M., Herlyn,M., Brown,E. and Simpkins,F. (2017) Targeting the ATR/CHK1 axis with PARP inhibition results in tumor regression in BRCA-mutant ovarian cancer models. *Clin. Cancer Res.*, **23**, 3097–3108.
81. Haince,J.-F., Kozlov,S., Dawson,V.L., Dawson,T.M., Hendzel,M.J., Lavin,M.F. and Poirier,G.G. (2007) Ataxia telangiectasia mutated (ATM) signaling network is modulated by a novel poly(ADP-ribose)-dependent pathway in the early response to DNA-damaging agents. *J. Biol. Chem.*, **282**, 16441–16453.
82. Bryant,H.E. and Helleday,T. (2006) Inhibition of poly (ADP-ribose) polymerase activates ATM which is required for subsequent homologous recombination repair. *Nucleic Acids Res.*, **34**, 1685–1691.
83. Patel,A.G., Sarkaria,J.N. and Kaufmann,S.H. (2011) Nonhomologous end joining drives poly(ADP-ribose) polymerase (PARP) inhibitor lethality in homologous recombination-deficient cells. *Proc. Natl. Acad. Sci. U.S.A.*, **108**, 3406–3411.
84. Cheung,M., Kadariya,Y., Sementino,E., Hall,M.J., Cozzi,I., Ascoli,V., Ohar,J.A. and Testa,J.R. (2021) Novel LRRK2 mutations and other rare, non-BAP1-related candidate tumor predisposition gene variants in high-risk cancer families with mesothelioma and other tumors. *Hum. Mol. Genet.*, **30**, 1750–1761.
85. Rizvi,N.A., Hellmann,M.D., Snyder,A., Kvistborg,P., Makarov,V., Havel,J.J., Lee,W., Yuan,J., Wong,P., Ho,T.S., *et al.* (2015) Cancer immunology. Mutational landscape determines sensitivity to PD-1 blockade in non-small cell lung cancer. *Science*, **348**, 124–128.

Received: September 22, 2023. **Revised:** May 2, 2024. **Editorial Decision:** May 3, 2024. **Accepted:** May 9, 2024

Co-author certification

I, the undersigned Dr. Lajos Mátés as a corresponding author of the following publication hereby declare that the authors have no conflict of interest, and **Anna Georgina Kopasz** Ph.D. candidate had significant contribution to the jointly published research findings. The results discussed in her thesis were not used and not intended to be used in any other qualification process for obtaining a PhD degree. The specific results incorporated into her thesis are as follows: Fig.2/A,B,D; Fig.3/A,B,C,D; Suppl. Fig.2; Suppl. Fig.4/A,B.

Szeged, 2025. 10. 08.

.....

corresponding author

The publication relevant to the applicant's thesis:

Kopasz AG, Pusztai DZ*, Karkas R, Hudoba L, Abdullah KS, Imre G, Pankotai-Bodó G, Migh E, Nagy A, Kriston A, Germán P, Drubi AB, Molnár A, Fekete I, Dani VÉ, Ocsovszki I, Puskás, LG, Horváth P, Sükösd F, Mátés L, A versatile transposon-based technology to generate loss- and gain-of-function phenotypes in the mouse liver, *BMC Biology*, 20, 74 (2022). https://doi.org/10.1186/s12915-022-01262-x, **D1**

In the aforementioned publication, Anna Georgina Kopasz performed the majority of plasmid construction, RNA and DNA isolation, qPCR, RT-qPCR, and Western blot experiments. Moreover, she participated in cell culture experiments, animal processing, sample collection, and formalin fixation of the transgenic livers. She also contributed to the experimental design and data interpretation.

Co-author certification

I, the undersigned Dr. Gyula Timinszky as a corresponding author of the following publication hereby declare that the authors have no conflict of interest, and **Anna Georgina Kopasz** Ph.D. candidate had significant contribution to the jointly published research findings. The results discussed in her thesis were not used and not intended to be used in any other qualification process for obtaining a PhD degree. The specific results incorporated into her thesis are as follows: R-loop staining (Fig. 3/F, Suppl. Fig. 3/E) and hydroxyurea cell survival assay (Suppl. Fig. 3/D).

Szeged, 2025. 10. 08.

.....

corresponding author

The publication relevant to the applicant's thesis:

Hasan Mamar, Roberta Fajka-Boja*, Mónika Mórocz, Eva Pinto Jurado, Siham Zentout, Alexandra Mihuț, **Anna Georgina Kopasz**, Mihály Mérey, Rebecca Smith, Abhishek Bharadwaj Sharma, Nicholas D Lakin, Andrew James Bowman, Lajos Haracska, Sébastien Huet, Gyula Timinszky, The loss of DNA polymerase epsilon accessory subunits POLE3–POLE4 leads to BRCA1-independent PARP inhibitor sensitivity, *Nucleic Acids Research*, Volume 52, Issue 12, 8 July 2024, Pages 6994–7011, https://doi.org/10.1093/nar/gkae439, **D1**

In the aforementioned publication, Anna Georgina Kopasz performed all biological replicates of the R-loop staining and constructed the pcDNA5-FRT-TO-POLE4 plasmid. Moreover, she participated in cell survival assays, Western blot, and pRPA(T21) FACS experiments.